NUMERICAL PREDICTION OF MOBILE OFFSHORE DRILLING UNIT DRIFT DURING HURRICANES

A Thesis

by

GALIN VALENTINOV TAHCHIEV

Submitted to the Office of Graduate Studies of
Texas A&M University
in partial fulfillment of the requirements for the degree of

MASTER OF SCIENCE

May 2007

Major Subject: Ocean Engineering

NUMERICAL PREDICTION OF MOBILE OFFSHORE DRILLING UNIT DRIFT DURING HURRICANES

A Thesis

by

GALIN VALENTINOV TAHCHIEV

Submitted to the Office of Graduate Studies of
Texas A&M University
in partial fulfillment of the requirements for the degree of

MASTER OF SCIENCE

Approved by:

Chair of Committee,	Jun Zhang
Committee Members,	Richard S. Mercier
	Robert H. Stewart
Head of Department,	David V. Rosowsky

May 2007

Major Subject: Ocean Engineering

ABSTRACT

Numerical Prediction of Mobile Offshore Drilling Unit Drift
During Hurricanes. (May 2007)
Galin Valentinov Tahchiev, B.A., Technical University of Varna
Chair of Advisory Committee: Dr. Jun Zhang

Hurricanes Ivan, Katrina, and Rita tracked through a high-density corridor of the oil and gas infrastructures in the Gulf of Mexico. Extreme winds and large waves exceeding the 100-year design criteria of the MODUs during these hurricanes, caused the failure of mooring lines to a number of Mobile Offshore Drilling Units (MODUs) in the Gulf of Mexico. In addition to the damage MODUs undertook during these severe hurricanes, drifting MODUs might impose a great danger to other critical elements of the oil and gas industry. Drifting MODUs may potentially collide with fixed or floating platforms and transportation hubs or rupture pipelines by dragging anchors over the seabed. Therefore, it is desirable to understand the physics of the drift of a MODU under the impact of severe wind, wave, and current and have the capabilities to predict the trajectory of a MODU that is drifting.

In this thesis, a numerical program, named “DRIFT,” is developed for predicting the trajectory of drifting MODUs given met-ocean conditions (wind, current, and wave) and the characteristics of the MODU. To verify “DRIFT,” the predicted drift of two typical MODUs is compared with the corresponding measured trajectory recorded by Global Positioning System (GPS).

To explore the feasibility and accuracy of predicting the trajectory of a drifting MODU based on real-time or hindcast met-ocean conditions and limited knowledge of the condition of the drift, this study employed a simplified equation describing only the horizontal (surge, sway, and yaw) motions of a MODU under the impact of steady wind, current, and wave forces. The simplified hydrodynamic model neglects the first-

and second-order oscillatory wave forces, unsteady wind forces, wave drift damping, and the effects of body oscillation on the steady wind and current forces. It was assumed that the net effects of the oscillatory forces on the steady motion are insignificant.

Two types of MODU drift predictions are compared with the corresponding measured trajectories: 1) MODU drift prediction with 30-minute corrections of the trajectory (every 30 minutes the simulation of the drift starts from the measured trajectory), and 2) continuous MODU drift prediction without correction.

ACKNOWLEDGMENTS

I would like to express my sincere gratitude to my advisor and committee chair, Dr. Jun Zhang, for his encouragement, guidance, and support throughout this research and my education at Texas A&M University. Sincere thanks to Dr. Richard S. Mercier and Dr. Robert H. Stewart for serving as my committee members.

I am grateful to Dr. E.G. Ward and Evan Zimmerman for their guidance and providing the data necessary for this thesis to be completed.

TABLE OF CONTENTS

Page

Page

LIST OF FIGURES

FIGURE Page

LIST OF TABLES

1. INTRODUCTION

Hurricanes Ivan, Katrina, and Rita tracked through a high-density corridor of the oil and gas infrastructures in the Gulf of Mexico. The track of hurricane Ivan (Adapted from Sharples, 2004) is shown in Fig.1.1 and the tracks of Katrina and Rita are shown in Fig.1.2 (Adapted from Smith, 2006).

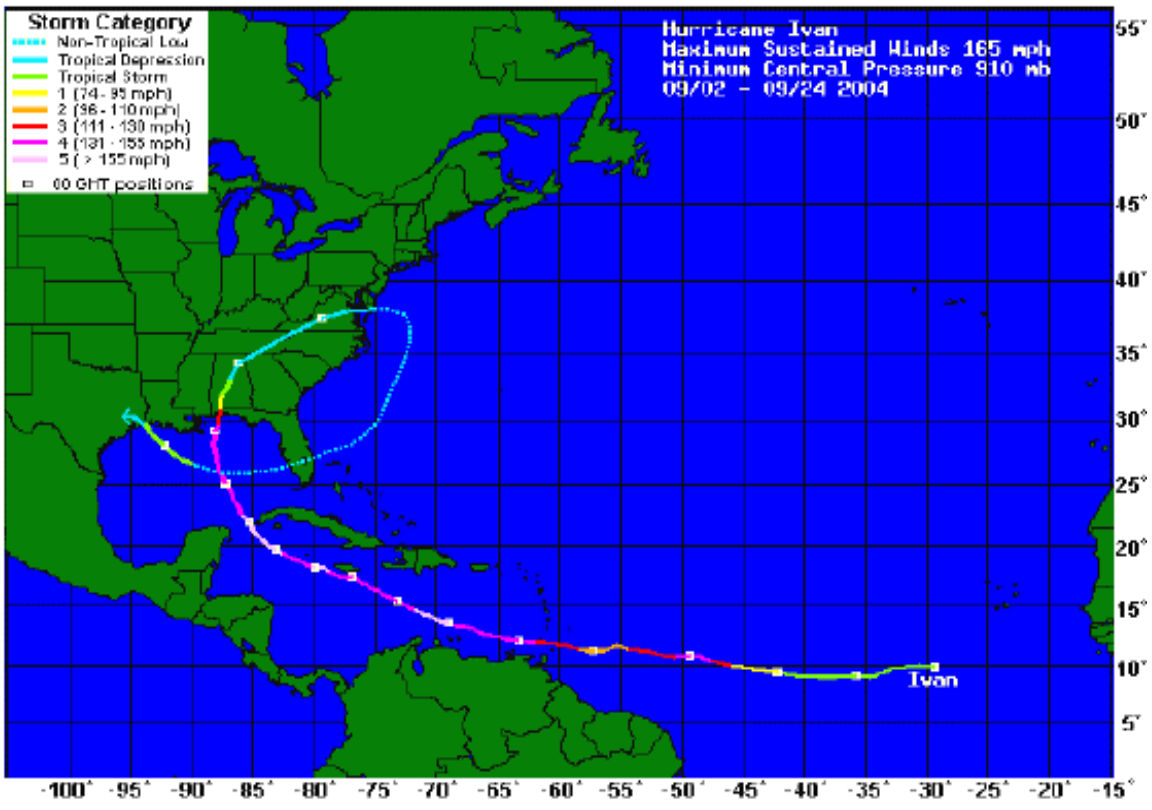

Fig.1.1. Track of hurricane Ivan.

This thesis follows the style of Ocean Engineering.

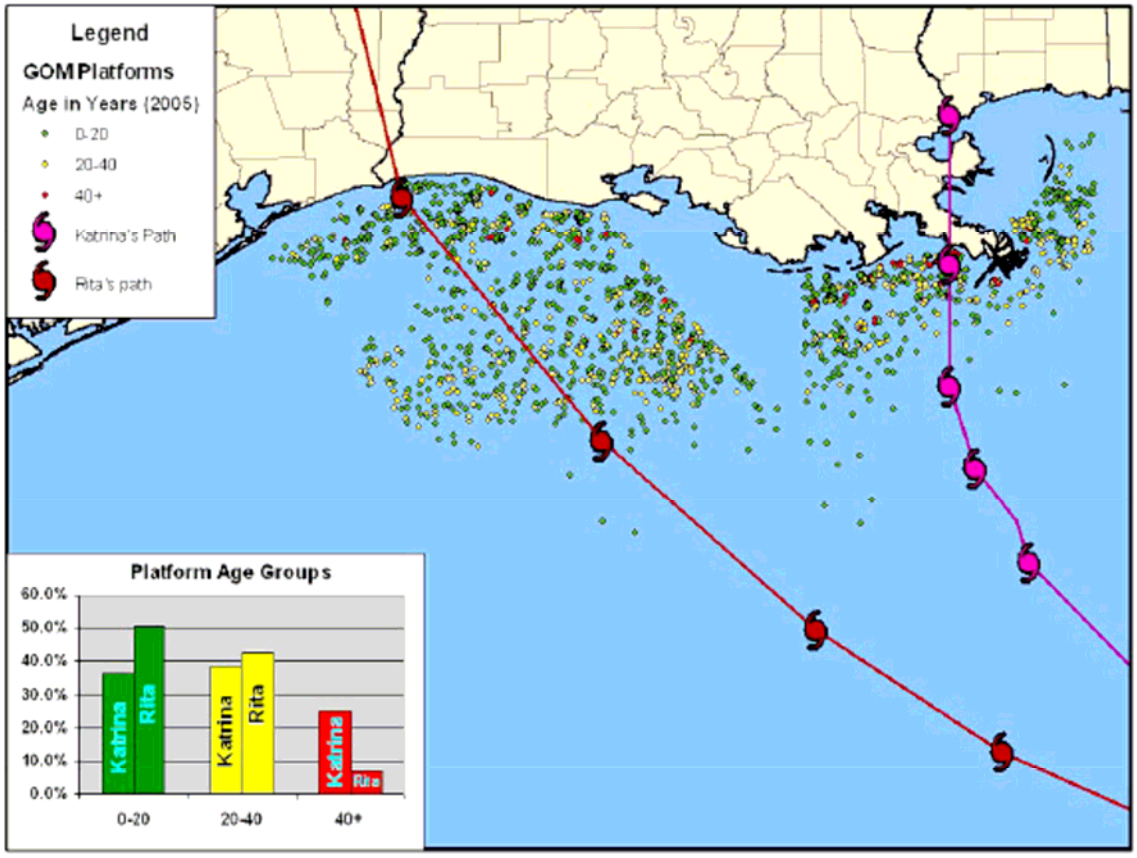

Fig.1.2. Tracks of hurricanes Katrina and Rita.

Extreme winds and large waves exceeding the 100-years design criteria during these hurricanes, caused mooring line failure to a number of Mobile Offshore Drilling Units (MODUs) in the Gulf of Mexico. Five semi-submersible MODUs went adrift during hurricane Ivan (Sharples, 2004) and nineteen MODUs were adrift or significantly damaged during hurricanes Katrina and Rita (Smith, 2006). In addition to the damage MODUs undertook during the severe hurricanes, drifting MODUs might impose a great danger to other critical elements of the oil and gas industry. Drifting MODUs may potentially collide with fixed or floating platforms and transportation hubs, or rupture pipelines by dragging anchors over the seabed. Therefore, it is desirable to understand

the physics of the drift of a MODU under the impact of severe wind, wave, and current and have the capabilities of predicting the trajectory of a drifting MODU.

In this thesis, a numerical program, named as "DRIFT", is developed for predicting the trajectory of drifted MODUs during hurricanes given hindcast or real-time met-ocean conditions (wind, current, and wave) and the characteristics of the MODUs. To validate the numerical program, the predicted drift of two typical MODUs is compared with the corresponding measured trajectory recorded by Global Positioning System (GPS). In addition to the benefit of being able to predict the trajectory of unmoored MODU for search and rescue missions in the aftermath of the hurricanes (if GPS is not available), program "DRIFT" may be used in future studies to explore innovative technological solutions and methods to control, reduce, or stop a MODU that has gone adrift in a hurricane.

An integrated semi-submersible MODU consists of a mooring system and a moored floating structure (hull). Many studies carried out coupled analysis on Spars, Semi-submersibles, and FPSOs positioned by mooring systems (Ormberg and Larsen, 1997; Ran and Kim, 1997; Ma et al., 2000). This kind of analyses considers the interactions among mooring and riser systems and the hull in calculating the motions and forces of a floating structure. When a MODU breaks its mooring lines the motion equation of a free floating body should be used.

Anderson et al. (1998) reviewed the existing practice in the computation of leeway drift and proposed generalized analysis of the force balance of a drifting object in the open ocean. Leeway, as defined by the National Search and Rescue Manual, is the movement of a craft through the water caused by the wind acting on the exposed surface of the craft. The work reviewed by Anderson et al. (1998) relevant to this study includes two reports prepared by Su (1986) and Hodgins and Mak (1995). Both reports excluded the vertical body oscillations and rotations (heave, pitch, and roll) from their models for predicting the drift and only considered the body motion in surge, sway, and yaw directions. Anderson et al. (1998) only considered the body motion in surge and sway directions. The main forces affecting the body drift are wind, current, and wave

forces. In addition, Su (1986) and Hodgins and Mak (1995) considered the inertia force term, which includes body mass and added mass.

In this study only the horizontal (surge, sway, and yaw) motions of the body due to steady wind, current, and wave (wave mean drift) forces are considered. This simplification neglects the first- and second-order oscillatory wave forces, unsteady wind forces (owing to wind gustiness), wave drift damping, and the effects of the body oscillation on the steady wind and current forces. It is assumed that the net effects of the oscillatory forces on the steady motion are insignificant and hence can be neglected.

Two typical semi-submersible MODUs were chosen for simulation studies. One is of triangular waterplane and the other of rectangular waterplane, which are named as "Generic MODU I" and "Generic MODU II", respectively. The coefficients for computing wind and current force in surge and sway directions are given based on respective model tests. The coefficients for calculating the steady wave forces are computed using WAMIT (WAMIT, Inc., 1999) and the wave amplitude determined based on a Pierson-Moskowitz wave spectrum of given peak period and significant wave height. WAMIT is commercial software developed for the analysis of the interaction of surface waves with floating structures and is based on a radiation/diffraction wave theory and a three-dimensional panel method. Two sets of hindcast met-ocean conditions (wind, current, and wave) during hurricane Katrina, called "Emergency Response Data" (ERD) and "Revised Data" (RD) were sequentially provided by Oceanweather Inc. The former was given earlier during this study and the latter more recently. For this reason, only the simulations of the drift of Generic MODU I and II based on the ERD were completed and presented in this thesis.

Hindcast information of the wind and current speeds, wind and current directions, significant wave height, peak period, and mean wave direction updated every 15 minutes is available on a rectangular grid with a step size of $\Delta\varphi = 0.05°$ and $\Delta\lambda = 0.05°$, where φ is the degree of latitude and λ the degree of longitude. In addition, a hindcast multidirectional wave spectrum, updated every 15, minutes is available on a coarser grid with a step size of $\Delta\varphi = 0.2°$ and $\Delta\lambda = 0.2°$. The so-called

"Great Circle Formula" is used for converting from latitude and longitude coordinates to Cartesian coordinates. The motion equation is solved by using Newmark-β time integration scheme with an iterative procedure.

Two types of MODU's drift predictions during the hurricane are compared with the corresponding measured trajectories recorded by GPS: 1) MODU's drift prediction with 30 minutes correction of the trajectory (every 30 minutes the simulation of the drift starts from the measured trajectory): and 2) continuous MODU's drift prediction without correction.

2. THEORY OF 6-DOF EQUATIONS OF MOTION OF A FREE FLOATING RIGID BODY

2.1 6-DOF Dynamic Equations of a Free Floating Body

The derivation of the six degree of freedom (6-DOF) equations of motion of a free floating rigid body with respect to its center of gravity (CG) follows the work of Paulling and Webster (1986), and Lee (1995) and their derivation is given briefly below.

Two coordinate systems are used in this derivation: a space-fixed coordinate system $(\hat{o}\hat{x}\hat{y}\hat{z})$ and a body-fixed coordinate system $(oxyz)$ moving with the body. The origin of the body-fixed coordinate system can be any point fixed on the body and in this derivation is taken to be the center of gravity (CG). When the body is at its initial position, the body-fixed coordinate system $(oxyz)$ coincides with the space-fixed coordinate system $(\hat{o}\hat{x}\hat{y}\hat{z})$ (see Fig. 2.1). A third, spaced-fixed coordinate system $(OXYZ)$, with the OXY plane taken to be at the free surface and *Z*-axis positive upward is introduced as a reference coordinate system for describing the incoming waves.

Newton's second law may be written in terms of the rate of change of the linear and angular momentum:

$$\frac{d\hat{\mathbf{L}}}{dt} = \hat{\mathbf{F}} \tag{2.1}$$

$$\frac{d\mathbf{H}_{CG}}{dt} = \mathbf{M}_{CG} \tag{2.2}$$

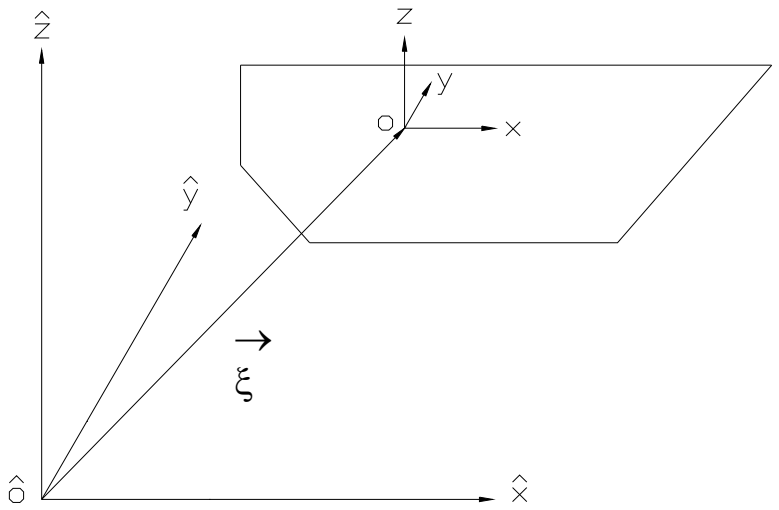

Fig.2.1. Coordinate systems.

where $\hat{\mathbf{L}}$ is the linear momentum, $\mathbf{H}_{CG}$ the angular momentum with respect to CG, $\hat{\mathbf{F}}$ the applied forces, and $\mathbf{M}_{CG}$ the applied moments. The linear momentum $(\hat{\mathbf{L}})$ may be written as the product of the rigid body mass (m) and the velocity at its center of gravity $(\hat{\mathbf{v}}_{CG})$:

$$\hat{\mathbf{L}} = m\hat{\mathbf{v}}_{CG} \tag{2.3}$$

The angular momentum with respect to CG, expressed in the body-fixed coordinate system is:

$$\mathbf{H}_{CG} = \mathbf{I}_{CG}\boldsymbol{\omega} \tag{2.4}$$

where $\mathbf{I}_{CG}$ is the moment of inertia matrix with respect to CG expressed in the body-fixed coordinate system (oxyz). Vector $(\boldsymbol{\omega})$ is the angular velocity also expressed in oxyz.

After substituting equations (2.3) and (2.4) into equations (2.1) and (2.2) respectively, the translational and rotational motion equations are given by:

$$m\hat{\mathbf{a}}_{CG} = \hat{\mathbf{F}} \tag{2.5}$$

$$\mathbf{I}_{CG}\frac{d\boldsymbol{\omega}}{dt} + \boldsymbol{\omega} \times \mathbf{I}_{CG}\boldsymbol{\omega} = \mathbf{M}_{CG} \tag{2.6}$$

where $\hat{\mathbf{a}}_{CG}$ is the acceleration at the center of gravity (CG) and the moments $\mathbf{M}_{CG}$ are defined with respect to the body-fixed coordinate system.

The angular velocity vector $(\boldsymbol{\omega})$ may be written in terms of Euler angles:

$$\boldsymbol{\omega} = \mathbf{B}\frac{d\boldsymbol{\alpha}}{dt} \tag{2.7}$$

where $\boldsymbol{\alpha} = (\boldsymbol{\alpha}_1, \boldsymbol{\alpha}_2, \boldsymbol{\alpha}_3)^t$ are the Euler angles in the roll-pitch-yaw sequence, superscript (t) represents transpose of a matrix, and the matrix (**B**) is given by:

$$\mathbf{B} = \begin{bmatrix} \cos\alpha_3 \cos\alpha_2 & \sin\alpha_3 & 0 \\ -\sin\alpha_3 \cos\alpha_2 & \cos\alpha_3 & 0 \\ \sin\alpha_2 & 0 & 1 \end{bmatrix} \tag{2.8}$$

The first derivative of the angular velocity with respect to time is:

$$\frac{d\boldsymbol{\omega}}{dt} = \mathbf{B}\frac{d^2\boldsymbol{\alpha}}{dt^2} + \boldsymbol{\alpha}_q \tag{2.9}$$

where

$$\boldsymbol{\alpha}_q = \frac{d\mathbf{B}}{dt}\frac{d\boldsymbol{\alpha}}{dt} = \begin{bmatrix} -\cos\alpha_3 \sin\alpha_2\alpha_{2t} - \sin\alpha_3 \cos\alpha_2\alpha_{3t} & \cos\alpha_3\alpha_{3t} & 0 \\ \sin\alpha_3 \sin\alpha_2\alpha_{2t} - \cos\alpha_3 \cos\alpha_2\alpha_{3t} & -\sin\alpha_3\alpha_{3t} & 0 \\ \cos\alpha_2\alpha_{2t} & 0 & 0 \end{bmatrix} \begin{Bmatrix} \alpha_{1t} \\ \alpha_{2t} \\ \alpha_{3t} \end{Bmatrix} \tag{2.10}$$

$$\frac{d\boldsymbol{\alpha}}{dt} = (\alpha_{1t}, \alpha_{2t}, \alpha_{3t})^t \tag{2.11}$$

Furthermore, more general motion equations with respect to the center of the body-fixed coordinate system are derived. The acceleration at the center of gravity (CG) expressed in the space-fixed coordinate system $(\hat{o}\hat{x}\hat{y}\hat{z})$ is:

$$\hat{\mathbf{a}}_{CG} = \hat{\mathbf{a}}_o + \mathbf{T}^t\left(\frac{d\boldsymbol{\omega}}{dt} \times \mathbf{r}_{CG} + \boldsymbol{\omega} \times (\boldsymbol{\omega} \times \mathbf{r}_{CG})\right) \tag{2.12}$$

where:

$\hat{\mathbf{a}}_o = \frac{d^2\boldsymbol{\xi}}{dt^2}$ is the acceleration at point *o* of the body expressed in $\hat{o}\hat{x}\hat{y}\hat{z}$;

$\boldsymbol{\xi} = (\xi_1, \xi_2, \xi_3)^t$ is the displacement at point *o* of the body expressed in $\hat{o}\hat{x}\hat{y}\hat{z}$;

$\boldsymbol{\omega} = (\omega_1, \omega_2, \omega_3)^t$ is the angular velocity expressed in $oxyz$;

$\mathbf{r}_{CG} = (x_{CG}, y_{CG}, z_{CG})^t$ is the vector of the center of gravity (mass) of the body expressed in $oxyz$.

T is a transfer matrix between the body-fixed coordinate system and the space-fixed coordinate system expressed as:

$$\mathbf{T} = \begin{bmatrix} \cos\alpha_3\cos\alpha_2 & \sin\alpha_3\cos\alpha_1 + \cos\alpha_3\sin\alpha_2\sin\alpha_1 & \sin\alpha_3\sin\alpha_1 - \cos\alpha_3\sin\alpha_2\cos\alpha_1 \\ -\sin\alpha_3\cos\alpha_2 & \cos\alpha_3\cos\alpha_1 - \sin\alpha_3\sin\alpha_2\sin\alpha_1 & \cos\alpha_3\sin\alpha_1 + \sin\alpha_3\sin\alpha_2\cos\alpha_1 \\ \sin\alpha_2 & -\cos\alpha_2\sin\alpha_1 & \cos\alpha_2\cos\alpha_1 \end{bmatrix} \tag{2.13}$$

The transfer matrix (**T**) is an orthogonal matrix with the property $\mathbf{T}^t=\mathbf{T}^{-1}$, where superscript (-1) indicates inverse of a matrix.

The moments in the body-fixed coordinate system with respect to CG are:

$$\mathbf{M}_{CG} = \mathbf{M}_o - \mathbf{r}_{CG} \times \mathbf{T}\hat{\mathbf{F}} \tag{2.14}$$

where:

$\hat{\mathbf{F}}$ are the total forces applied on the body expressed in $\hat{o}\hat{x}\hat{y}\hat{z}$;

$\mathbf{M}_o$ are the total moments with respect to the origin of the $oxyz$ coordinates.

Substituting equations (2.12) and (2.14) into equations (2.5) and (2.6), the translational motion equations of a rigid body expressed in $\hat{o}\hat{x}\hat{y}\hat{z}$ and the rotational motion equations expressed in $oxyz$ with respect to *o* are:

$$m\frac{d^2\boldsymbol{\xi}}{dt^2} + m\mathbf{T}^t\left(\frac{d\boldsymbol{\omega}}{dt} \times \mathbf{r}_g\right) + m\mathbf{T}^t(\boldsymbol{\omega} \times (\boldsymbol{\omega} \times \mathbf{r}_g)) = \hat{\mathbf{F}} \tag{2.15}$$

$$\mathbf{I}_o\frac{d\boldsymbol{\omega}}{dt} + \boldsymbol{\omega} \times \mathbf{I}_o\boldsymbol{\omega} + m\mathbf{r}_g \times \left(\mathbf{T}\frac{d^2\boldsymbol{\xi}}{dt^2}\right) = \mathbf{M}_o \tag{2.16}$$

where $\mathbf{I}_o$ is the moment of inertia of the body with respect to *o* expressed in $oxyz$.

The relationship between space-fixed coordinates $\hat{\mathbf{x}} = (\hat{x}, \hat{y}, \hat{z})^t$ and body-fixed coordinates $\mathbf{x} = (x, y, z)^t$ is:

$$\hat{\mathbf{x}} = \boldsymbol{\xi} + \mathbf{T}^t \mathbf{x} \tag{2.17}$$

2.2 Forces

The forces are written in general form, which has six components: the first three represent the forces in surge, sway, and heave directions and the last three for the moments in roll, pitch, and yaw (see Fig.2.2).

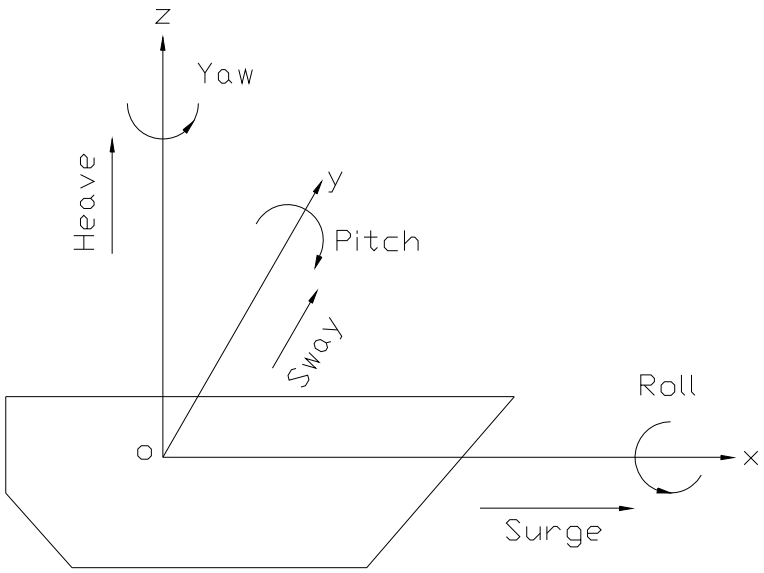

Fig.2.2. Body motion.

The total force is divided into the following sub-forces:

$$\mathbf{F} = \mathbf{F}_{\text{HFSODRT}} + \mathbf{F}_{\text{Wind}} + \mathbf{F}_{\text{Current}} + \mathbf{F}_{\text{Coriolis}} \tag{2.18}$$

where $\mathbf{F}_{\text{HFSODRT}}$ stands for hydrodynamic forces by second-order diffraction/radiation theory, $\mathbf{F}_{\text{Wind}}$ the wind forces, $\mathbf{F}_{\text{Current}}$ the current forces, and $\mathbf{F}_{\text{Coriolis}}$ the Coriolis forces.

2.2.1 Hydrodynamic Forces by Second-order Diffraction/Radiation Theory

The hydrodynamic forces calculated based on a second-order diffraction/radiation theory (such as WAMIT) consist of:

$$\mathbf{F}_{\text{HFSODRT}} = \mathbf{F}_{\text{R}} + \mathbf{F}_{\text{W}} + \mathbf{F}_{\text{WD}} + \mathbf{F}_{\text{HS}} \tag{2.19}$$

where $\mathbf{F}_{\text{R}}$ stands for the radiation forces, $\mathbf{F}_{\text{W}}$ the wave exciting forces, $\mathbf{F}_{\text{HS}}$ the linear part of the hydrostatic forces, and $\mathbf{F}_{\text{WD}}$ the wave drift damping forces.

2.2.1.1 Radiation Forces

The radiation forces are due to the body motion in each of its six modes of motion in still water. The equation of radiation forces for an arbitrary motion of the body was derived by many authors for first-order (Chitrapu and Ertekin, 1995) and second-order problems (de Boom et al., 1983; Ran and Kim, 1997). It is given as:

$$\mathbf{F}_{\text{R}} = -\left\{ \mathbf{M}(\infty)\ddot{\mathbf{x}}(t) + \int_{-\infty}^{t} \mathbf{K}(t-\tau)\dot{\mathbf{x}}(\tau)d\tau \right\} \tag{2.20}$$

$$\mathbf{K}(t) = \frac{2}{\pi}\int_{0}^{\infty} \mathbf{B}(\omega)\cos(\omega t)d\omega \tag{2.21}$$

$$\mathbf{M}(\infty) = \mathbf{A}(\omega) + \frac{1}{\omega}\int_0^{\infty} \mathbf{K}(t)\sin(\omega t)dt \tag{2.22}$$

where $\mathbf{M}(\infty)$ is the added-mass matrix at infinite wave frequency (ω), and $\mathbf{K}(t)$ is the retardation function matrix. $\mathbf{A}(\omega)$ and $B(\omega)$ are the added-mass and wave-damping coefficient matrices at frequency (ω) and $\mathbf{x} = (\xi_1, \xi_2, \xi_3, \alpha_1, \alpha_2, \alpha_3)^t$ describes 6-DOF displacement of the body (see Fig.2.2).

$$\mathbf{x} = \begin{bmatrix} \xi_1 \\ \xi_2 \\ \xi_3 \\ \alpha_1 \\ \alpha_2 \\ \alpha_3 \end{bmatrix} = \begin{bmatrix} \text{Surge} \\ \text{Sway} \\ \text{Heave} \\ \text{Roll} \\ \text{Pitch} \\ \text{Yaw} \end{bmatrix} \tag{2.23}$$

2.2.1.2 Wave Exciting Forces

The wave exciting forces are induced by both, incident and scattered waves. An incident wave is the wave without the body obstructing the flow. Scattered wave represents the disturbance of the incident wave due to the presence of the body assuming it is fixed in space. Wave diffraction combines the effects of both the incident and scattered waves. In using a second-order diffraction/radiation theory, the wave exciting forces are divided into first- and second-order forces:

$$\mathbf{F}_W = \mathbf{F}_W^{(1)} + \mathbf{F}_W^{(2)} \tag{2.24}$$

In using the summation method the incident wave is decomposed into N discrete wave components:

$$\eta(t) = \mathrm{Re}\sum_{j=1}^{N} A_j e^{i\omega_j t} \tag{2.25}$$

where A_j and ω_j are the amplitude and frequency of the j^{th} wave component, respectively. The amplitude of the j^{th} wave component (A_j) is computed by:

$$\left|A_j\right| = \sqrt{2S(\omega)\Delta\omega} \tag{2.26}$$

where $S(\omega)$ is the wave energy density spectrum and $\Delta\omega$ the bandwidth. If measured time series of the wave elevation are available, the amplitude of the j^{th} wave component (A_j) can be found by using fast Fourier transform (FFT).

If we define the linear (first-order) diffraction forces by $\mathbf{F}^{D(1)}(\omega)$, the second-order sum-frequency diffraction force by $\mathbf{F}^{D(2+)}(\omega_j, \omega_k)$, and the second-order difference-frequency diffraction force by $\mathbf{F}^{D(2-)}(\omega_j, \omega_k)$, the corresponding force transfer functions are given by:

$$\mathbf{Q}^{(1)}(\omega) = \frac{\mathbf{F}^{D(1)}(\omega)}{A} \tag{2.27}$$

$$\mathbf{Q}^{(2+)}(\omega_j, \omega_k) = \frac{\mathbf{F}^{D(2+)}(\omega_j, \omega_k)}{A_j A_k} \tag{2.28}$$

$$\mathbf{Q}^{(2-)}(\omega_j, \omega_k) = \frac{\mathbf{F}^{D(2-)}(\omega_j, \omega_k)}{A_j A_k} \tag{2.29}$$

where $\mathbf{Q}^{(1)}(\omega)$ is the linear force transfer function (LTF). $\mathbf{Q}^{(2+)}(\omega_j, \omega_k)$ and $\mathbf{Q}^{(2-)}(\omega_j, \omega_k)$ are the second-order (quadratic) sum- and difference-frequency force transfer functions (QTFs), respectively. A_j and A_k are the amplitudes of the wave

components with frequencies ω_j and ω_k, respectively. The force transfer functions can be found by using WAMIT.

The first-order and second-order wave exciting forces can be computed by:

$$\mathbf{F}_W^{(1)}(t) = \mathrm{Re}\sum_{j=1}^{N} A_j \mathbf{Q}^{(1)}(\omega_j) e^{i\omega_j t} \tag{2.30}$$

$$\mathbf{F}_W^{(2)}(t) = \mathrm{Re}\sum_{j=1}^{N}\sum_{k=1}^{N}\left[A_j A_k \mathbf{Q}^{(2+)}(\omega_j,\omega_k) e^{i(\omega_j+\omega_k)t} + A_j A_k^{*} \mathbf{Q}^{(2-)}(\omega_j,\omega_k) e^{i(\omega_j-\omega_k)t}\right] \tag{2.31}$$

where superscript * represents the complex conjugate.

Equation (2.31) renders the respective terms for mean, sum-, and difference-frequency second-order wave forces. The difference-frequency second-order wave forces act at low frequencies and are called slow drift forces. The sum-frequency second-order wave forces act at high frequencies and are called springing forces. The mean drift forces in a random sea are given by:

$$\mathbf{F}_{WMDF} = \sum_{j=1}^{N} A_j^2 \mathbf{Q}^{(2-)}(\omega_j,\omega_j) = 2\int_0^{\infty} S(\omega)\mathbf{Q}^{(2-)}(\omega,\omega)d\omega \tag{2.32}$$

2.2.1.3 Wave Drift Damping

The damping of a surface-piercing body oscillating in still water has two components, potential (radiation) and viscous damping. The damping of the same body in incident waves differs from that in still water and is usually greater.

The wave drift damping forces on a 6-DOF body in the time domain (Chen, 2002) can be calculated by:

$$\mathbf{F}_{WD}(t) = \mathbf{b}^{WD}(t)\dot{\mathbf{x}}(t) = \begin{bmatrix} b_{11}^{WD}(t) & b_{12}^{WD}(t) & 0 & 0 & 0 & b_{16}^{WD}(t) \\ b_{21}^{WD}(t) & b_{22}^{WD}(t) & 0 & 0 & 0 & b_{26}^{WD}(t) \\ 0 & 0 & 0 & 0 & 0 & 0 \\ 0 & 0 & 0 & 0 & 0 & 0 \\ 0 & 0 & 0 & 0 & 0 & 0 \\ b_{61}^{WD}(t) & b_{62}^{WD}(t) & 0 & 0 & 0 & b_{66}^{WD}(t) \end{bmatrix} \begin{Bmatrix} \dot{\xi}_1 \\ \dot{\xi}_2 \\ \dot{\xi}_3 \\ \dot{\alpha}_1 \\ \dot{\alpha}_2 \\ \dot{\alpha}_3 \end{Bmatrix} \tag{2.33}$$

The time-dependent wave drift damping coefficients $\left(\mathbf{b}^{WD}(t)\right)$ can be computed by:

$$\mathbf{b}^{WD}(t) = \mathrm{Re}\left\{ \left[\sum_{i=1}^{N} A_i \mathbf{B}^{WD}(\omega_i) e^{i\omega_i t} \right] \left[\sum_{j=1}^{N} A_j^{*} e^{-i\omega_j t} \right] \right\} \tag{2.34}$$

where the wave-drift damping matrix expressed in 2-DOF (surge and sway) (Nielsen et al., 1994) is given by:

$$\begin{aligned} \mathbf{B}_{11}^{WD}(\omega,\beta) &= \left(\frac{\omega^2}{g}\frac{\partial \mathbf{Q}_{dx}}{\partial \omega} + \frac{4\omega}{g}\mathbf{Q}_{dx}\right)\cos\beta - \frac{2\omega}{g}\frac{\partial \mathbf{Q}_{dx}}{\partial \beta}\sin\beta \\ \mathbf{B}_{12}^{WD}(\omega,\beta) &= \left(\frac{\omega^2}{g}\frac{\partial \mathbf{Q}_{dx}}{\partial \omega} + \frac{4\omega}{g}\mathbf{Q}_{dx}\right)\sin\beta + \frac{2\omega}{g}\frac{\partial \mathbf{Q}_{dx}}{\partial \beta}\cos\beta \\ \mathbf{B}_{21}^{WD}(\omega,\beta) &= \left(\frac{\omega^2}{g}\frac{\partial \mathbf{Q}_{dy}}{\partial \omega} + \frac{4\omega}{g}\mathbf{Q}_{dy}\right)\cos\beta - \frac{2\omega}{g}\frac{\partial \mathbf{Q}_{dy}}{\partial \beta}\sin\beta \\ \mathbf{B}_{22}^{WD}(\omega,\beta) &= \left(\frac{\omega^2}{g}\frac{\partial \mathbf{Q}_{dy}}{\partial \omega} + \frac{4\omega}{g}\mathbf{Q}_{dy}\right)\sin\beta + \frac{2\omega}{g}\frac{\partial \mathbf{Q}_{dy}}{\partial \beta}\cos\beta \end{aligned} \tag{2.35}$$

$\mathbf{Q}_{dx}$ and $\mathbf{Q}_{dy}$ are the mean wave drift force coefficients at frequency (ω) in surge and sway direction respectively, and (β) is the wave incident angle. By extending 2-DOF wave-drift damping matrix into 6-DOF, the wave-drift damping matrix can be expressed (Grue, 1999) as:

$$\mathbf{B}^{WD}(\omega,\beta)=\begin{bmatrix} B_{11}^{WD}(\omega,\beta) & B_{12}^{WD}(\omega,\beta) & 0 & 0 & 0 & B_{16}^{WD}(\omega,\beta) \\ B_{21}^{WD}(\omega,\beta) & B_{22}^{WD}(\omega,\beta) & 0 & 0 & 0 & B_{26}^{WD}(\omega,\beta) \\ 0 & 0 & 0 & 0 & 0 & 0 \\ 0 & 0 & 0 & 0 & 0 & 0 \\ 0 & 0 & 0 & 0 & 0 & 0 \\ B_{61}^{WD}(\omega,\beta) & B_{62}^{WD}(\omega,\beta) & 0 & 0 & 0 & B_{66}^{WD}(\omega,\beta) \end{bmatrix} \tag{2.36}$$

2.2.1.4 Hydrostatic Restoring Forces

The hydrostatic restoring forces can be expressed in the following form:

$$\mathbf{F}_{HS} = -\mathbf{C}\mathbf{x} \tag{2.37}$$

where the hydrostatic stiffness matrix (**C**) (Newman, 1999; Lee, 1995) is given by:

$$\mathbf{C}=\begin{bmatrix} 0 & 0 & 0 & 0 & 0 & 0 \\ 0 & 0 & 0 & 0 & 0 & 0 \\ 0 & 0 & \rho g A^{(o)} & \rho g I_Y^A & -\rho g I_X^A & 0 \\ 0 & 0 & \rho g I_Y^A & \rho g\left[I_{YY}^A + V^{(o)} z_{B,b}\right] - mgz_{B,g} & -\rho g I_{XY}^A & -\rho g V^{(o)} x_{B,b} + mgx_{B,g} \\ 0 & 0 & -\rho g I_X^A & -\rho g I_{YX}^A & \rho g\left[I_{XX}^A + V^{(o)} z_{B,b}\right] - mgz_{B,g} & -\rho g V^{(o)} y_{B,b} + mgy_{B,g} \\ 0 & 0 & 0 & 0 & 0 & 0 \end{bmatrix} \tag{2.38}$$

where ρ is the water density, g the acceleration due to gravity, $A^{(o)}$ the water plane area, $V^{(o)}$ the submerged volume of the body, $(x_{B,b}, y_{B,b}, z_{B,b})$ the coordinates of the center of buoyancy, $(x_{B,g}, y_{B,g}, z_{B,g})$ the coordinates of the center of gravity, m the body mass, and I_X^A, I_Y^A, I_{XX}^A, I_{YY}^A, $I_{XY}^A = I_{YX}^A$ the moments of inertia of the water plane area.

For a free-floating body, $mg = \rho g V^{(0)}$ and the body-fixed horizontal coordinates of the center of buoyancy coincide with those of the center of gravity, hence:

$$\begin{aligned} C(4,6) &= -\rho g V^{(o)} x_{B,b} + mg x_{B,g} = 0 \\ C(5,6) &= -\rho g V^{(o)} y_{B,b} + mg y_{B,g} = 0 \end{aligned} \tag{2.39}$$

Furthermore, the hydrostatic stiffness in roll and pitch directions, $C(4,4)$ and $C(5,5)$ respectively, can be rewritten as:

$$\begin{aligned} C(4,4) &= \rho g\left[I_{YY}^A + V^{(o)} z_{B,b}\right] - mg z_{B,g} = \rho g V^{(o)}\left[\frac{I_{YY}^A}{V^{(o)}} + z_{B,b} - z_{B,g}\right] = \rho g V^{(o)} GMT \\ C(5,5) &= \rho g\left[I_{XX}^A + V^{(o)} z_{B,b}\right] - mg z_{B,g} = \rho g V^{(o)}\left[\frac{I_{XX}^A}{V^{(o)}} + z_{B,b} - z_{B,g}\right] = \rho g V^{(o)} GML \end{aligned} \tag{2.40}$$

where GMT is the transverse metacentric height and GML the longitudinal metacentric height.

The hydrostatic stiffness matrix computed by WAMIT is given by:

$$\begin{aligned}
C(3,3) &= \overline{C}(3,3)\rho g L^2 \\
C(3,4) &= \overline{C}(3,4)\rho g L^3 \\
C(3,5) &= \overline{C}(3,5)\rho g L^3 \\
C(4,4) &= \overline{C}(4,4)\rho g L^4 \\
C(4,5) &= \overline{C}(4,5)\rho g L^4 \\
C(4,6) &= \overline{C}(4,6)\rho g L^4 \\
C(5,5) &= \overline{C}(5,5)\rho g L^4 \\
C(5,6) &= \overline{C}(5,6)\rho g L^4
\end{aligned} \tag{2.41}$$

where $\overline{C}(i,j)$ is the non-dimensional coefficient (output from WAMIT) and L the dimensional unit length, characterizing the body dimensions.

2.2.2 Wind Force

The instantaneous wind force on an element of the structure, whose center of pressure is at elevation z_{CP} (Faltinsen, 1990), is given by:

$$\mathbf{F}_{Wind}(z_{CP},t) = \frac{1}{2}\rho_a C_{dw} A_{pw}\left[u_w(z_{CP},t) - \frac{d\mathbf{x}(z_{CP},t)}{dt}\right]^2 \tag{2.42}$$

where ρ_a is the air density, C_{dw} the drag coefficient, A_{pw} the projected area of the structural element in the direction of the wind velocity (u_w), and $\frac{d\mathbf{x}(z_{CP},t)}{dt}$ the instantaneous velocity of the structural element in the direction of the mean flow. The instantaneous wind speed (u_w) may be written as the sum of the mean wind speed $(\overline{U}_w(z_{CP}))$ and the instantaneous wind velocity fluctuation about the mean $(u'_w(z_{CP},t))$:

$$u_w(z_{CP},t) = \overline{U}_w(z_{CP}) + u'_w(z_{CP},t) \tag{2.43}$$

Using an approach similar to the summation method for the random incident wave, random wind can be decompose into N discrete wind components:

$$u_w(z_{CP},t) = \overline{U}_w(z_{CP}) + \sum_{j=1}^{N} |u_j| \cos(\omega_j t + \psi_j) \tag{2.44}$$

where u_j and ω_j are the amplitude and frequency of the j^{th} wind speed component, respectively and ψ_j is the random phase angle. The amplitude of the wind speed of the j^{th} wind component (u_j) is computed by:

$$|u_j| = \sqrt{2S_w(\omega)\Delta\omega} \tag{2.45}$$

where $S_w(\omega)$ is the wind speed spectrum and $\Delta\omega$ the bandwidth. If measured time series of the wind speed are available, the wind speed of the j^{th} wind component (u_j) can be found using FFT.

There are several wind models for describing the wind speed spectrum. The American Petroleum Institute (API) wind spectrum (API, 1993) has the following expression as seen below:

$$S_w(\omega) = \frac{\sigma^2(z)}{2\pi f_r \left[1 + \frac{1.5\omega}{2\pi f_r}\right]^{5/3}} \tag{2.46}$$

where $\sigma^2(z)$ is the variance of the wind speed at elevation (z), and f_r a reference frequency given by:

$$f_r = \frac{0.025\overline{U}_w(z)}{z} \tag{2.47}$$

The standard deviation of the wind speed $(\sigma(z))$ is related to the wind turbulence intensity by:

$$\frac{\sigma(z)}{\overline{U}_w(z)} = \begin{cases} 0.15\left(\frac{z}{z_S}\right)^{-0.125} & \text{for } z/z_S \le 1 \\ 0.15\left(\frac{z}{z_S}\right)^{-0.275} & \text{for } z/z_S > 1 \end{cases} \tag{2.48}$$

where $z_S = 20$ m. An API wind spectrum for $\overline{U}_w = 100$ ft/s is sketched in Fig. 2.3.

From equation (2.42) for the mean wind force we have:

$$\overline{\mathbf{F}}_{Wind}(z_{CP}, t) = \frac{1}{2}\rho_a C_{dw} A_{pw}\left[\overline{U}_w(z_{CP}) - \frac{d\mathbf{x}(z_{CP}, t)}{dt}\right]^2 \tag{2.49}$$

Equation (2.49) accounts for the relative velocity between the wind and the body. Even though the wind speed is usually much greater than the body velocity, retaining the body velocity term may be important as it contributes to damping effects.

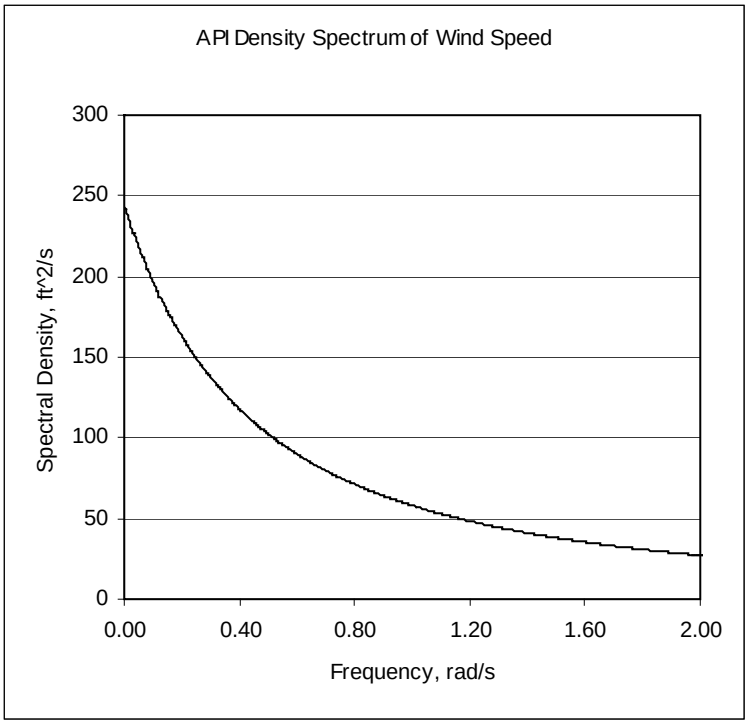

Fig.2.3. API wind speed spectrum.

2.2.3 Current Force

The mean current force is calculated using an expression similar to the one for the mean wind force.

$$\overline{\mathbf{F}}_{\text{Current}}(z_{CP},t)=\frac{1}{2}\rho C_{dc}A_{pc}\left[\overline{U}_c(z_{CP})-\frac{d\mathbf{x}(z_{CP},t)}{dt}\right]^2 \qquad (2.50)$$

where ρ is the water density, C_{dc} the drag coefficient, A_{pc} the projected area of the structural element in the direction of the mean current velocity $\left(\overline{U}_c(z_{CP})\right)$, and $\frac{d\mathbf{x}(z_{CP},t)}{dt}$ the instantaneous velocity of the structural element in the direction of the mean flow.

2.2.4 Coriolis Force

Due to the rotation of the Earth, the Coriolis acceleration will induce a force on the body. The surge and sway components of the Coriolis force (Hodgins and Mak, 1995) are given by:

$$\begin{aligned} \mathbf{F}_{CoriolisX} &= mf\frac{d\mathbf{x}_2}{dt} \\ \mathbf{F}_{CoriolisY} &= -mf\frac{d\mathbf{x}_1}{dt} \end{aligned} \tag{2.51}$$

where m is the body mass, $\frac{d\mathbf{x}_1}{dt}$ and $\frac{d\mathbf{x}_2}{dt}$ the body velocities in the surge and sway directions, respectively. The Coriolis parameter $(f)$is given by:

$$f = 2\Omega\sin\varphi \tag{2.52}$$

where $\Omega \approx 7.3\times10^{-5}$ rad/s is the angular velocity of the Earth and φ the latitude of the body position.

The Coriolis force of MODU I and II was computed, in order to explore whether or not it will affect the MODU's drift. It was found that the maximum Coriolis force is about $(1/500)^{th}$ of the wind force, which is the dominant force applied on the body and hence can be neglected in this study.

2.2.5 Summary of the 6-DOF dynamic equations

The 6DOF motion equations are summarized below:

$$\begin{aligned}&\left[\mathbf{M}_S+\mathbf{M}(\infty)\right]\ddot{\mathbf{x}}(t)+\int_{-\infty}^{t}\mathbf{K}(t-\tau)\dot{\mathbf{x}}(\tau)d\tau+\mathbf{b}^{WD}(t)\dot{\mathbf{x}}(t)+\mathbf{C}\mathbf{x}(t)\\&=\mathbf{F}_W^{(1)}+\mathbf{F}_W^{(2)}+\mathbf{F}_{Wind}+\mathbf{F}_{Current}+\mathbf{F}_{Coriolis}+\mathbf{F}_e\end{aligned}\tag{2.53}$$

where

$$\mathbf{F}_e=\begin{Bmatrix}-m\mathbf{T}^t(\boldsymbol{\omega}\times(\boldsymbol{\omega}\times\mathbf{r}_g))-m\mathbf{T}^t(\boldsymbol{\alpha}_q\times\mathbf{r}_g)\\-\boldsymbol{\omega}\times\mathbf{I}_o\boldsymbol{\omega}-\mathbf{I}_o\boldsymbol{\alpha}_q\end{Bmatrix}\tag{2.54}$$

$$\mathbf{M}_S=\begin{bmatrix}\mathbf{M} & -m\mathbf{T}^t\mathbf{R}_G\mathbf{B}\\ m\mathbf{R}_G\mathbf{T} & \mathbf{I}_o\mathbf{B}\end{bmatrix}\tag{2.55}$$

$$\mathbf{R}_G=\begin{bmatrix}0 & -z_{B,g} & y_{B,g}\\ z_{B,g} & 0 & -x_{B,g}\\ -y_{B,g} & x_{B,g} & 0\end{bmatrix}\tag{2.56}$$

$$\mathbf{M}=\begin{bmatrix}m & 0 & 0\\ 0 & m & 0\\ 0 & 0 & m\end{bmatrix}\tag{2.57}$$

$\mathbf{F}_e$ includes the nonlinear terms coming from the translation motion equation (2.15) and rotation motion equation (2.16) of a 6-DOF rigid body, $\mathbf{M}_s$ is a 6×6 mass matrix of the rigid body.

Considering the uncertainty involved in real-time or hindcast met-ocean conditions during a hurricane, at this stage this study only considers the most important factors in

the governing equation of describing the drift of an unmoored MODU. The equation describing the horizontal (surge, sway, and yaw) motions of a floating body due to steady wind, current, and wave (wave mean drift) forces is given below.

$$\left[\mathbf{M}_S + \mathbf{M}(\infty)\right]\ddot{\mathbf{x}}(t) = \overline{\mathbf{F}}_{\text{Wind}} + \overline{\mathbf{F}}_{\text{Current}} + \mathbf{F}_{\text{WMDF}} \tag{2.58}$$

The above simplified governing equation neglects the first- and second-order oscillatory wave forces, unsteady wind forces (owing to wind gustiness), wave drift damping, and the effects of the body oscillation on the steady wind and current forces. For example, the heave oscillation of the body may periodically change the area of the body exposed to wind and current. All these simplifications are made based on the assumption that the effects of oscillatory forces on the steady motion of the body are insignificant.

3. NUMERICAL IMPLEMENTATION

Numerical program "DRIFT" has been developed for predicting the trajectory of a drifted MODUs during hurricanes given met-ocean conditions (wind, current, and wave) and the characteristics of the MODU. The wind and current steady forces are computed given the wind and current force coefficients (WFC and CFC) obtained from respective model tests. The wave mean drift forces are computed by equation (2.32), where the amplitude square of the j^{th} wave component $\left(A_j^2\right)$ is determined based on Pierson-Moskowitz wave spectrum of given significant wave height and peak period, and the force transfer functions are computed using WAMIT. Great circle formula has been used for converting from latitude and longitude coordinates to Cartesian coordinates. The motion equation is solved by using Newmark-β time integration scheme with an iterative procedure.

3.1 Met-ocean Conditions

3.1.1 The Hindcast Approach

The met-ocean conditions during hurricane Katrina were provided from Oceanweather Inc. (OWI). OWI is a well known consulting firm specializing in providing the coastal and offshore industries with design data on the physical environment (wind, current, and wave data). The hindcast approach as stated in Oceanweather Inc. (2006) consists of four main steps. First, the wind field during a hurricane is specified at hourly intervals and input parameters for the tropical boundary layer model are developed. Secondly, the final wind fields are used as an input to a proven hydrodynamic model. During this step the time variant water level anomalies (storm surge) and vertically integrated storm driven currents in shallow water are modeled. Thirdly, the wind fields and the water level anomalies are used to drive the OWI's standard UNIWAVE high-resolution full spectral wave hindcast model.

Fourthly, the wind fields are used to drive a 1-D mixed layer current profile model at each grid point with water depth greater than 75 m. Additional information on the hindcast approach can be found on OWI's website www.oceanweather.com.

3.1.2 Hindcast Data

The hindcast information relevant to this study consists of wind and current speeds, wind, current and wave directions, significant wave height, and peak period updated every 15 minutes. Rectangular grid is used with the size of $\Delta\varphi = 0.05°$ and $\Delta\lambda = 0.05°$, where φ is the degree of latitude and λ the degree of longitude. The standard Fortran subroutine DQD2VL (Visual Numerics Inc., 1999) is used to determine the hindcast data at the intermediate position of the MODUs. This subroutine evaluates a function defined on rectangular grid using quadratic polynomials. The algorithm for subroutine DQD2VL is described briefly below.

If the input data for subroutine DQD2VL is defined with $(\lambda_i, \varphi_j, h_{ij})$ for $i = 1,..., n_\lambda$ and $j = 1,..., n_\varphi$, where n_λ and n_φ are the number of grid points in the zonal (longitude) and meridional (latitude) directions respectively, then given the intermediate position of the MODU (λ, φ) at which the interpolated value $h(\lambda, \varphi)$ is desired, a two- dimensional (2-D) quadratic polynomial is formed using six grid points near (λ, φ). Five of these points (See Fig.3.1) are (λ_i, φ_j), $(\lambda_{i\pm1}, \varphi_j)$, and $(\lambda_i, \varphi_{j\pm1})$, where (λ_i, φ_j) is the nearest interior grid point to (λ, φ). The sixth point is the nearest point to (λ, φ) out of the grid points $(\lambda_{i\pm1}, \varphi_{j\pm1})$. The output from subroutine DQD2VL is $h(\lambda, \varphi)$.

In order to interpolate vector quantities such as the wind and current velocities we first decomposed them in zonal and meridional directions. If $\vec{e}_{ij}$ is set to be a vector with magnitude $\left|\vec{e}_{ij}\right|$ and direction γ_{ij}, then the corresponding components are:

$$\begin{aligned} e_{ij,\lambda} &= \left| \vec{e}_{ij} \right| \cos\gamma_{ij} \\ e_{ij,\varphi} &= \left| \vec{e}_{ij} \right| \sin\gamma_{ij} \end{aligned} \tag{3.1}$$

The interpolated vector, $\vec{e}(\lambda,\varphi)$ has magnitude $\left| \vec{e}(\lambda,\varphi) \right| = \sqrt{e_\lambda^2(\lambda,\varphi) + e_\varphi^2(\lambda,\varphi)}$ and direction $\gamma(\lambda,\varphi) = \arctan\left[e_\varphi(\lambda,\varphi)/e_\lambda(\lambda,\varphi)\right]$, where $e_\lambda(\lambda,\varphi)$ and $e_\varphi(\lambda,\varphi)$ are the interpolated components at the desired location (λ,φ) obtained as an output from subroutine DQD2VL. The wave mean direction is treated as a vector with unit magnitude.

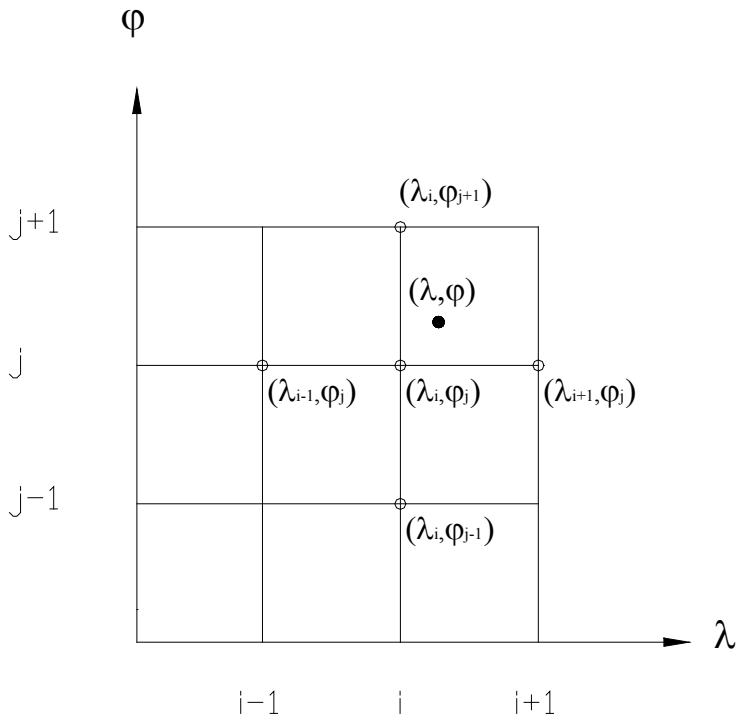

Fig.3.1. Grid points for subroutine DQD2VL.

In addition, a hindcast multidirectional wave spectrum updated every 15 minutes is available on a coarser grid with step size of $\Delta\varphi = 0.2°$ and $\Delta\lambda = 0.2°$. A typical multidirectional wave spectrum is given in Table 3.1. The first row gives the nominal frequency of each frequency bin. Frequency bins are spaced in the following geometric progression: $f_1,\ f_1 r,\ f_1 r^2,\ f_1 r^3, \ldots$. That is, each frequency after the first (f_1) one is found by multiplying the previous one by a fixed number, where $r = 0.75^{(-1/3)}$ is the frequency ratio. The nominal frequency is the mean of the two ends, i.e. the starting and ending frequencies of each frequency bin. Directional bands are identified at the first column. The 552-element array contains the variance of wave components at 23 discrete frequencies $(j = 1,..,23)$ and in 24 angular directions $(i = 1,..,24)$. The relation between the variance (σ_{ij}^2) at the i^{th} angular direction and the j^{th} discrete frequency and the corresponding wave amplitude (A_{ij}) is given by:

$$\sigma_{ij}^2 = \frac{1}{2} A_{ij}^2 \tag{3.2}$$

Highlighted in the table is the maximum energy content at each frequency.

Table 3.1

Multidirectional wave spectrum

Frequency, Hz	0.0390	0.0429	0.0472	0.0520	0.0572	0.0630	0.0693	0.0763	0.0840	0.0924	0.1017
Wave Direction, degree	**Variance, ft ^{2}**										
7.5	0.0011	0.0011	0.0011	0.0022	0.0043	0.0054	0.0065	0.0075	0.0075	0.0097	0.0172
22.5	0.0011	0.0011	0.0011	0.0022	0.0032	0.0032	0.0043	0.0043	0.0043	0.0043	0.0043
37.5	0.0011	0.0011	0.0011	0.0022	0.0032	0.0032	0.0032	0.0032	0.0032	0.0032	0.0032
52.5	0.0011	0.0011	0.0022	0.0032	0.0032	0.0032	0.0032	0.0032	0.0022	0.0022	0.0032
67.5	0.0011	0.0011	0.0022	0.0032	0.0032	0.0032	0.0032	0.0032	0.0022	0.0032	0.0032
82.5	0.0011	0.0022	0.0022	0.0032	0.0032	0.0032	0.0032	0.0032	0.0032	0.0043	0.0054
97.5	0.0011	0.0011	0.0022	0.0032	0.0032	0.0032	0.0032	0.0032	0.0043	0.0108	0.0129
112.5	0.0011	0.0011	0.0011	0.0022	0.0032	0.0032	0.0032	0.0032	0.0054	0.0172	0.0312
127.5	0.0000	0.0000	0.0011	0.0011	0.0022	0.0022	0.0022	0.0032	0.0065	0.0172	0.0323
142.5	0.0000	0.0000	0.0000	0.0011	0.0011	0.0022	0.0022	0.0032	0.0086	0.0215	0.0355
157.5	0.0000	0.0000	0.0000	0.0000	0.0011	0.0011	0.0022	0.0032	0.0086	0.0269	0.0463
172.5	0.0000	0.0000	0.0000	0.0000	0.0011	0.0011	0.0022	0.0054	0.0086	0.0226	0.0463
187.5	0.0000	0.0000	0.0000	0.0011	0.0011	0.0022	0.0043	0.0118	0.0161	0.0355	0.0678
202.5	0.0000	0.0000	0.0011	0.0011	0.0022	0.0108	0.0161	0.0334	0.0409	0.0969	0.2131
217.5	0.0011	0.0011	0.0011	0.0022	0.0075	0.0355	0.0527	0.0947	0.1550	0.2626	0.3950
232.5	0.0011	0.0011	0.0011	0.0032	0.0205	0.0635	0.1281	0.2164	0.5619	0.4263	0.5576
247.5	0.0011	0.0022	0.0032	0.0108	0.0312	0.0818	0.2099	0.4069	0.8902	0.5436	0.6631
262.5	0.0011	0.0043	0.0129	0.0506	0.0829	0.1378	0.3003	0.6340	0.8148	0.6006	0.7072
277.5	0.0011	0.0065	0.0388	0.1948	0.3412	0.4263	0.6943	0.9289	0.9268	0.6275	0.7040
292.5	0.0022	0.0043	0.0463	0.3380	1.0010	1.3057	1.6049	1.5242	1.2820	0.6846	0.6695
307.5	0.0011	0.0022	0.0097	0.1421	1.0215	2.1194	2.7243	2.2432	1.6383	0.8482	0.7438
322.5	0.0011	0.0022	0.0022	0.0248	0.3014	1.5317	2.6124	2.1302	1.3498	0.7535	0.6631
337.5	0.0011	0.0011	0.0032	0.0086	0.0269	0.1959	0.7739	1.0753	0.7352	0.5016	0.5038
352.5	0.0011	0.0011	0.0022	0.0065	0.0140	0.0258	0.0388	0.0570	0.0807	0.1432	0.2077

Table 3.1

Continued

Frequency, Hz	0.1120	0.1233	0.1357	0.1493	0.1643	0.1809	0.1991	0.2191	0.2412	0.2655	0.2922	0.3216
Wave Direction, degree	**Variance, ft ^{2}**											
7.5	0.0291	0.0280	0.0495	0.0624	0.0980	0.0560	0.0355	0.0258	0.0388	0.0248	0.0151	0.0312
22.5	0.0054	0.0043	0.0054	0.0075	0.0129	0.0118	0.0183	0.0172	0.0280	0.0194	0.0108	0.0226
37.5	0.0022	0.0032	0.0032	0.0032	0.0032	0.0032	0.0032	0.0032	0.0075	0.0086	0.0054	0.0140
52.5	0.0032	0.0032	0.0032	0.0043	0.0043	0.0043	0.0043	0.0043	0.0032	0.0032	0.0022	0.0086
67.5	0.0043	0.0043	0.0065	0.0065	0.0075	0.0075	0.0075	0.0075	0.0054	0.0054	0.0043	0.0140
82.5	0.0065	0.0075	0.0108	0.0118	0.0151	0.0140	0.0151	0.0161	0.0108	0.0097	0.0065	0.0194
97.5	0.0140	0.0161	0.0280	0.0280	0.0344	0.0312	0.0291	0.0258	0.0140	0.0108	0.0065	0.0205
112.5	0.0388	0.0431	0.0721	0.0603	0.0495	0.0398	0.0301	0.0280	0.0151	0.0097	0.0065	0.0205
127.5	0.0592	0.0775	0.1012	0.0710	0.0484	0.0388	0.0269	0.0258	0.0161	0.0097	0.0065	0.0205
142.5	0.0732	0.0958	0.0915	0.0732	0.0474	0.0355	0.0248	0.0237	0.0172	0.0108	0.0075	0.0215
157.5	0.1001	0.1044	0.0807	0.0818	0.0560	0.0377	0.0280	0.0269	0.0248	0.0140	0.0086	0.0237
172.5	0.0969	0.1066	0.0786	0.0958	0.0797	0.0474	0.0366	0.0312	0.0355	0.0205	0.0118	0.0291
187.5	0.0990	0.1345	0.1044	0.1206	0.1249	0.0624	0.0527	0.0344	0.0441	0.0280	0.0151	0.0344
202.5	0.1916	0.1808	0.1432	0.1528	0.1841	0.0893	0.0678	0.0388	0.0495	0.0323	0.0172	0.0388
217.5	0.3122	0.2239	0.1668	0.1701	0.2239	0.1238	0.0753	0.0463	0.0495	0.0344	0.0183	0.0431
232.5	0.4532	0.3412	0.2562	0.1604	0.2486	0.1442	0.0732	0.0517	0.0495	0.0344	0.0205	0.0474
247.5	0.6555	0.5167	0.2842	0.1981	0.2368	0.1539	0.0721	0.0527	0.0484	0.0344	0.0215	0.0506
262.5	0.9096	0.5673	0.3175	0.2153	0.2314	0.1604	0.0732	0.0527	0.0484	0.0355	0.0226	0.0538
277.5	0.9892	0.6997	0.2863	0.2390	0.2239	0.1572	0.0721	0.0527	0.0474	0.0355	0.0226	0.0549
292.5	0.9192	0.6415	0.2153	0.2207	0.2228	0.1485	0.0700	0.0506	0.0463	0.0344	0.0215	0.0538
307.5	0.8708	0.5716	0.2228	0.1970	0.2164	0.1432	0.0678	0.0474	0.0441	0.0323	0.0205	0.0495
322.5	0.7556	0.5220	0.2530	0.1658	0.2099	0.1432	0.0635	0.0431	0.0409	0.0301	0.0183	0.0452
337.5	0.5317	0.3455	0.1733	0.1421	0.1948	0.1389	0.0570	0.0409	0.0377	0.0280	0.0172	0.0398
352.5	0.2508	0.1711	0.1292	0.1206	0.1636	0.1087	0.0495	0.0323	0.0366	0.0291	0.0172	0.0355

A 3-D plot of the multidirectional wave spectrum is shown in Fig.3.2 and the corresponding spectrum at high frequencies is amplified in Fig.3.3.

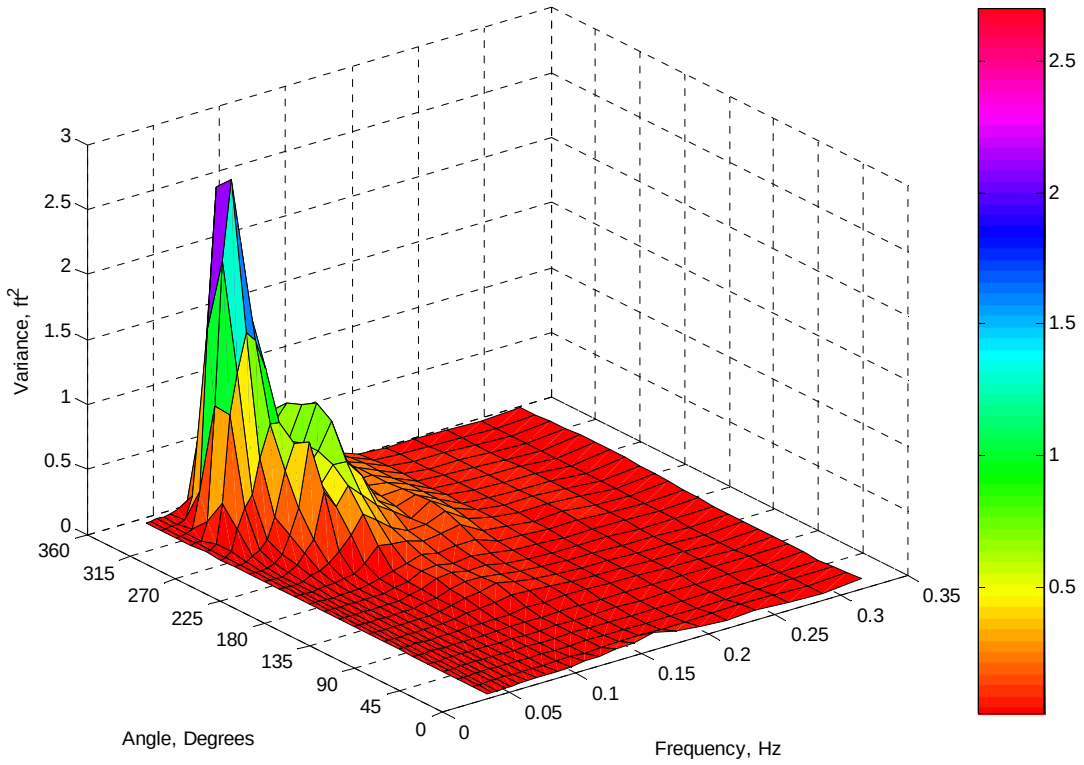

Fig.3.2. Multidirectional wave spectrum.

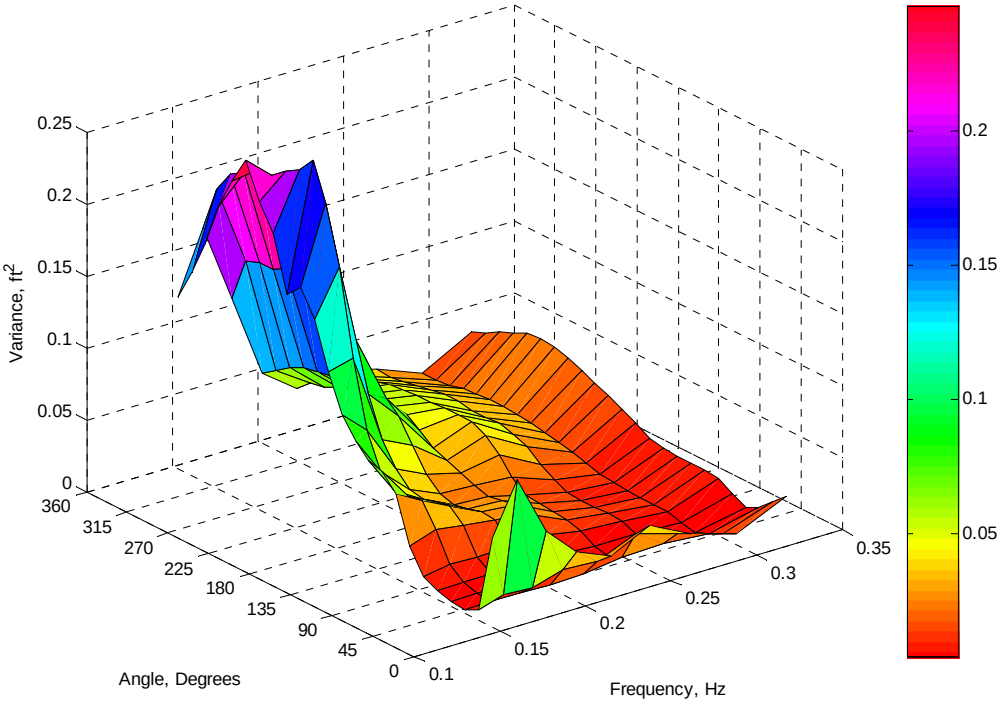

Fig.3.3. Multidirectional wave spectrum at high frequencies.

A description of the hindcast data (Oceanweather Inc., 2006) and the convention for the wind, current, and wave directions adopted in this study are summarized in Table 3.2.

3.2 Coordinates Transformation

The met-ocean conditions and the GPS track of the MODUs are given in a spherical coordinates in terms of latitude and longitude and therefore need to be converted to Cartesian coordinates. The distance $(\mathbf{d})$ between two points (φ_1, λ_1) and (φ_2, λ_2), given their latitude and longitude coordinates, is found by the so-called "Great Circle Formula" (McGovern, 2004):

$$\mathbf{d} = \mathrm{R}\arccos\left[\cos(\mathbf{a})\cos(\mathbf{c}) + \sin(\mathbf{a})\sin(\mathbf{c})\cos(\phi)\right] \tag{3.3}$$

where

$$\phi = (\lambda_2 - \lambda_1)\frac{\pi}{180} \tag{3.4}$$

$$\mathbf{c} = (90^\circ - \varphi_1)\frac{\pi}{180} \tag{3.5}$$

$$\mathbf{a} = (90^\circ - \varphi_2)\frac{\pi}{180} \tag{3.6}$$

The angle made between true north and the great circle passing through the two points at the first point, i.e. the azimuth α can be found by:

$$\alpha = \arcsin\left[\frac{\sin(\mathbf{a})\sin(\phi)}{\sin(\mathbf{b})}\right] \tag{3.7}$$

where

$$\mathbf{b} = \arccos[\cos(\mathbf{a})\cos(\mathbf{c}) + \sin(\mathbf{a})\sin(\mathbf{c})\cos(\phi)] \tag{3.8}$$

The great circle is a circle with origin at the Earth's center and radius R, where $R = 6371.0$ km is the mean radius of the Earth. If the Cartesian coordinates of the first point are set to be $x_1 = 0$ and $y_1 = 0$, then the coordinates of the second point are:

$$\begin{aligned} x_2 &= \mathbf{d}\sin(\alpha) \\ y_2 &= \mathbf{d}\cos(\alpha) \end{aligned} \tag{3.9}$$

Details on the derivation of the "Great Circle Formula" and the inverse transformation, finding the latitude and longitude coordinates of a point given the initial latitude, longitude, distance, and azimuth, are provided in Appendix A-1.

Table 3.2

Hindcast data description

Hindcast Data	**Description**
Wind Direction	To which the wind is blowing, counter clockwise from the positive x-axis (eastward) in degrees (See Fig.3.4).
Wind Speed	30-minutes average at a height of 10 m above the sea level.
Current Direction	To which the currents are traveling, counter clockwise from the positive x-axis (eastward) in degrees.
Current Speed	Vertically averaged storm driven current.
Wave Direction	To which the waves are traveling, counter clockwise from the positive x-axis (eastward) in degrees.
Total Variance	The sum of the variance components of the hindcast spectrum, over the 552 bins.
Significant Wave Height	4.0 times the square root of the total variance.

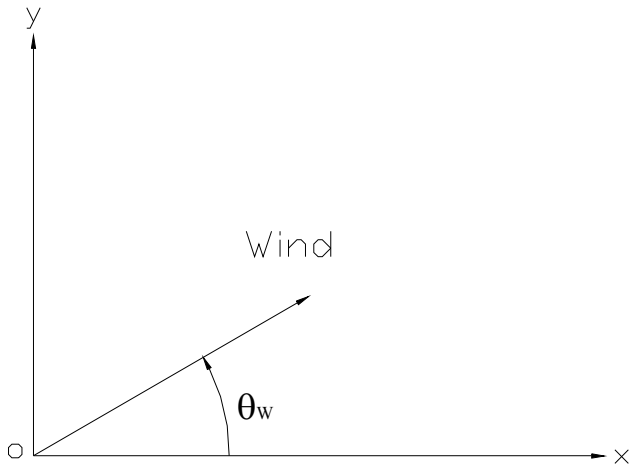

Fig.3.4. Wind, current, and wave directions.

3.3 Added Mass at Infinite Wave Period

The added mass matrix at infinite wave period is computed by using WAMIT:

$$\mathbf{M_{ij}}(\infty) = \overline{\mathbf{M}}_{\mathbf{ij}}(\infty)\rho L^{k} \tag{3.10}$$

where $\overline{\mathbf{M}}_{\mathbf{ij}}(\infty)$ is the non-dimensional added mass matrix (output from WAMIT), ρ the water density, and L the unit length characterizing the body dimensions (input for WAMIT). The coefficient (k) is defined below:

$$\begin{aligned} &k = 3 \quad \text{for} \quad i, j = 1,2,3 \\ &k = 4 \quad \text{for} \quad i = 1,2,3 \quad \text{and} \quad j = 4,5,6 \\ &k = 4 \quad \text{for} \quad i = 4,5,6 \quad \text{and} \quad j = 1,2,3 \\ &k = 5 \quad \text{for} \quad i, j = 4,5,6 \end{aligned} \tag{3.11}$$

3.4 Wind Forces Given the WFC

The wind steady force in surge and sway directions, given the surge and sway wind force coefficients $(C_{Wx}(\theta_W))$ and $(C_{Wy}(\theta_W))$, are computed based on equation (2.49) and given in the form:

$$\begin{aligned} \overline{\mathbf{F}}_{\text{Windx}}(\theta_w) &= \frac{1}{2}\rho_a C_{dw} A_{pw} \cos(\theta_w) U_{W/B}^2 = C_{Wx}(\theta_W) U_{W/B}^2 \\ \overline{\mathbf{F}}_{\text{Windy}}(\theta_w) &= \frac{1}{2}\rho_a C_{dw} A_{pw} \sin(\theta_w) U_{W/B}^2 = C_{Wy}(\theta_W) U_{W/B}^2 \end{aligned} \tag{3.12}$$

where $\vec{U}_{W/B}$ accounts for the relative velocity between the wind and the body and is given by:

$$\vec{U}_{W/B} = \vec{U}_W(z_{CP}) - \frac{d\vec{x}}{dt} \tag{3.13}$$

$\vec{U}_W(z_{CP})$ is the steady wind velocity at the pressure center, extrapolated from the 30-minute average hindcast wind speed at a height of 10 meters $(\vec{U}_{10})$, (Wilson, 2003):

$$\vec{U}_W(z_{CP}) = \vec{U}_{10}\left(\frac{z_{CP}}{10}\right)^{0.125} \tag{3.14}$$

θ_W is the angle between $\vec{U}_{W/B}$ and the positive x-axis of the coordinates fixed on the body. The wind force coefficients at intermediate values of θ_W are interpolated using a cubic spline function.

3.5 Current Force Given the CFC

The current steady forces in surge and sway directions, given the surge and sway current force coefficients $(C_{Cx}(\theta_C))$ and $(C_{Cy}(\theta_C))$, are computed based on equation (2.50) and given in the form:

$$\begin{aligned}\overline{\mathbf{F}}_{Currentx}(\theta_C) &= \frac{1}{2}\rho C_{dc} A_{pc} \cos(\theta_C) U_{C/B}^2 = C_{Cx}(\theta_C) U_{C/B}^2 \\ \overline{\mathbf{F}}_{Currenty}(\theta_C) &= \frac{1}{2}\rho C_{dc} A_{pc} \sin(\theta_C) U_{C/B}^2 = C_{Cy}(\theta_C) U_{C/B}^2\end{aligned} \tag{3.15}$$

where $\vec{U}_{C/B}$ accounts for the relative velocity between the current and the body and is given by:

$$\vec{U}_{C/B} = \vec{U}_C - \frac{d\vec{x}}{dt} \tag{3.16}$$

$\vec{U}_C$ is the vertically averaged storm driven hindcast current velocity and θ_C the angle between $\vec{U}_{C/B}$ and the positive x-axis of the coordinates fixed on the body. The current force coefficients at intermediate values of θ_C are interpolated using a cubic spline function.

3.6 Wave Mean Drift Forces

As mentioned earlier, a multi-directional wave spectrum is given on a set of grids of a much greater size than that of the significant wave height, peak period, and wave vector-mean direction. Therefore, the computation of the wave mean force is based on the significant wave height, peak period, and mean wave direction. That is, the wave mean force is calculated based on an energy density (uni-directional) spectrum, such as Pierson-Moskowitz (P-M) or JONSWAP spectrum, which is described by the significant wave height and peak period. However, it was found that wave spreading may significantly reduce the magnitude of the resultant wave force and the direction of the resultant wave mean force may be different from the wave mean direction. Hence, the magnitude and direction of the wave mean drift forces computed using multidirectional and the corresponding uni-directional wave spectra are compared and corresponding corrections are made to account for the multidimensionality of the spectrum. The procedure is described below.

3.6.1 Wave Mean Drift Forces Using Unidirectional Wave Spectrum

In using a unidirectional wave spectrum the wave mean drift forces are computed by equation (2.32) given in the form:

$$\mathbf{F}_{WMDF}(\beta) = \sum_{j=1}^{N} A_j^2 \mathbf{Q}(\beta, f_j) \tag{3.17}$$

where β is the incident wave angle, A_j the amplitude of the j^{th} wave component, $\mathbf{Q}(\beta, f_j)$ the force transfer functions and f_j the frequency of the j^{th} wave component. The amplitude square $\left(A_j^2\right)$, of the j^{th} wave component is computed by equation (2.26) and is given in the form:

$$A_j^2 = 2S(f)\Delta f \tag{3.18}$$

where $S(f)$ is the wave energy density spectrum and Δf is the bandwidth.

3.6.1.1 Unidirectional Wave Spectra

There are several wave models for describing the wave energy density spectra and the formulation of the JONSWAP spectrum is given below. A JONSWAP spectrum using Goda's form, which specifies the spectrum in terms of the significant wave height $\left(H_S\right)$, peak period $\left(T_p\right)$, and sharp factor $\left(\gamma\right)$ (Goda, 1979) is given by:

$$S(f) = \alpha H_S^2 T_P^{-4} f^{-5} \exp\left[-1.25\left(T_P f\right)^{-4}\right]\gamma^d \tag{3.19}$$

where

$$\alpha = \frac{0.06238}{0.230 + 0.0336\gamma - 0.185\left(1.9 + \gamma\right)^{-1}}\left[1.094 - 0.01915\ln(\gamma)\right] \tag{3.20}$$

$$d = \exp\left[-\frac{\left(T_P f - 1\right)^2}{2\sigma^2}\right] \tag{3.21}$$

$$\sigma = \begin{cases} 0.07 & f \le f_p \\ & , f_p = 1/T_P \\ 0.09 & f > f_p \end{cases} \qquad (3.22)$$

For $\gamma = 1$, a JONSWAP spectrum reduces to a Pierson-Moskowitz spectrum.

A Pierson-Moskowitz spectrum has been chosen for computing the wave mean drift forces, because it fits to the related hindcast wave density spectrum. To demonstrate this, a JONSWAP spectrum with $\gamma = 3.3$, Pierson-Moskowitz spectrum of the same significant wave height and peak period are compared in Fig.3.5 with the corresponding wave density spectrum, which is derived by summing the energy density of different directions, but at the same frequency of the multidirectional spectrum (See Table 3.1).

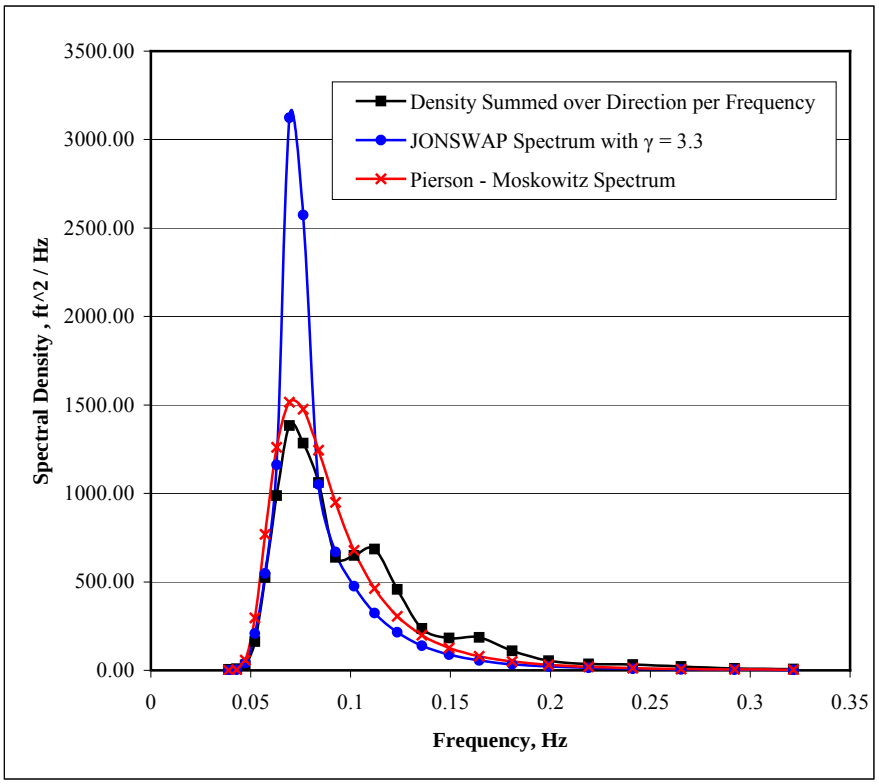

Fig.3.5.Wave spectra comparison.

3.6.1.2 Force Transfer Functions

The force transfer functions $\mathbf{Q}(\beta, f)$ for different incident wave angles (β) at frequency (f) (WAMIT, Inc., 1999) are computed by:

$$\mathbf{Q}(\beta, f) = \frac{\mathbf{F}_{WMDF}(\beta, f)}{A^2} = \overline{\mathbf{F}}_{WMDF}(\beta, f)\rho g L^k \tag{3.23}$$

where $\overline{\mathbf{F}}_{WMDF}(\beta, f)$ are the non-dimensional mean drift forces, which are the output of WAMIT, ρ the water density, g the acceleration due to gravity, and L the unit length characterizing the body dimensions (input for WAMIT). The coefficient k is defined as: $k = 1$ when computing the forces and $k = 2$ for the moments. A plot of the wave mean drift force coefficient $\mathbf{Q}(\beta, f)$ as a function of the frequency $(f)$is shown in Fig.3.6.

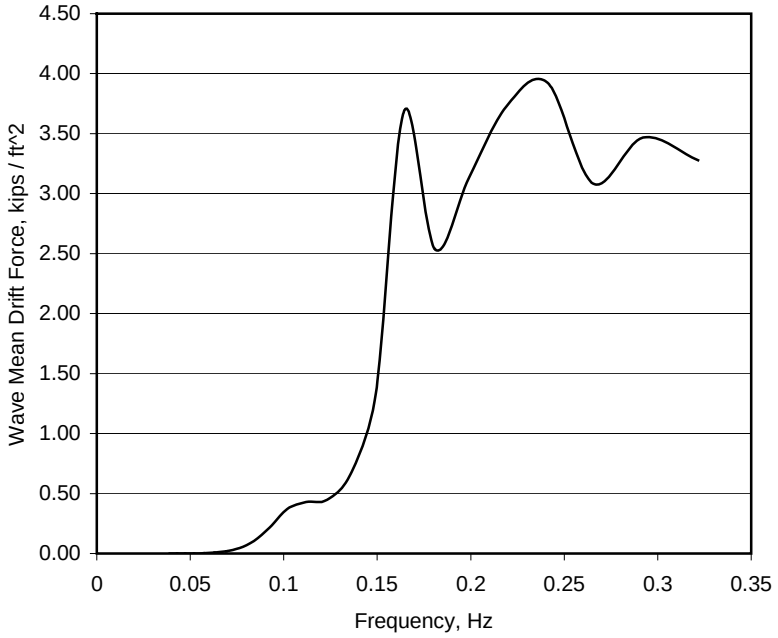

Fig.3.6. MODU I surge wave mean drift force coefficient, β = 300.

3.6.2 Wave Mean Drift Forces Using a Multidirectional Wave Spectrum

Based on a multidirectional wave spectrum the wave mean drift forces are computed by using the double summation expression of equation (3.17):

$$\mathbf{F}_{\text{WMDF}} = \sum_{i=1}^{M}\sum_{j=1}^{N} A_{ij}^2 \mathbf{Q}(\beta_i, f_j) \tag{3.24}$$

where M is the number of the wave direction components at each discrete frequency, N the number of the wave frequency components, and A_{ij}^2 the amplitude square at the i^{th} wave direction component and the j^{th} wave frequency component.

3.7 Viscous Yaw Damping Moment

A very simplified approach is used in computing the MODU's viscous yaw damping moment. The MODU's structure is approximated by equivalent cylinders and the viscous yaw damping moment is derived by using the cross-flow principle (Faltinsen, 1990). The derivation of the viscous yaw damping moment for a cylindrical member is given in Appendix A-2.

3.8 Numerical Integration in Time

In general, the 6-DOF motion equation can be written in the form given below:

$$\widetilde{\mathbf{A}}\ddot{\mathbf{x}}(t) + \widetilde{\mathbf{B}}\dot{\mathbf{x}}(t) + \mathbf{C}\mathbf{x}(t) = \widetilde{\mathbf{F}}(t) \tag{3.25}$$

where $\widetilde{\mathbf{A}}$ is the combined added mass and body mass matrix, $\widetilde{\mathbf{B}}$ is the damping matrix, $\mathbf{C}$ is the hydrostatic stiffness matrix, and $\widetilde{\mathbf{F}}(t)$ represents all external forces. Consequently, the motion equation at $(n+1)^{th}$ time step is of the following form:

$$\widetilde{\mathbf{A}}^{(n+1)}\ddot{\mathbf{x}}^{(n+1)} + \widetilde{\mathbf{B}}^{(n+1)}\dot{\mathbf{x}}^{(n+1)} + \mathbf{C}^{(n+1)}\mathbf{x}^{(n+1)} = \widetilde{\mathbf{F}}^{(n+1)} \tag{3.26}$$

which is solved using Newmark-β method (Wood, 1990; Argyris and Mlejnek, 1991). The procedure is described below.

The predictors $\mathbf{x}^{(n+1)}$, $\dot{\mathbf{x}}^{(n+1)}$, and $\ddot{\mathbf{x}}^{(n+1)}$ at time step $(n+1)$ are given by:

$$\begin{aligned}
\ddot{\mathbf{x}}^{(n+1)} &= \ddot{\mathbf{x}}^{(n)} \\
\dot{\mathbf{x}}^{(n+1)} &= \dot{\mathbf{x}}^{(n)} + \Delta t(1-\gamma)\ddot{\mathbf{x}}^{(n)} + \Delta t\gamma\ddot{\mathbf{x}}^{(n+1)} \\
\mathbf{x}^{(n+1)} &= \mathbf{x}^{(n)} + \Delta t\dot{\mathbf{x}}^{(n)} + \Delta t^2(\frac{1}{2}-\beta)\ddot{\mathbf{x}}^{(n)} + \Delta t^2\beta\ddot{\mathbf{x}}^{(n+1)}
\end{aligned} \tag{3.27}$$

where Δt is the time step. The typical value for γ is chosen to be 0.5 and the values for β in the interval $1/6 \le \beta \le 1/4$ satisfy the stability and accuracy requirements (Chopra, 2001). It should be noted that $\gamma = 1/2$ and $\beta = 1/4$ corresponds to the assumption of constant average acceleration, while $\gamma = 1/2$ and $\beta = 1/6$ corresponds to the assumption of linear variation of the acceleration. $\gamma = 1/2$ and $\beta = 1/4$ are used in this study. During the first time step $(1\Delta t)$ initial conditions $\mathbf{x}^{(0)}$, $\dot{\mathbf{x}}^{(0)}$, and $\ddot{\mathbf{x}}^{(0)}$ at time $t = 0$, are given as input. Thus, $\dot{\mathbf{x}}^{(0)}$ are estimated from the MODU's GPS data and $\ddot{\mathbf{x}}^{(0)}$ is assumed to be zero.

The correctors $\mathbf{x}^{(n+1)}$, $\dot{\mathbf{x}}^{(n+1)}$, and $\ddot{\mathbf{x}}^{(n+1)}$ at time step $(n+1)$ are given by:

$$\begin{aligned}
\mathbf{x}^{(n+1)} &= \mathbf{x}^{(n+1)} + \delta\mathbf{x}^{(n+1)} \\
\dot{\mathbf{x}}^{(n+1)} &= \dot{\mathbf{x}}^{(n+1)} + \frac{\gamma}{\beta\Delta t}\delta\mathbf{x}^{(n+1)} \\
\ddot{\mathbf{x}}^{(n+1)} &= \ddot{\mathbf{x}}^{(n+1)} + \frac{1}{\beta\Delta t^2}\delta\mathbf{x}^{(n+1)}
\end{aligned} \tag{3.28}$$

where $\delta\mathbf{x}^{(n+1)}$ is found by solving the following equation:

$$\left[\frac{1}{\Delta t^2\beta}\widetilde{\mathbf{A}}+\frac{\gamma}{\Delta t\beta}\widetilde{\mathbf{B}}+\mathbf{C}\right]^{(n+1)}\delta\mathbf{x}^{(n+1)}=\widetilde{\mathbf{F}}^{(n+1)}-\widetilde{\mathbf{A}}\ddot{\mathbf{x}}^{(n+1)}-\widetilde{\mathbf{B}}\dot{\mathbf{x}}^{(n+1)}-\mathbf{C}\mathbf{x}^{(n+1)} \quad (3.29)$$

Iteration is required until the difference in $\delta\mathbf{x}^{(n+1)}$ of two consecutive iterations is smaller than a prescribed error tolerance.

Consistent with the met-ocean conditions (wind, current, and wave) during hurricane Katrina, provided from Oceanweather Inc., the hindcast data is updated every 15 minutes during the simulation of the drift of the MODUs. That is, the met-ocean conditions are kept constant during every 15-minute simulation. However, the wind, current, and wave forces vary every time step due to the yaw motion of the MODU. This is because of the dependence of the wind, current, and mean wave force coefficients on the yaw angle (See equations 3.12, 3.15 and 3.24). It should be noted that the yaw moments due to the steady wind and current forces are not considered in this study, because of the lack of data from the respective model tests. The MODU's rotation in yaw direction is only induced by the wave mean yaw moment computed using WAMIT.

Ramp function, is applied to the external forces when updating the met-ocean conditions every 15 minutes. That is, at the beginning of every 15-minute simulation the wind, wave, and current forces are built up smoothly from their values at the previous time step $\left(\mathbf{F}^{(n-1)}\right)$ to their full values $\left(\mathbf{F}^{(n)}\right)$ by using:

$$\mathbf{F}^{(n)}=\mathbf{F}^{(n-1)}+\left(\mathbf{F}^{(n)}-\mathbf{F}^{(n-1)}\right)\left[1-\cos\left(\pi\ t_1/t_{ramp}\right)\right]/2 \quad (3.30)$$

where t_{ramp} is the duration of time for which the ramp function is applied and $t_1=0,..t_{ramp}$ ($t_1=0$ at the beginning of every 15 minutes simulation).

A convergence test to find the sufficient in term of accuracy and economy step size (Δt) was conducted for the drift of MODU I and II. It was found that a step size of

$\Delta t = 0.1$ s gives satisfactory agreement between the drift of the MODUs, simulated with $\Delta t = 0.1$ s and the one simulated with reduced step size.

4. MODU DRIFT PREDICTIONS

Two typical semi-submersible MODUs, one of triangular and the other of rectangular waterline planes are named as ”Generic MODU I” and ”Generic MODU II”, respectively. Their drift during hurricane Katrina was simulated using program “DRIFT”. The predicted drift was then compared with the corresponding measured trajectories recorded by GPS.

Two types of prediction of the MODU’s drift were made and compared with the corresponding measured trajectories:

- MODU’s drift prediction with every 30 minutes correction of the trajectory, i.e. each 30 minutes the simulation of the drift starts from the measured trajectory;
- Continuous MODU’s drift prediction without correction.

4.1 MODU Properties

Both, MODU I and II have semi-submersible hulls. MODU I has a triangular waterline plane and consists of three columns and three pontoons, while MODU II has two parallel waterline planes and consists of four columns and two pontoons. The properties of MODU I and II are summarized in Table 4.1.

4.2 MODU Hull Discretization

A constant panel method (WAMIT, Inc., 1999) is used in discretizing the hull of the MODUs. That is, the geometry of the body is represented by many flat quadrilateral panels and the solution for the velocity potential is approximated by a piecewise constant value on each panel.

The hulls of MODU I and II were discretized into 1608 and 1672 panels, respectively and provided by our industry partners (Zimmerman, 2006).

Table 4.1

MODU properties

Properties	MODU I	MODU II	Units
Total Displacement	59376.0	121585.9	kips
Volume	927369.5	1899000.0	ft^3
Transverse Metacentric Height GMT	12.5	31.2	ft
Longitudinal Metacentric Height GML	12.5	92.6	ft
Vertical Center of Buoyancy KB (from water line)	-42.9	-37.0	ft
Vertical Center of Gravity VCG (from water line)	21.0	-9.0	ft
Waterplane Area	5769.0	16800.0	ft^2
Mean Draft	58.5	60.0	ft
Roll Gyradius	105.0	100.0	ft
Pitch Gyradius	110.0	110.0	ft
Yaw Gyradius	120.0	120.0	ft

All three forms of the submerged volume of the body can be evaluated in using the different WAMIT approaches given below:

$$\nabla_X = -\iint_{Sb} n_1 x dS \tag{4.1}$$

$$\nabla_Y = -\iint_{Sb} n_2 y dS \tag{4.2}$$

$$\nabla_Z = -\iint_{Sb} n_3 z dS \tag{4.3}$$

$$\nabla = \nabla_X = \nabla_Y = \nabla_Z \tag{4.4}$$

where S_b is the body's wetted surface at its mean position and $\mathbf{n} = (n_1, n_2, n_3)$ the unit normal vector. If the hull discretization is done correctly, the three evaluations of the

volume $(\nabla_X, \nabla_Y, \nabla_Z)$ should be identical. In addition, one can compare the hydrostatic stiffness in heave $(C(3,3))$, roll $(C(4,4))$, and pitch $(C(5,5))$ directions computed by equations (2.38 and 2.40) with the one obtained directly from WAMIT.

The wave mean drift force coefficients (output from WAMIT) are evaluated by using two different methods: the momentum conservation principle and integration of the pressure over the wetted body surface. If sufficient number of grid panels is used in discretizing the hull, the force transfer functions evaluated by the two methods should be identical.

For comparison, the submerged volume and hydrostatic stiffness in heave, roll, and pitch directions of MODU I and II were computed and are summarized in Table 4.2. The satisfactory agreement demonstrated in these tables indicates that the computation of hydrostatic forces is accurate.

Table 4.2

MODU hydrostatic data comparison

Equation	Hydrostatic Data	MODU I	MODU II	Units
WAMIT output	∇_X	927754.0	1893000.0	ft^3
	∇_y	927755.0	1893000.0	ft^3
	∇_Z	927758.0	1893000.0	ft^3
Table 4.1	∇	927369.5	1899000.0	ft^3
WAMIT output	C(3,3)	369356.3	1075641.2	lb/ft
2.38	C(3,3)	369367.5	1075641.2	lb/ft
WAMIT output	C(4,4)	7.40E+08	3.80E+09	lb.ft
2.40	C(4,4)	7.42E+08	3.80E+09	lb.ft
WAMIT output	C(5,5)	7.49E+08	1.13E+10	lb.ft
2.40	C(5,5)	7.42E+08	1.13E+10	lb.ft

The wave mean drift force coefficients of MODU I and II, estimated by the moment conservation and pressure integration, were obtained as a function of wave frequency for different incident wave angles (β), ranging from $0°$ to $180°$ with an increment of $\Delta\beta = 7.5°$. The comparison shows a satisfactory agreement in the coefficients evaluated by the two methods. For example, the plots of the wave mean drift force coefficients (surge, sway, and yaw) of MODU I for $\beta = 22.5$ are shown in Fig.4.1 through Fig.4.3.

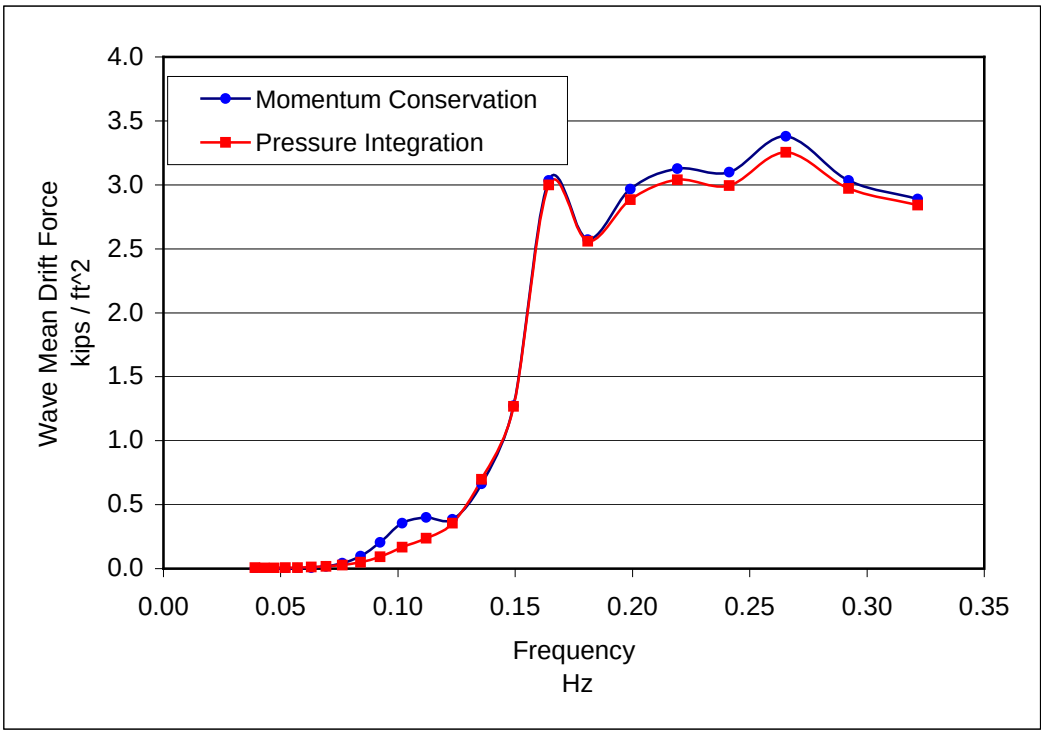

Fig.4.1. MODU I surge wave mean drift force coefficients, $\beta = 22.5°$.

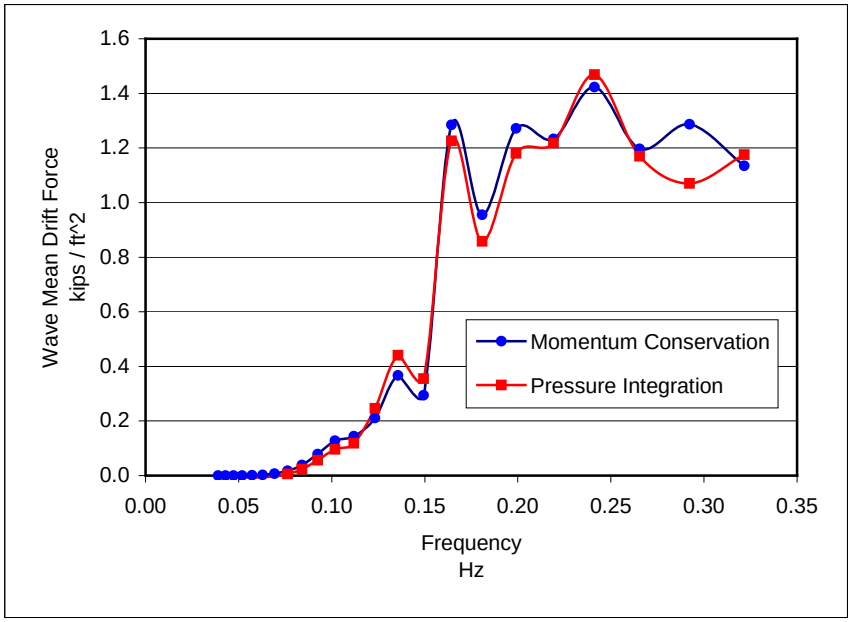

Fig.4.2. MODU I sway wave mean drift force coefficients, $\beta = 22.5°$.

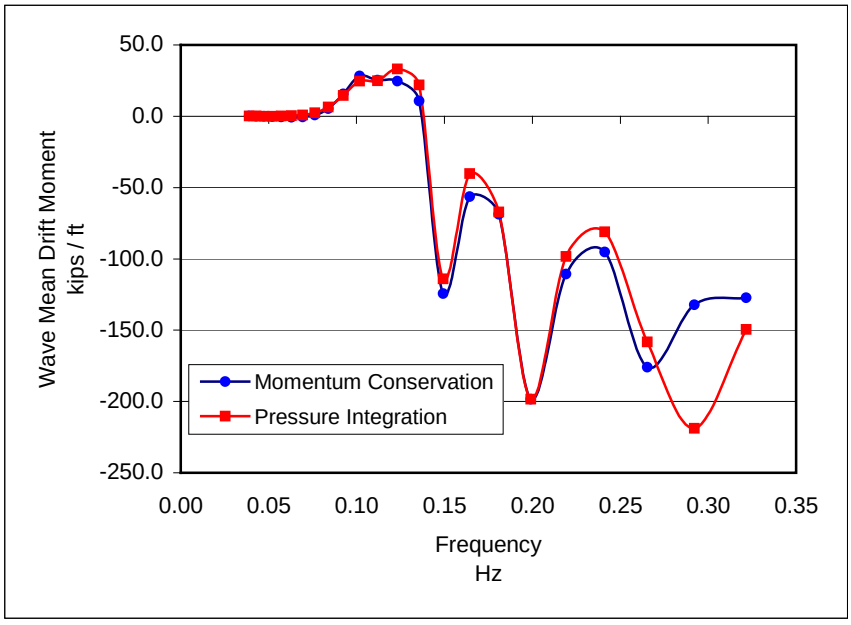

Fig.4.3. MODU I yaw wave mean drift force coefficients, $\beta = 22.5°$.

4.3 MODU Wave Mean Drift Forces

In this study, the wave mean drift force coefficients evaluated based on the moment conservation principle are used in computing the wave mean drift forces. This is because the momentum conservation principle is, in general, more accurate than the pressure integration owing to its independence on local velocities at the body surface (WAMIT, Inc., 1999). For reference, the wave mean drift force coefficients of MODU I and II as a function of the wave frequency and incident wave angle, ranging from $0°$ to $180°$ with an increment of $\Delta\beta = 22.5°$ are presented in Appendix A-3.

As discussed in Section 3, the magnitude and direction of the wave mean forces computed using multidirectional spectrum and the corresponding Pierson-Moskowitz wave spectrum were compared. Based on the comparison, corrections on the magnitude and direction of the wave mean force are made to account for the multidimensionality of the spectrum. It is noticed that directional spreading reduces the magnitude of the resultant wave mean force. In addition there is a difference between the directions of the wave mean force computed by the two spectra. The factors contributing for this difference are explained below.

As shown in Fig.3.6, for example, the wave mean drift force coefficients depend on the wave frequency and are much greater at relative high frequencies (0.15 – 0.33 Hz) than near the spectral peak. Although wave energy is much greater near the spectral peak than at relatively high frequencies, the contribution to the resultant wave mean force from waves at relatively high frequencies is still significant. As shown in Table 3.1, the directions of wave components at high frequencies are noticeably different from those near the spectral peak, while the latter dictates the mean wave direction. Thus, the direction of the resultant wave force can be different from the mean wave direction. Furthermore, wave spreading reduces the magnitude of the wave force, especially at high frequencies where the spreading is generally greater. Therefore, the reduction in the wave force due to wave spreading must be accounted accordingly. The corrections are made by comparing the directions and magnitudes of the wave mean force computed, respectively, by using a multi-directional spectrum and the corresponding

energy density spectrum on the same grid. The corrections are then applied to the computation of wave forces at other grids nearby. In this study, it was found that the correction on the direction of the wave force ranges from 5 to 30 degrees and the correction on the magnitude of the wave force ranges from 20- 40 % of the wave force.

4.4 MODU Wind and Current Force Coefficients

The wind and current force coefficients, needed for computing the wind and current forces (Equations 3.12 and 3.15) were obtained from respective model tests and provided by our industry partners (Zimmerman, 2006). These coefficients, as a function of the yaw angle, are given in Tables 4.3 and 4.4. Because of the symmetry of the hulls with respect to the x-axis, only the values for yaw angles from 0° to 180° are given. The plots of the wind and current force coefficients as a function of the yaw angle are given in Appendix A-4. The subscripts 'w' and 'c' stand for wind and current, respectively, and 'x' and 'y' indicate the directions in the x- and y- axis.

Table 4.3

MODU I wind and current force coefficients

Angle	**Cwx**	**Cwy**	**Ccx**	**Ccy**
degree	$lb/(ft/s)^2$	$lb/(ft/s)^2$	$lb/(ft/s)^2$	$lb/(ft/s)^2$
0.0	38	0	11732	0
22.5	33	14	10318	4274
45.0	26	26	7496	7496
67.5	14	33	4188	10111
90.0	0	34	0	10110
112.5	-14	33	-4524	10921
135.0	-25	25	-8052	8052
157.5	-32	13	-9781	4051
180.0	-35	0	-10865	0

Table 4.4

MODU II wind and current force coefficients

Angle	**Cwx**	**Cwy**	**Ccx**	**Ccy**
degree	$lb/(ft/s)^2$	$lb/(ft/s)^2$	$lb/(ft/s)^2$	$lb/(ft/s)^2$
0.0	50	0	8000	0
22.5	47	20	9500	4000
45.0	38	38	10500	10000
67.5	18	45	5000	13000
90.0	0	41	0	11000
112.5	-18	45	-5000	13000
135.0	-38	38	-10500	10000
157.5	-47	20	-9500	4000
180.0	-50	0	-8000	0

4.5 MODU I Drift Predictions

The position of MODU I during the hurricane was recorded by GPS every 30 minutes. The evolution of the hurricane track given in Universal Time (UT) at intervals of 3 hours and the corresponding position of MODU I are depicted in Fig.4.4 to illustrate the position of MODU I with respect to the eye of hurricane Katrina. To conceal the proprietary information, the real longitude and latitude are altered on purpose for this and the following related figures. The GPS track of MODU I in UT and the closest available grid points for the hindcast multidirectional wave spectra are marked in Fig. 4.5.

Because no information about the yaw angles of the MODUs was available, 30-minute simulations of the drift of MODU I and II for different initial yaw angles were carried out to explore whether or not the predicted position is sensitive to the initial yaw.

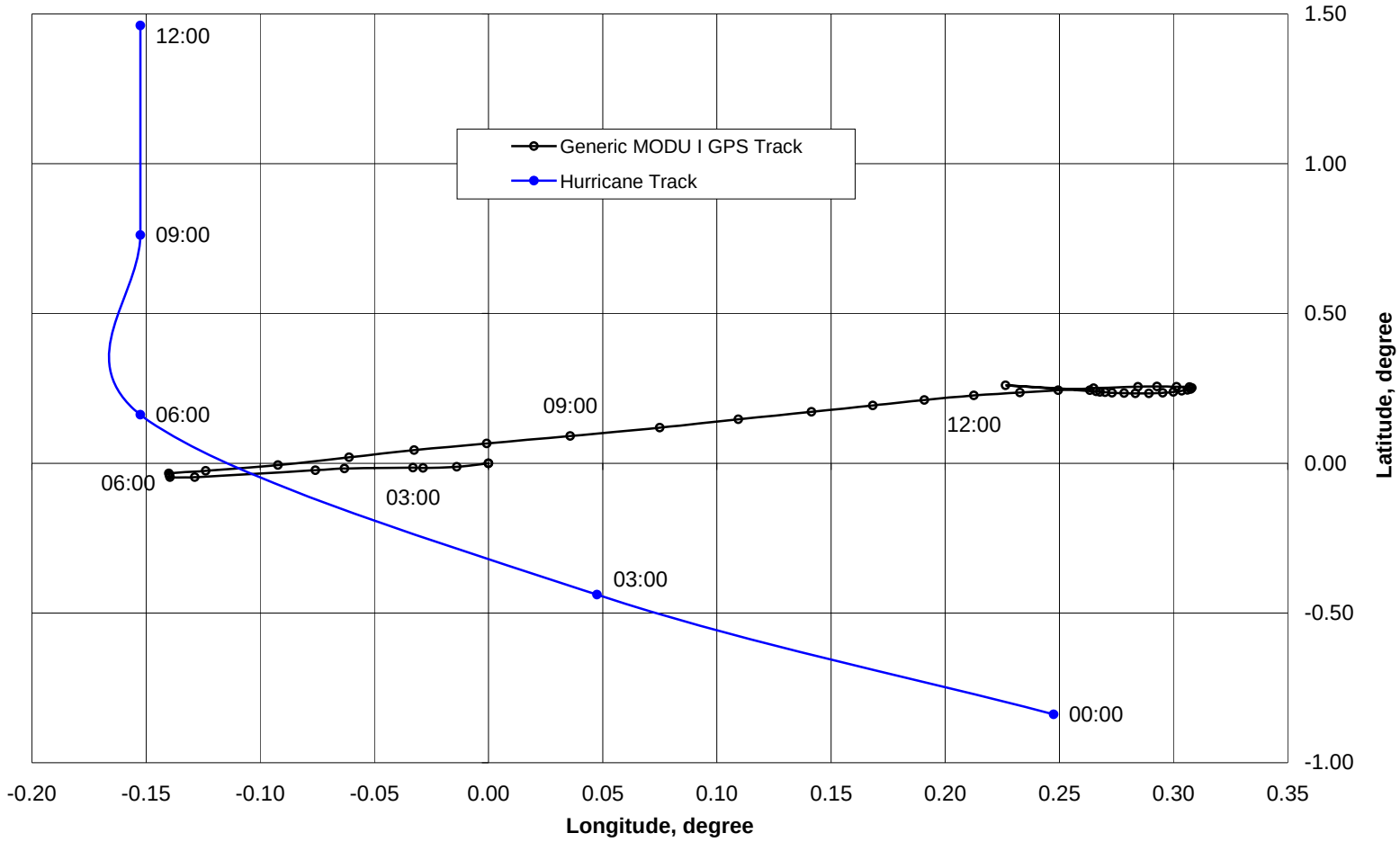

Fig.4.4. MODU I GPS and hurricane tracks.

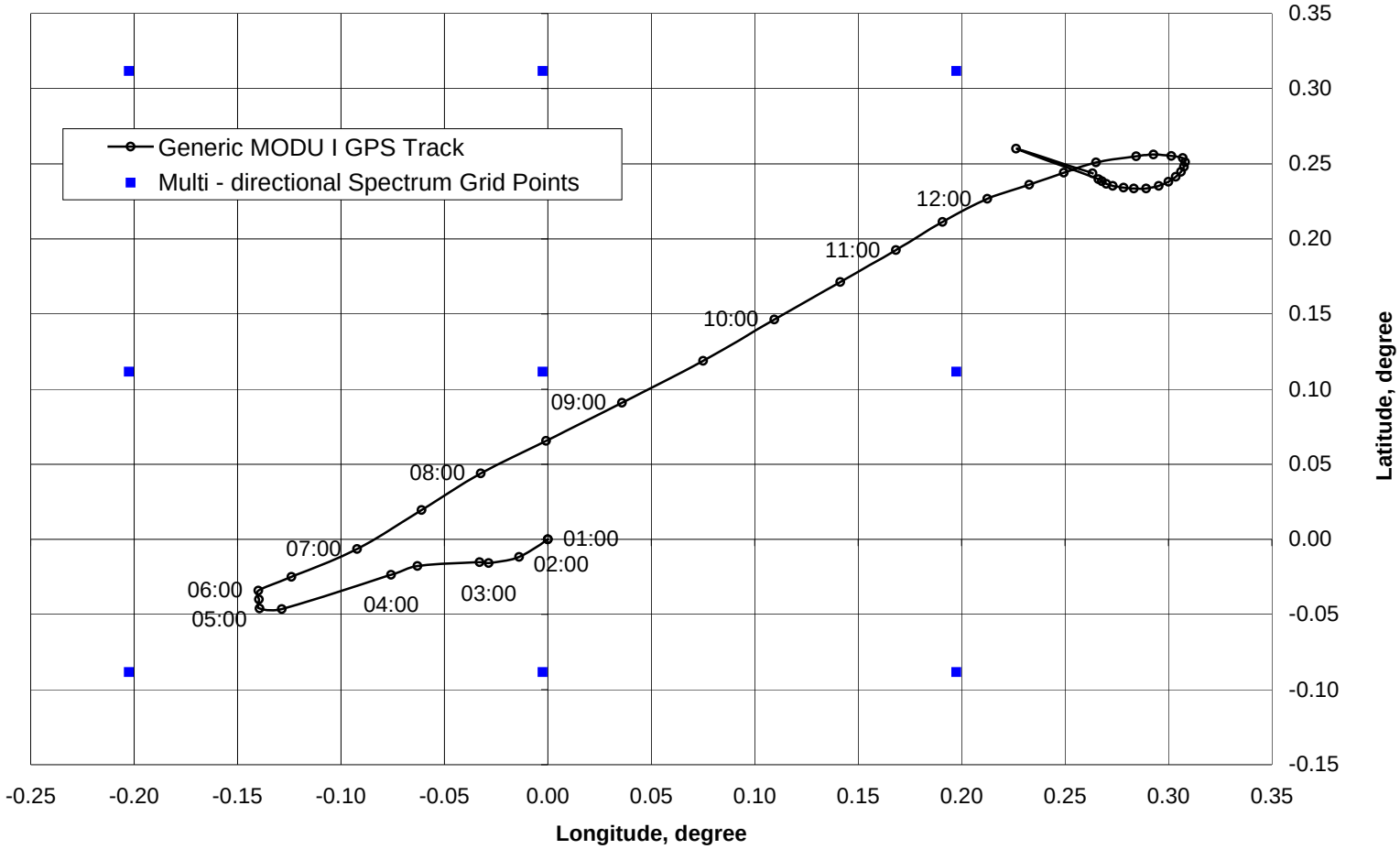

Fig.4.5. MODU I GPS track.

Fig.4.6 shows 30-minute predicted drift of MODU I based on four different initial yaw angles. It indicates that the initial yaw angle has insignificant effect on the predicted drift. This result is expected because MODU I has a nearly equilateral triangular waterplane and the total current and wind forces are not sensitive to the yaw angle.

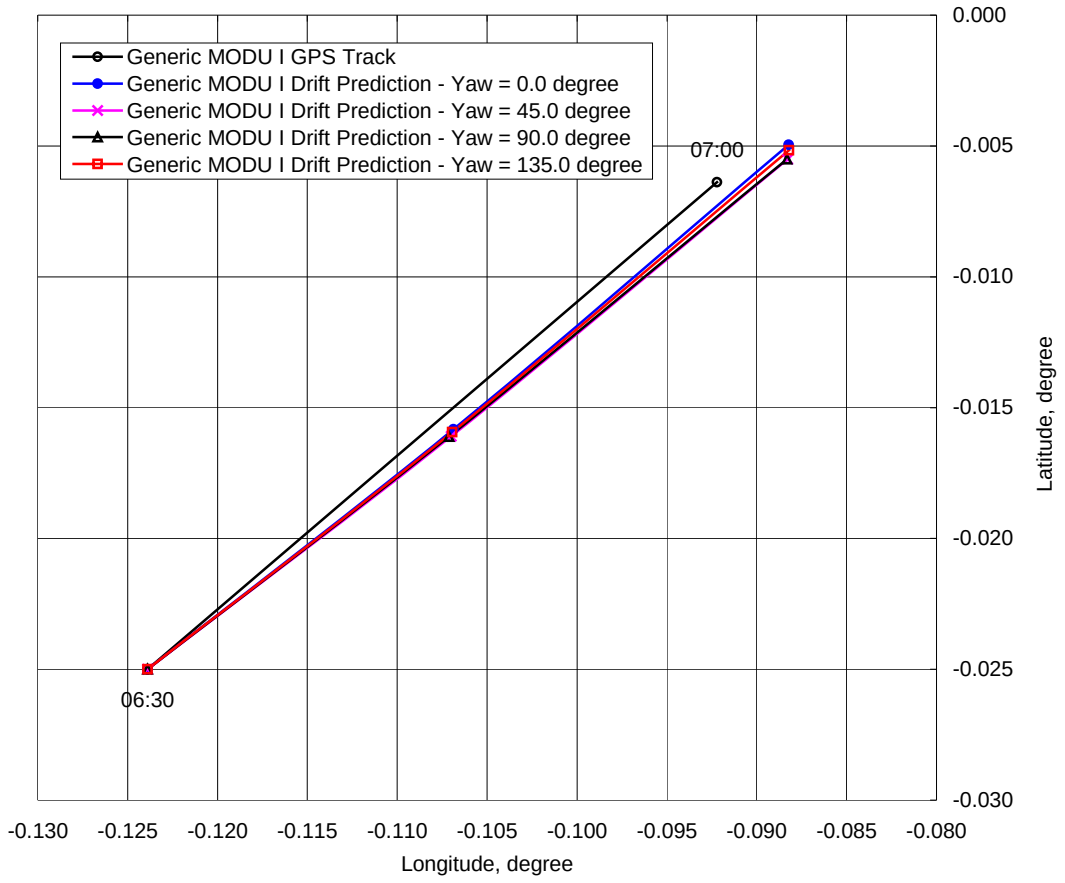

Fig.4.6. MODU I drift prediction for different yaw angles.

The simulation of the drift of MODU I from 06:30 to 12:00 UT during the hurricane with 30-minute corrections is plotted in Fig.4.7. This simulation starts at 06:30 UT (see Fig.4.5) and the hindcast information (wind, wave, and current) is updated every 15 minutes. Every 30 minutes, the simulation of the drift starts at the corresponding measured trajectory recorded by GPS.

The predicted drift of MODU I at the end of each 30-minute simulation is compared with the corresponding measured trajectory. This comparison shows satisfactory agreement. The distance between the measured and predicted position of the MODU at the end of each 30-minute simulation is less than 1 km. The predicted drift of the MODU is further South to its measured trajectory from 06:30 to 08:00 UT and then further North from 08:00 to 12:00 UT.

The corresponding continuous drift prediction is given in Fig.4.8. Here the distance between the predicted position of the MODU at the end of the simulation (12:00 UT) and the corresponding measured position is about 2.5 km. This distance is bigger than the one obtained from the MODU's drift prediction with 30-minute corrections, because the error is accumulated. The predicted drift of the MODU deviates to the South of its measured trajectory from 06:30 to 08:45 UT and then to the North from 08:45 to 12:00 UT. This trend of the predicted MODU's drift is consistent with the one obtained from the prediction with 30-minute corrections.

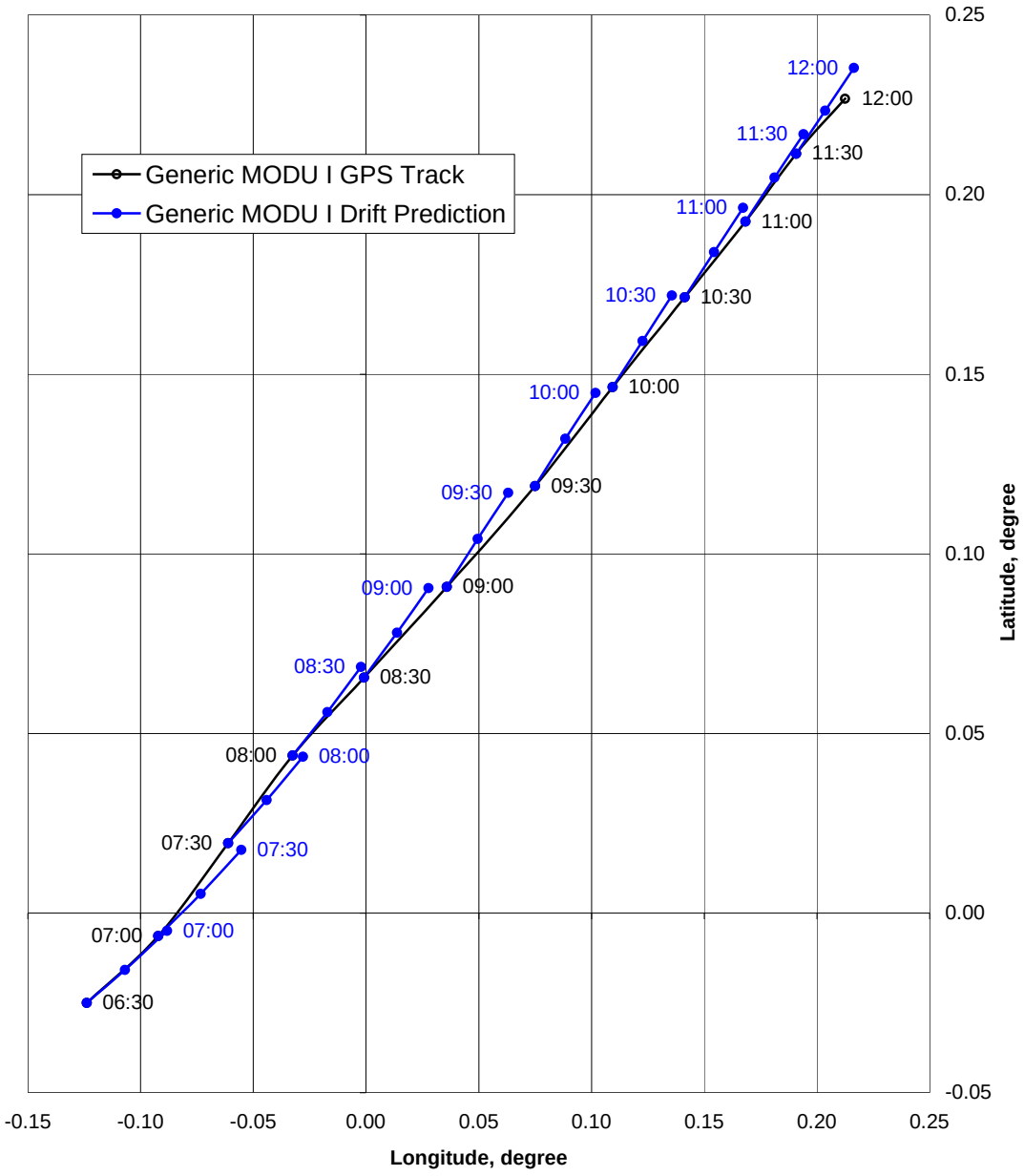

Fig.4.7. MODU I drift prediction with 30-minute corrections.

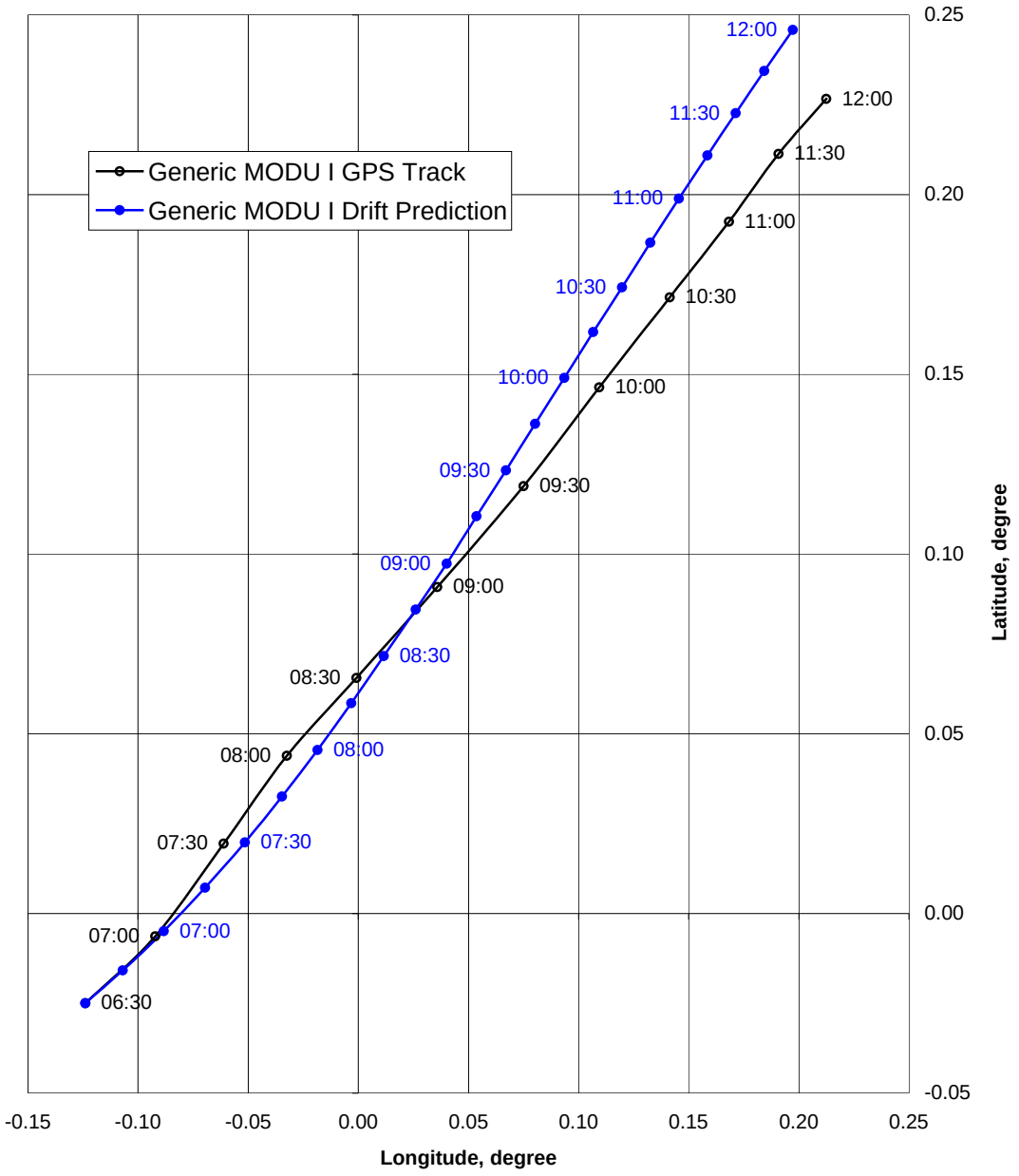

Fig.4.8. MODU I continuous drift prediction.

The magnitude and direction of the external forces applied on MODU I at the end of every 15 minutes during the continuous simulation, are given in Table 4.5. As seen from this table, the wind force dominates the MODU's drift. The wave force ranges

from about 4% to 15% of the respective wind force. It should be noted that in order to compare the external forces, the current force given in Table 4.5 is computed based on the current velocity only. As discussed in Section 3, the hindcast current velocity given as an output in the "Emergency Response Data" is the vertically averaged storm driven current velocity and, in general, significantly underestimates the current velocity near the free surface.

Table 4.5

External forces applied on MODU I during the continuous simulation starting at 06:30

Time	MODU Position		Wind Force		Wave Force		Current Force	
	Latitude	Longitude	Magnitude	Direction	Magnitude	Direction	Magnitude	Direction
UT	degree	degree	kips	degree	kips	degree	kips	degree
6:30	-0.025	-0.124	727.22	29.99	39.03	188.74	3.39	206.37
6:45	-0.016	-0.107	823.62	31.74	34.09	187.07	3.23	204.51
7:00	-0.005	-0.088	884.88	34.10	38.36	179.27	2.96	203.06
7:15	0.007	-0.070	858.61	36.07	33.13	175.19	2.73	200.57
7:30	0.019	-0.052	812.68	37.26	34.91	167.49	2.53	198.10
7:45	0.032	-0.035	776.90	38.54	33.25	161.02	2.39	195.24
8:00	0.044	-0.019	734.20	39.53	33.04	152.67	2.26	192.05
8:15	0.057	-0.004	679.37	40.08	35.60	143.55	2.17	188.64
8:30	0.070	0.011	618.51	40.82	32.43	94.41	2.09	185.30
8:45	0.083	0.025	607.88	41.28	37.05	86.15	1.85	181.53
9:00	0.096	0.039	579.16	41.71	62.02	79.69	1.70	177.42
9:15	0.110	0.053	545.51	41.52	42.20	74.81	1.62	173.29
9:30	0.122	0.066	518.62	41.42	54.84	70.29	1.60	169.51
9:45	0.135	0.080	495.65	41.44	47.77	66.17	1.63	165.94
10:00	0.148	0.093	477.51	41.57	55.28	62.59	1.68	162.79
10:15	0.161	0.107	462.57	41.90	52.78	59.14	1.74	160.15
10:30	0.173	0.120	453.31	41.97	52.41	60.21	1.73	157.94
10:45	0.185	0.133	445.56	41.77	50.46	55.99	1.70	155.95
11:00	0.198	0.146	440.15	41.76	51.98	53.01	1.66	154.39
11:15	0.210	0.159	437.29	41.98	51.93	49.55	1.58	153.09
11:30	0.221	0.173	436.52	42.30	53.25	47.07	1.51	152.08
11:45	0.233	0.186	438.32	42.19	51.69	44.44	1.44	151.21

The directions of wind, wave, and current forces at 30-minute intervals are plotted in Fig.4.9. It should be noted that the vectors given in this and the following similar figures, only depict the directions of the forces. Their lengths do not represent the real magnitude of the forces.

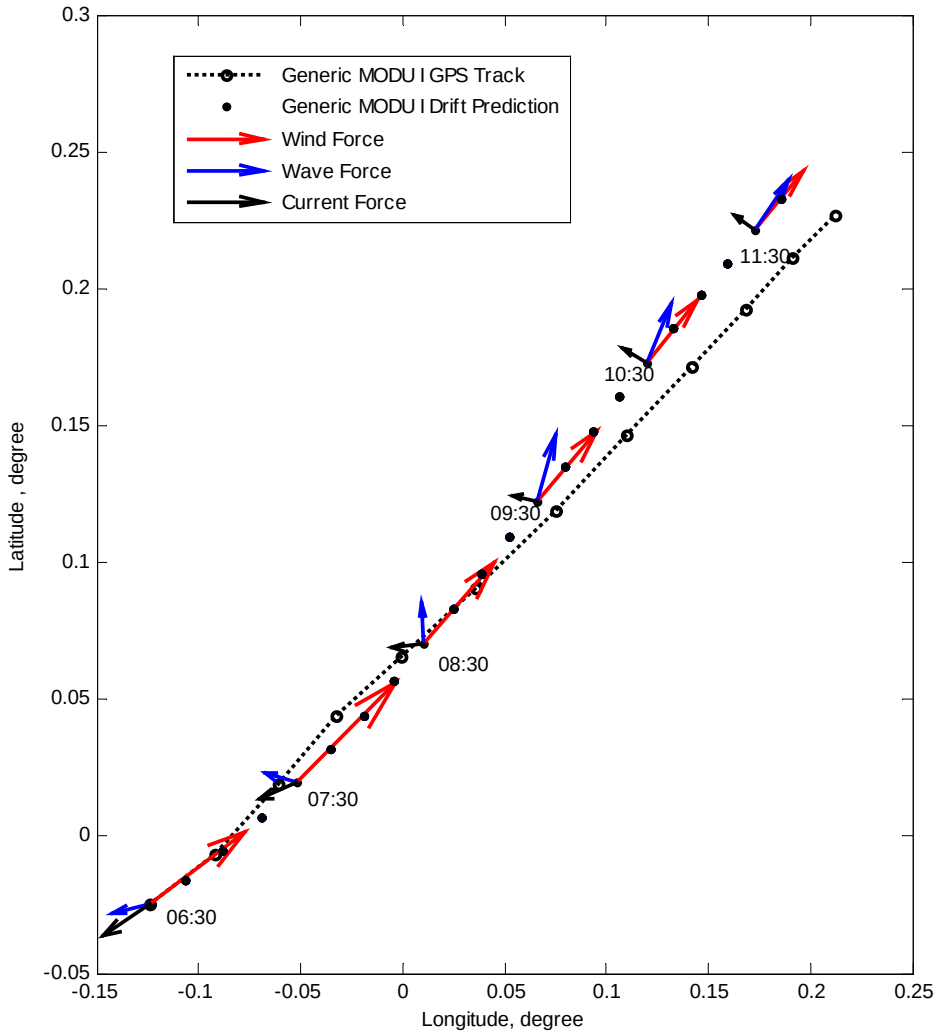

Fig. 4.9. External forces applied on MODU I during the continuous simulation starting at 06:30.

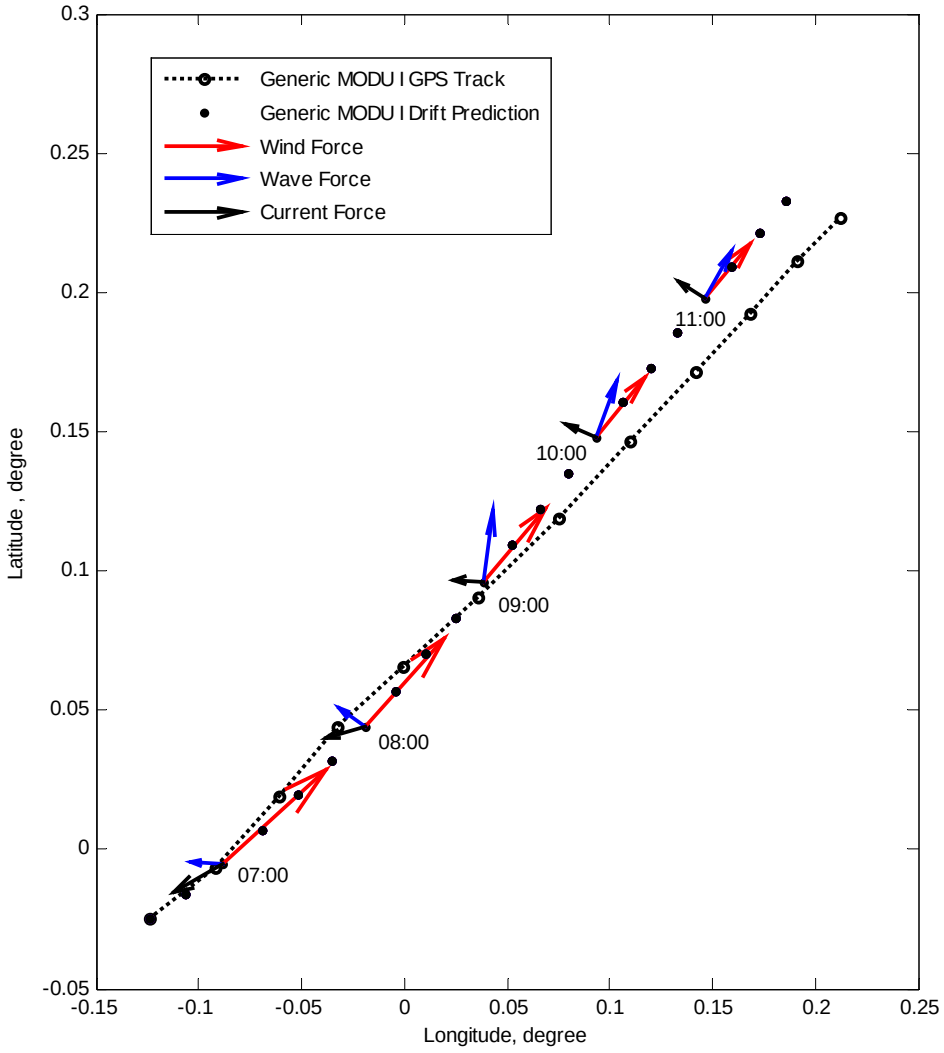

Fig. 4.9. Continued.

For clarity, Fig.4.9 is divided into two parts. The first one shows the direction of the forces for an interval of one hour starting at 06:30 UT, while the second shows the direction of the forces for the same interval but starting at 07:00 UT. The same procedure is used in all figures depicting the force directions.

Continuous drift prediction starting at an earlier time, 04:00 UT, when it is assumed that MODU I began to drift significantly (See Fig.4.5) and ending at 12:00 UT is plotted in Fig.4.10. A low pressure system such as a hurricane rotates counter clockwise in the northern hemisphere. Therefore, considering the relative position of MODU I at 04:00 UT and the corresponding location of the hurricane's eye (See Fig.4.4), one would expect the MODU's drift to be toward the West. Similarly, one would expect the MODU's drift to be toward the Northeast considering the relative position of MODU I, at about 06:00 UT, to the corresponding location of the hurricane's eye. As depicted in Fig.4.10, the simulated MODU's drift starting at 04:00 UT virtually follows the directions mentioned above. However, the recorded trajectory is toward the North and the corresponding prediction is southward at about 05:00 UT. This discrepancy may be caused by the uncertainty related with the hindcast of wind magnitude and direction near the hurricane's eye. The distance between the predicted position of the MODU at the end of the simulation (12:00 UT) and the corresponding measured position is about 2.0 km.

The magnitude and direction of the external forces applied on MODU I at the end of every 15 minutes during this continuous simulation, are summarized in Table 4.6.

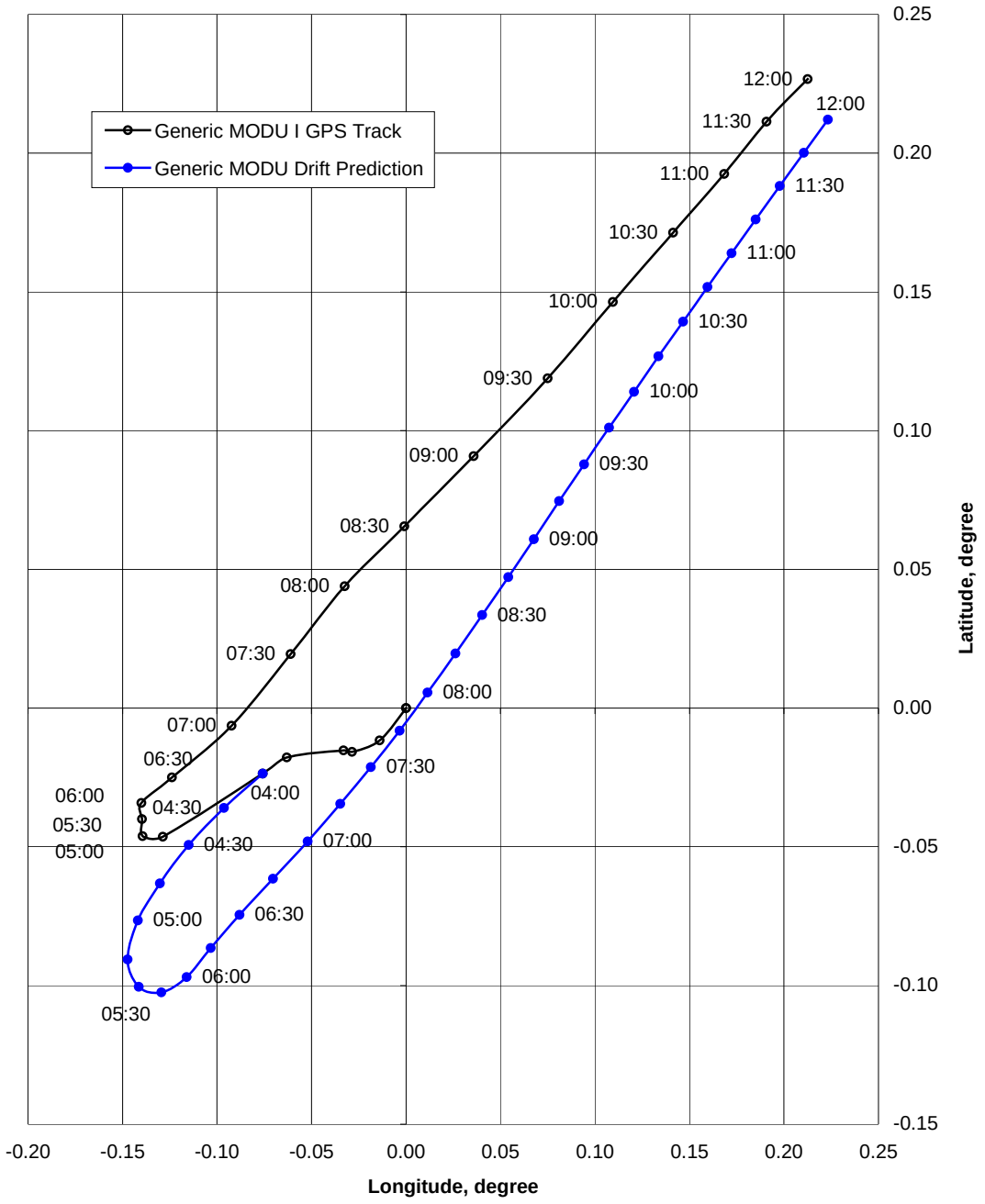

Fig.4.10. MODU I continuous drift prediction starting at 04:00.

Table 4.6

External forces applied on MODU I during the continuous simulation starting at 04:00

Time	MODU Position		Wind Force		Wave Force		Current Force	
	Latitude	Longitude	Magnitude	Direction	Magnitude	Direction	Magnitude	Direction
UT	degree	degree	kips	degree	kips	degree	kips	degree
4:00	-0.024	-0.076	797.85	218.11	75.61	178.53	2.50	201.89
4:15	-0.036	-0.096	640.16	224.62	72.30	179.31	2.73	203.25
4:30	-0.049	-0.115	514.56	233.95	74.95	181.19	2.99	204.58
4:45	-0.063	-0.130	379.99	244.83	78.10	184.50	3.15	205.95
5:00	-0.077	-0.142	328.25	270.15	75.32	187.67	3.25	207.26
5:15	-0.091	-0.147	309.95	324.05	78.30	188.79	3.30	208.72
5:30	-0.100	-0.141	345.85	1.44	76.59	189.50	3.24	209.42
5:45	-0.102	-0.129	441.35	24.70	66.34	188.03	3.19	209.22
6:00	-0.097	-0.116	578.37	38.90	68.50	183.98	3.16	208.12
6:15	-0.086	-0.103	744.72	37.60	58.48	179.42	3.08	206.64
6:30	-0.075	-0.088	890.67	37.13	44.81	185.06	3.01	204.83
6:45	-0.062	-0.070	921.23	37.90	34.25	181.66	2.88	202.27
7:00	-0.048	-0.052	899.76	38.99	37.18	173.04	2.66	200.10
7:15	-0.035	-0.035	838.32	39.88	34.11	167.22	2.45	197.43
7:30	-0.021	-0.019	785.93	40.73	34.21	158.48	2.33	194.35
7:45	-0.008	-0.003	740.63	41.56	34.57	149.99	2.22	191.14
8:00	0.006	0.011	681.98	41.96	32.90	140.23	2.17	187.81
8:15	0.020	0.026	628.83	42.86	38.70	131.50	2.11	184.55
8:30	0.034	0.040	599.49	43.95	42.02	86.25	2.06	181.11
8:45	0.047	0.054	560.33	43.50	43.71	81.39	1.92	177.06
9:00	0.061	0.068	541.65	43.36	60.87	73.90	1.81	173.58
9:15	0.075	0.081	509.08	43.43	47.71	70.35	1.79	169.92
9:30	0.088	0.094	492.14	43.48	59.00	65.88	1.75	166.50
9:45	0.101	0.107	477.63	43.26	49.81	62.27	1.69	163.24
10:00	0.114	0.121	466.69	43.64	58.22	59.68	1.69	160.28
10:15	0.127	0.134	456.01	43.57	51.80	56.24	1.69	157.89
10:30	0.139	0.147	456.07	43.60	55.06	59.00	1.71	155.97
10:45	0.152	0.159	448.63	43.32	51.12	55.07	1.68	154.42
11:00	0.164	0.172	450.29	43.32	55.54	53.34	1.69	153.03
11:15	0.176	0.185	447.66	43.22	52.38	50.45	1.61	151.96
11:30	0.188	0.198	445.31	43.17	56.95	48.03	1.52	151.14
11:45	0.200	0.211	442.01	43.49	52.43	45.44	1.40	150.46

Plots of the corresponding wind, wave, and current directions for every 30 minutes are given in Fig.4.11.

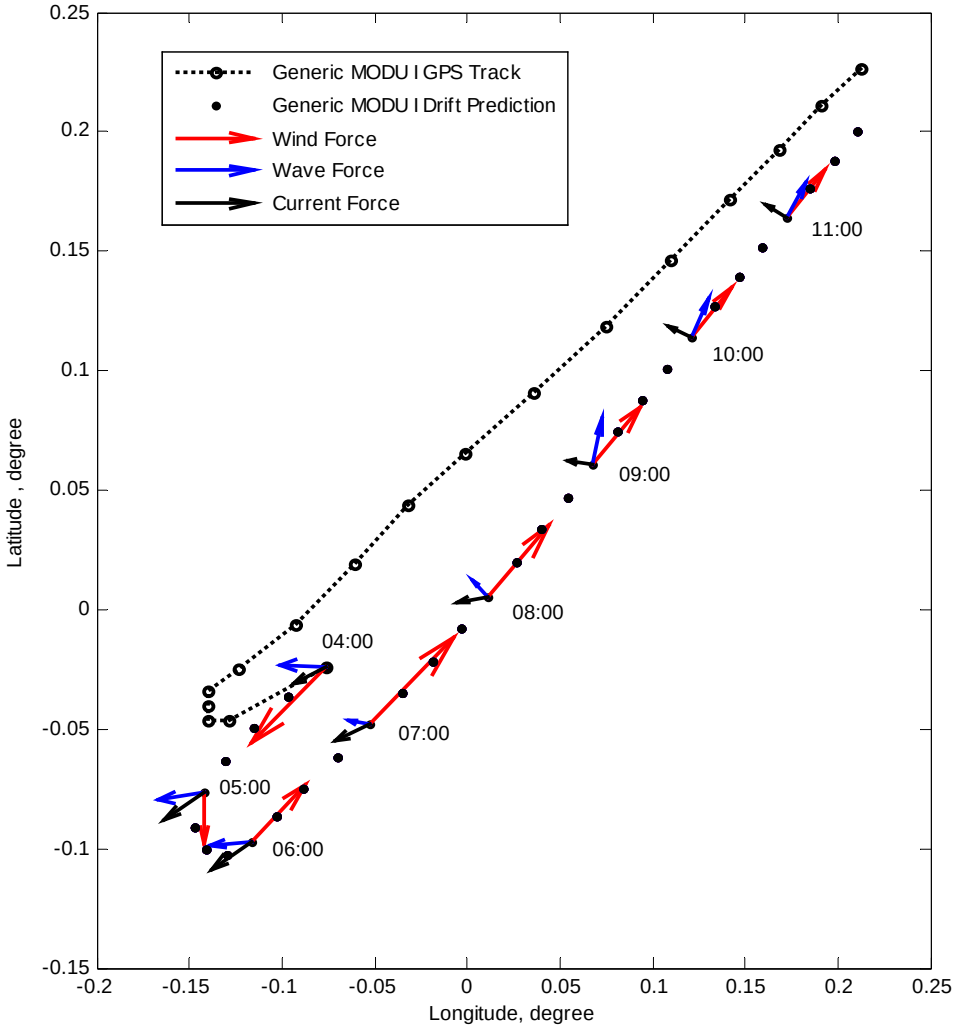

Fig. 4.11. External forces applied on MODU I during the continuous simulation starting at 04:00.

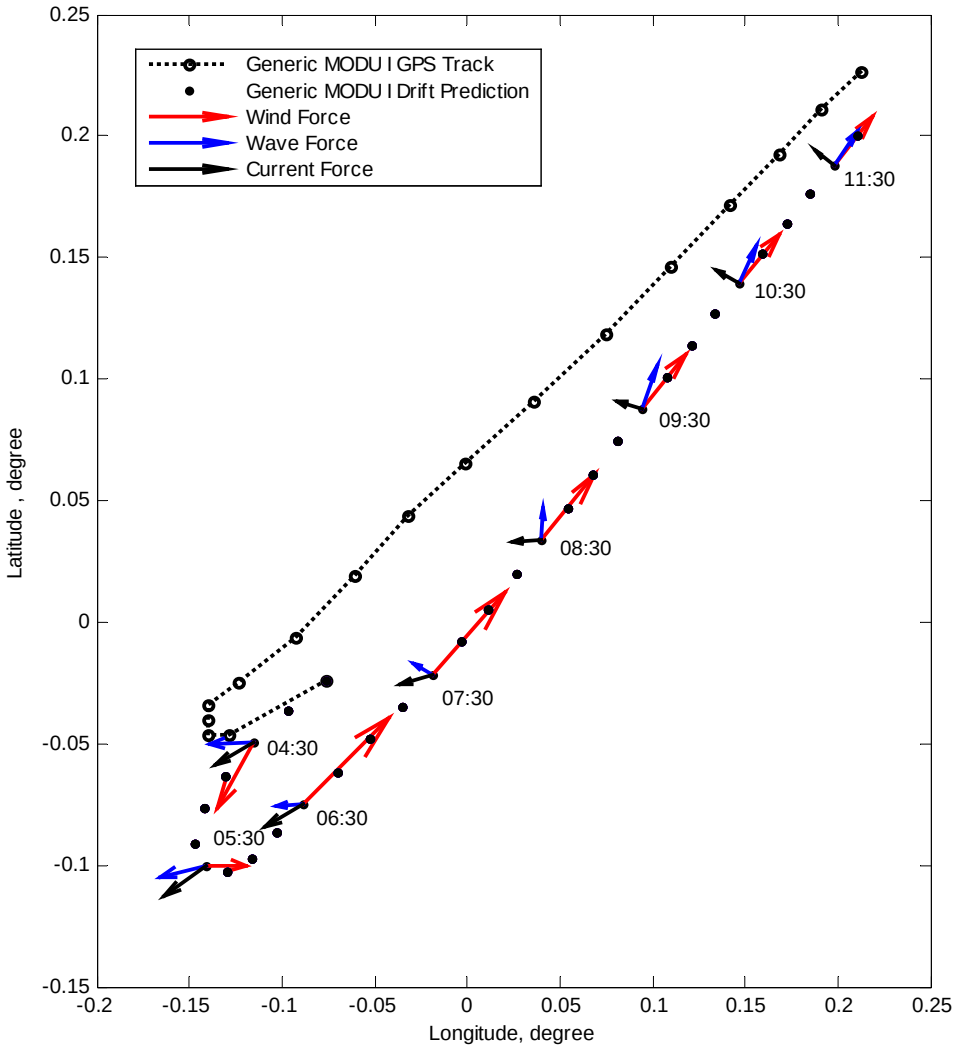

Fig. 4.11. Continued.

Examining Tables 4.5 and 4.6 and Figures 4.9 and 4.11, the following observations can be made:

● The predicted drift of MODU I is basically in the direction of the wind, which is expected because of the dominance of the wind force.

● The wind force decreased and reached its minimum around 05:30 UT when the hurricane's eye passed by, then it increased to reach its maximum around 06:30 UT. As the hurricane moved away from the MODU's position the wind force decreased.

● The direction and magnitude of the current force have similar trends as those of the wind force.

● The wave force reached its highest values from 04:00 to 06:00 UT, where the significant wave height was the greatest and then decreased as the hurricane moved to the North. However, at about 08:45, the wave force increased again. This is because of the shift of the spectral peak period towards relatively small values, where the mean wave force coefficient increases.

4.6 MODU II Drift Predictions

The position of MODU II during the hurricane was recorded by GPS every 30 minutes. The evolution of the hurricane track given in Universal Time (UT) at intervals of 3 hours and the corresponding position of MODU II are depicted in Fig.4.12. The GPS track of MODU II in UT and the closest available grid points for the hindcast multidirectional wave spectra are marked in Fig. 4.13.

Considering the position of MODU II at 06:00 UT and the corresponding location of the hurricane's eye shown in Fig.4.12, it would be expected for MODU II to drift eastward after 06:00 UT, which is confirmed by the recorded trajectory.

Similar to the simulations conducted for MODU I to explore the sensitivity of its drift to the initial yaw angle, predictions of the drift of MODU II were made using different initial yaw angles.

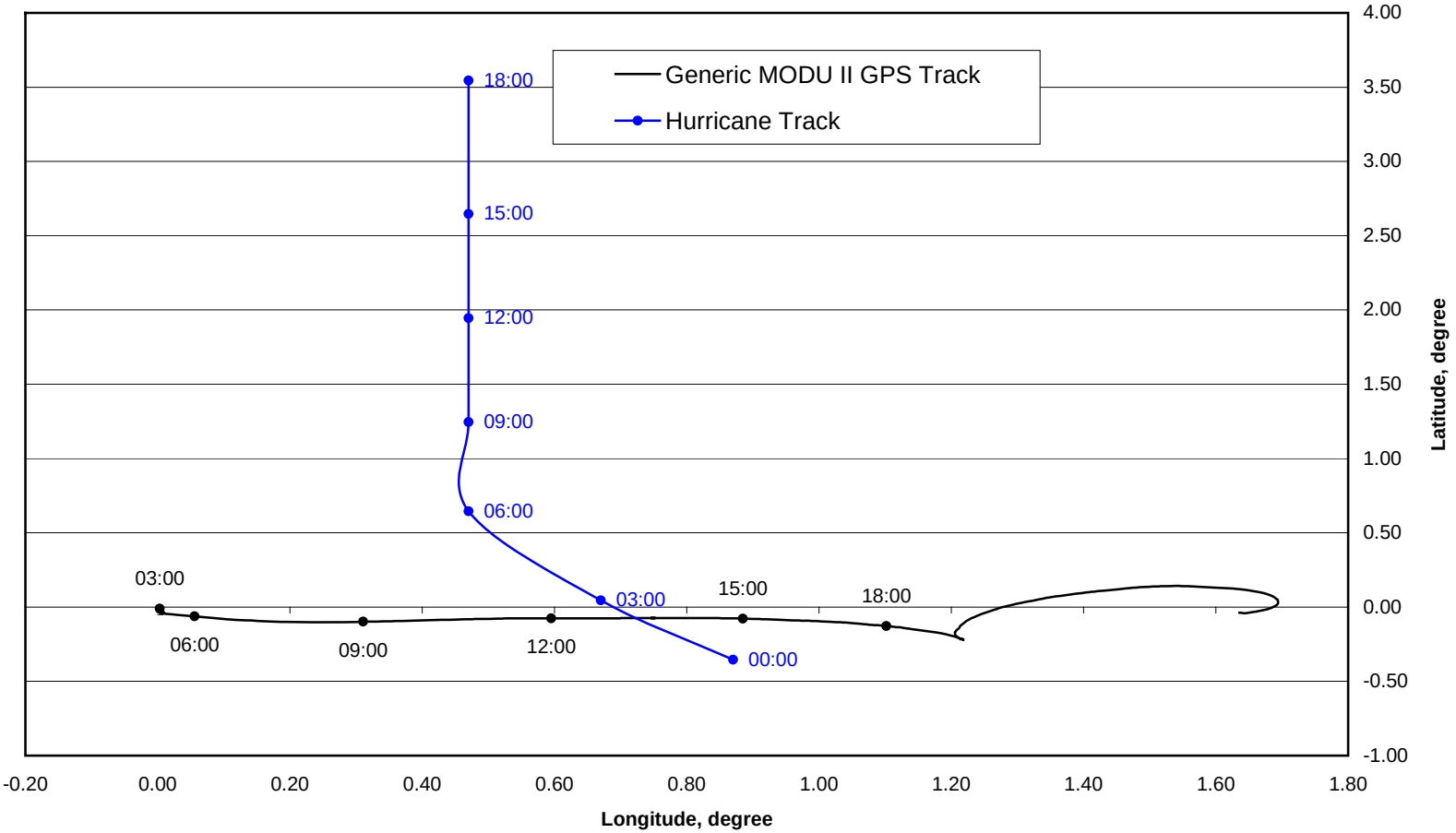

Fig.4.12. MODU II GPS and hurricane tracks.

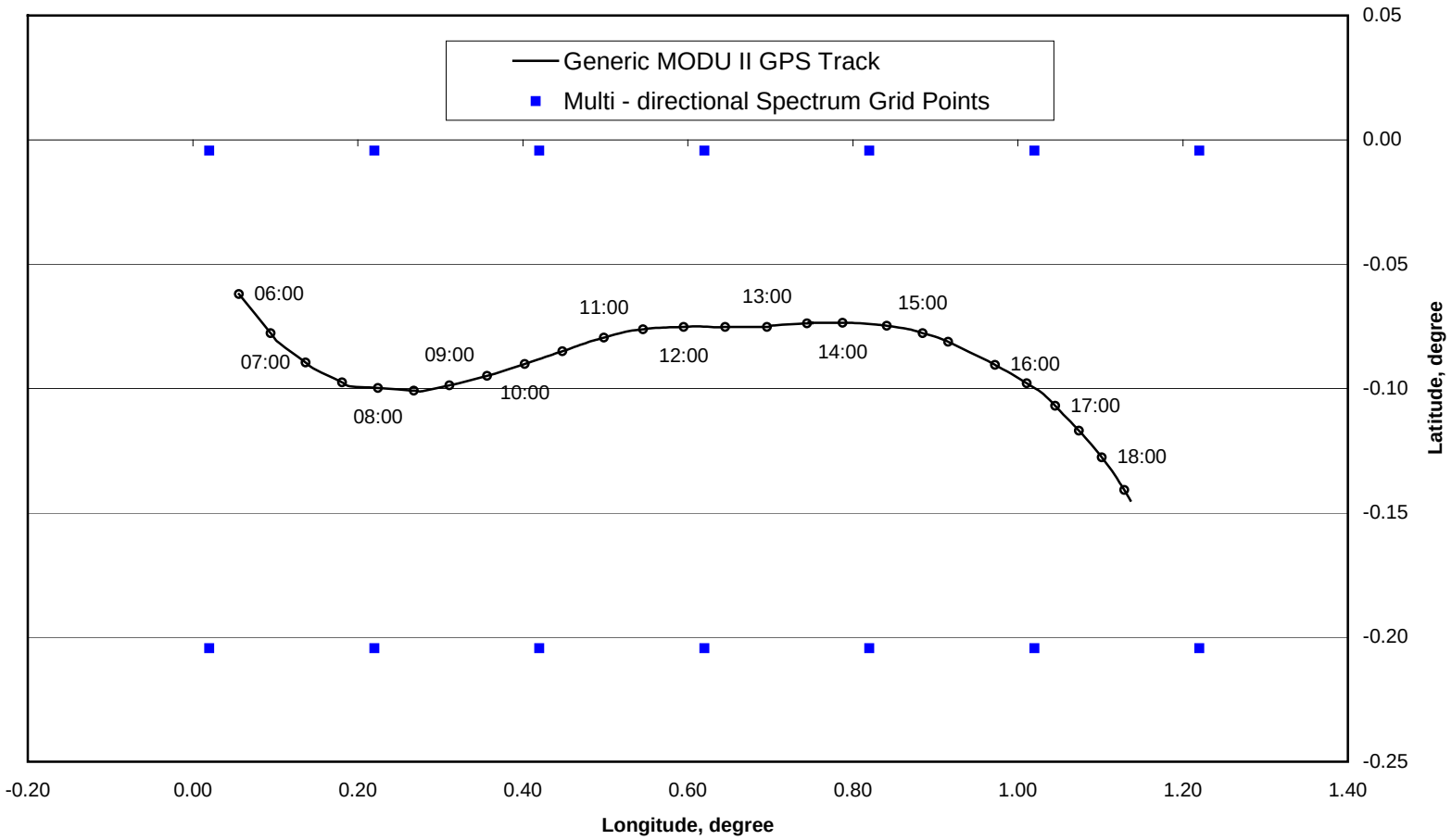

Fig.4.13. MODU II GPS track.

Given the shape of the hull of MODU II, it is expected that the initial yaw angle will have greater effect on the MODU's drift than in case of MODU I, as depicted in Fig.4.14. It is observed that the predictions of drift using the initial yaw angle, set at 0° and 45°, are virtually the same. However, the drift predicted with initial yaw angle at 90° is more toward the South, while the drift predicted with initial yaw angle at 135° is the closest to the measured trajectory of the MODU. For this reason, the initial angle of 135° was chosen for the simulation of the drift of MODU II.

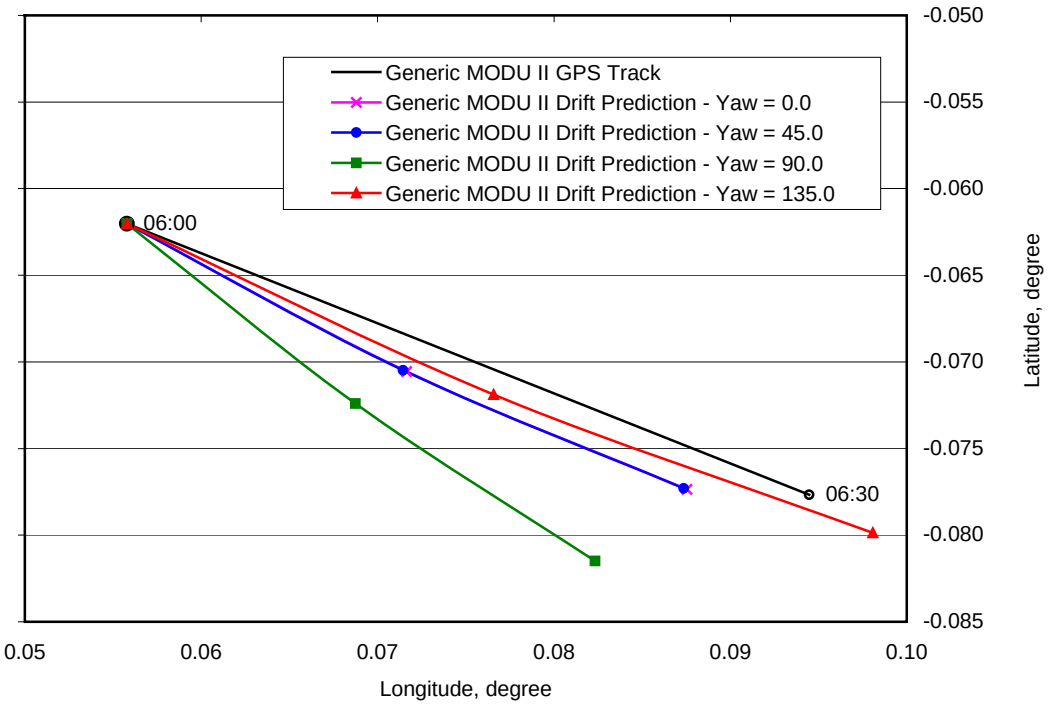

Fig.4.14. MODU II drift prediction for different yaw angles.

The simulation of the drift of MODU II from 06:00 to 10:30 UT during the hurricane with 30-minute corrections is plotted in Fig.4.15. The starting position of the simulation is chosen to be 06:00 UT, when it is assumed that MODU II began to drift significantly (see Fig.4.12). The hindcast information is updated every 15 minutes and every 30 minutes the simulation of the drift starts at the corresponding measured trajectory recorded by GPS.

The predicted drift of MODU II at the end of each 30-minute simulation is compared with the corresponding measured trajectory. This comparison shows satisfactory agreement. The distance between the measured and predicted position of the MODU at the end of each 30-minute simulation is less than 1.5 km. The predicted drift of the MODU is southward of its measured trajectory at the beginning of the simulation and gradually shifts northward, which is similar to the trend observed in the case of MODU I.

The corresponding continuous drift prediction is plotted in Fig.4.16. The predicted drift of the MODU deviates to the South of its measured trajectory from 06:00 to 08:15 UT and then to the North from 08:45 to 10:30 UT. This trend of the predicted MODU's drift is consistent with the one obtained from the prediction with 30-minute corrections. Here the distance between the measured and predicted position of the MODU computed at the end of the simulation (10:30 UT) is about 4 km.

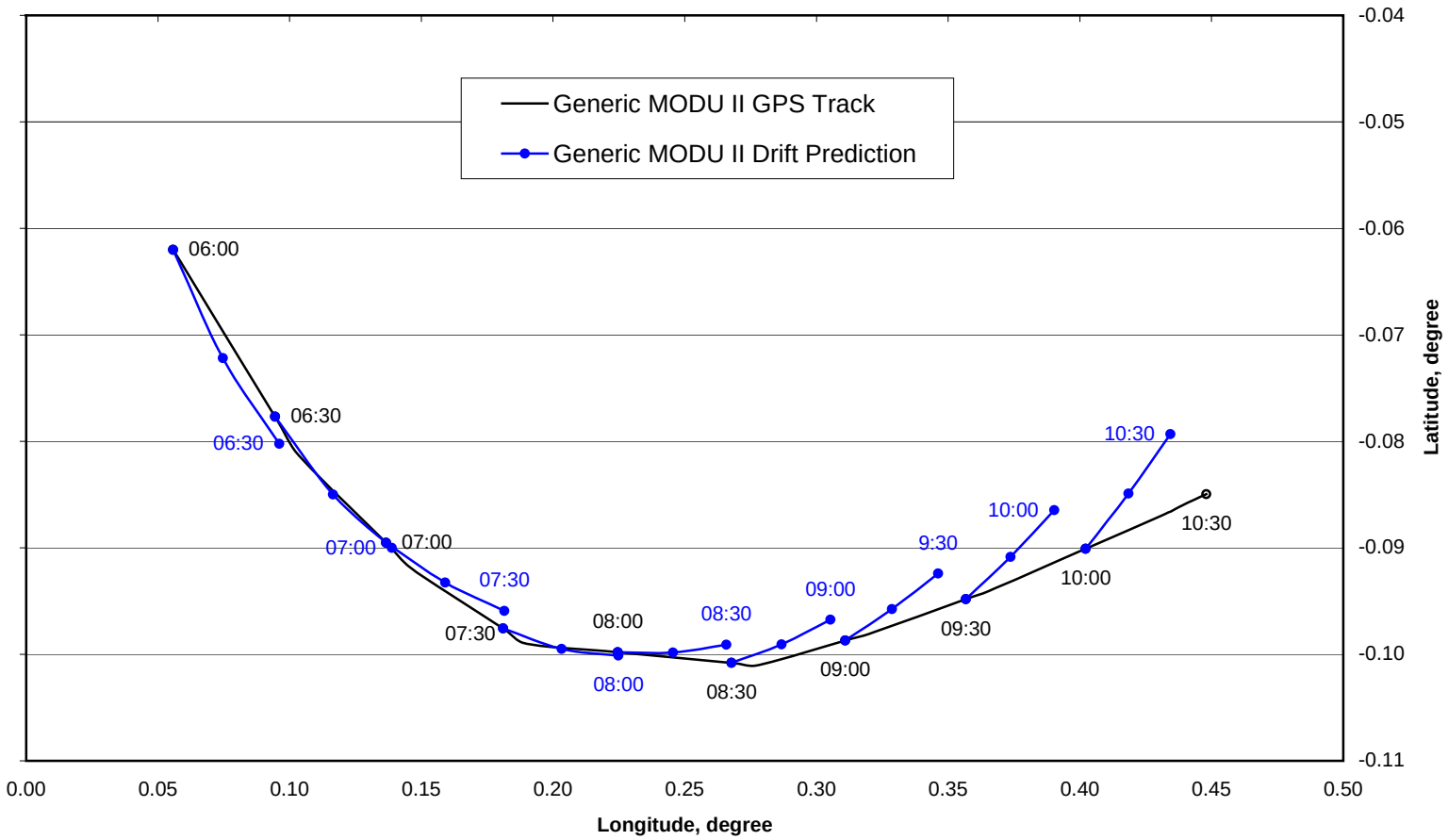

Fig.4.15. MODU II drift prediction with 30-minute corrections.

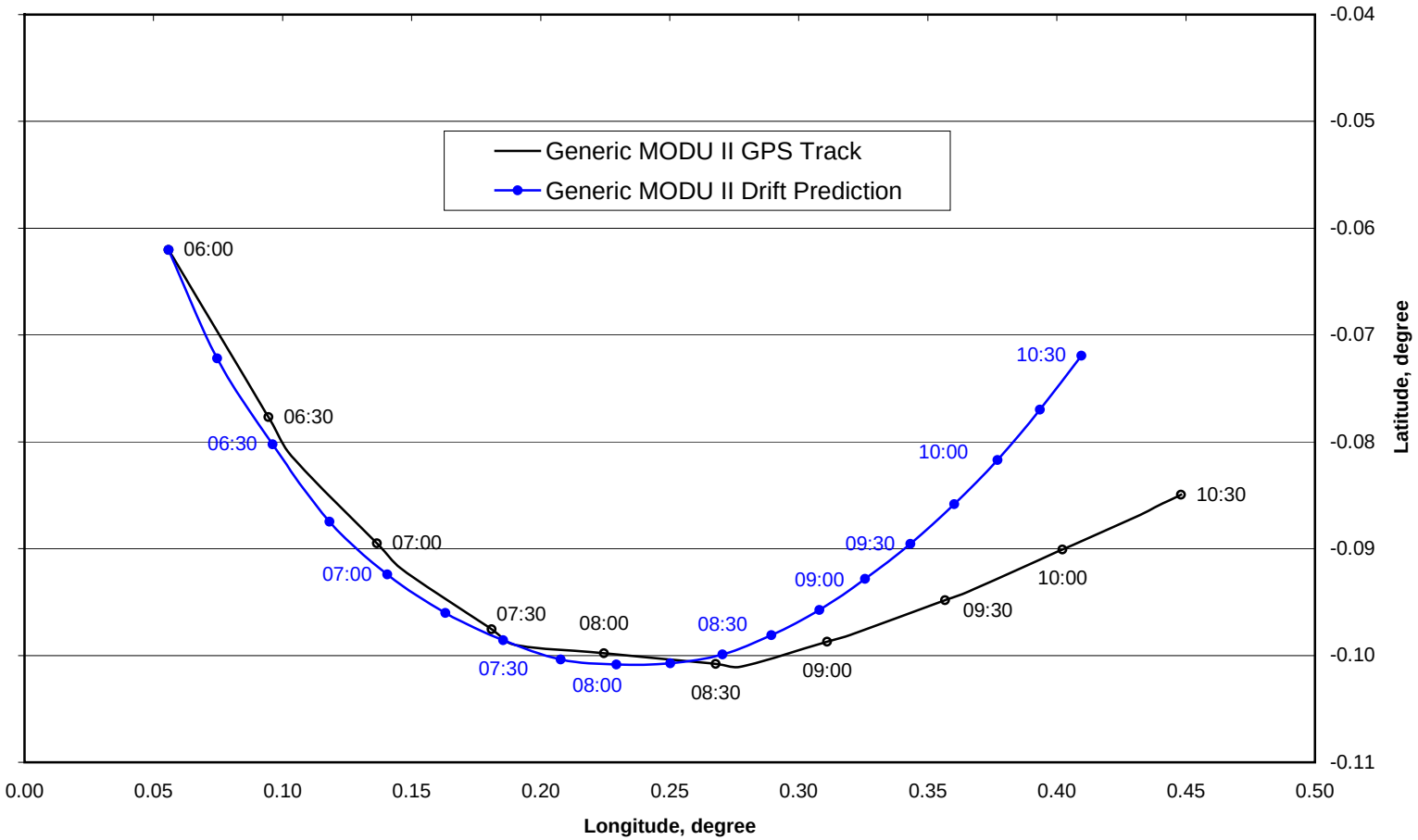

Fig.4.16. MODU II continuous drift prediction.

The magnitude and direction of the external forces applied on MODU II at the end of every 15 minutes during the continuous simulation, are summarized in Table 4.7. This table shows that the wind and wave forces dominate the MODU's drift. The mean wave force ranges from about 30% to 60% of the wind force, indicating the wave force plays a more important role than that of the case of MODU I. The greater role played by the mean wave force in the case of MODU II is expected because the hull of MODU II is much greater than that of MODU I, resulting in a greater mean wave force.

Plots of the corresponding wind, wave, and current directions for every 30 minutes are given in Fig.4.17.

Table 4.7

External forces applied on MODU II during the continuous simulation

Time	MODU Position		Wind Force		Wave Force		Current Force	
	Latitude	Longitude	Magnitude	Direction	Magnitude	Direction	Magnitude	Direction
UT	degree	degree	kips	degree	kips	degree	kips	degree
6:00	-0.062	0.056	531.89	352.76	218.18	269.56	1.64	230.37
6:15	-0.072	0.075	559.43	356.94	186.90	276.74	1.22	231.17
6:30	-0.080	0.096	547.50	0.88	216.59	283.53	1.23	231.99
6:45	-0.087	0.118	528.11	5.42	179.43	290.58	1.29	233.10
7:00	-0.092	0.141	507.44	8.39	172.08	297.10	1.40	234.45
7:15	-0.096	0.163	487.08	10.92	159.72	304.76	1.50	234.82
7:30	-0.099	0.185	470.48	12.57	147.64	309.28	1.52	233.20
7:45	-0.100	0.208	460.69	15.10	149.00	318.98	1.49	232.79
8:00	-0.101	0.229	453.37	16.66	178.93	326.17	1.37	233.12
8:15	-0.101	0.250	443.23	18.47	202.15	335.01	1.29	233.31
8:30	-0.100	0.270	435.42	19.90	186.96	342.63	1.13	233.87
8:45	-0.098	0.289	430.58	21.02	192.46	347.98	0.94	233.52
9:00	-0.096	0.308	426.19	22.03	184.45	354.12	0.80	232.02
9:15	-0.093	0.326	426.86	22.75	187.28	357.54	0.72	230.32
9:30	-0.090	0.343	428.04	23.62	181.91	2.15	0.70	230.68
9:45	-0.086	0.360	428.40	24.85	179.73	4.22	0.70	231.37
10:00	-0.082	0.377	430.86	26.43	182.64	8.59	0.73	229.66
10:15	-0.077	0.393	424.20	27.77	175.73	9.67	0.81	227.17

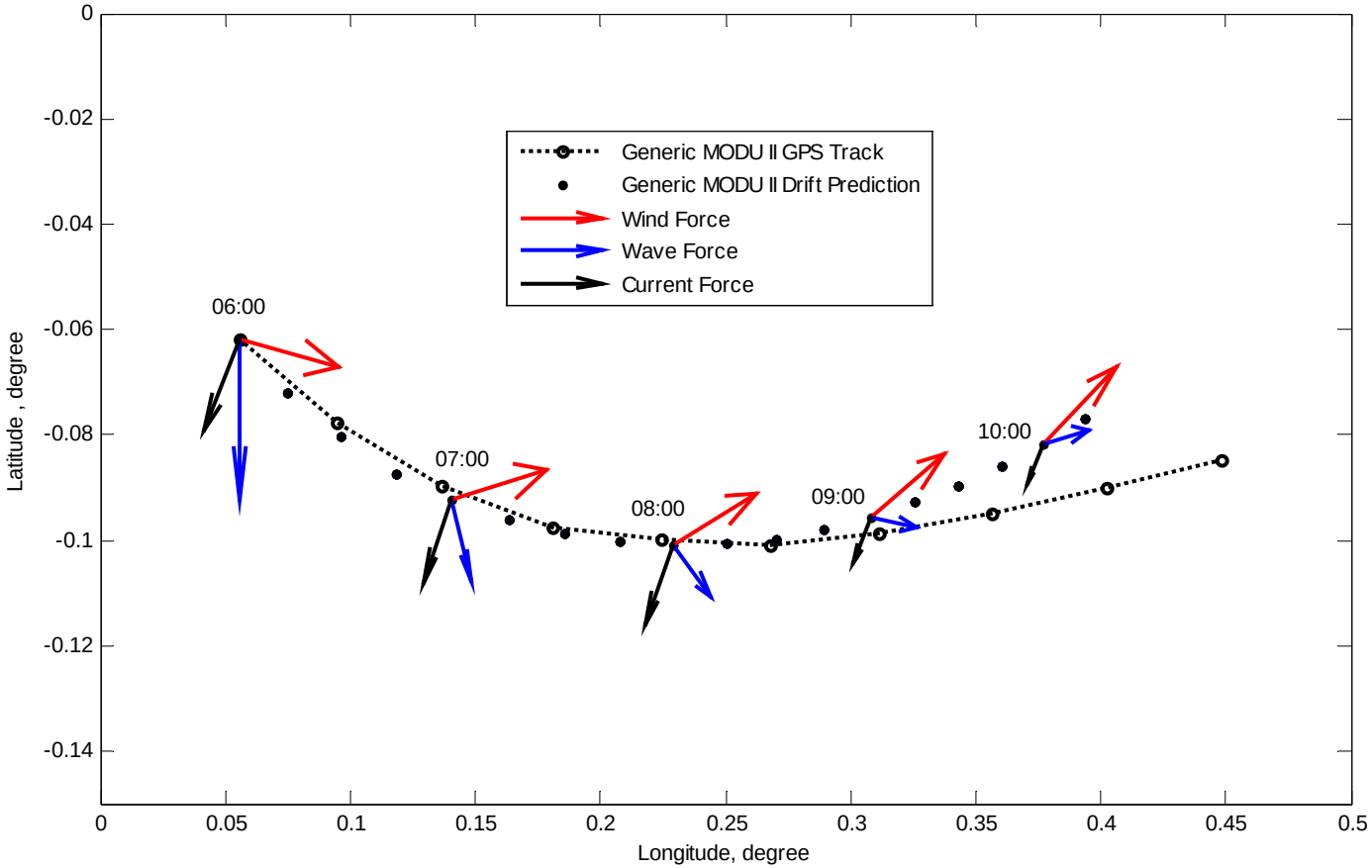

Fig. 4.17. External forces applied on MODU II during the continuous simulation.

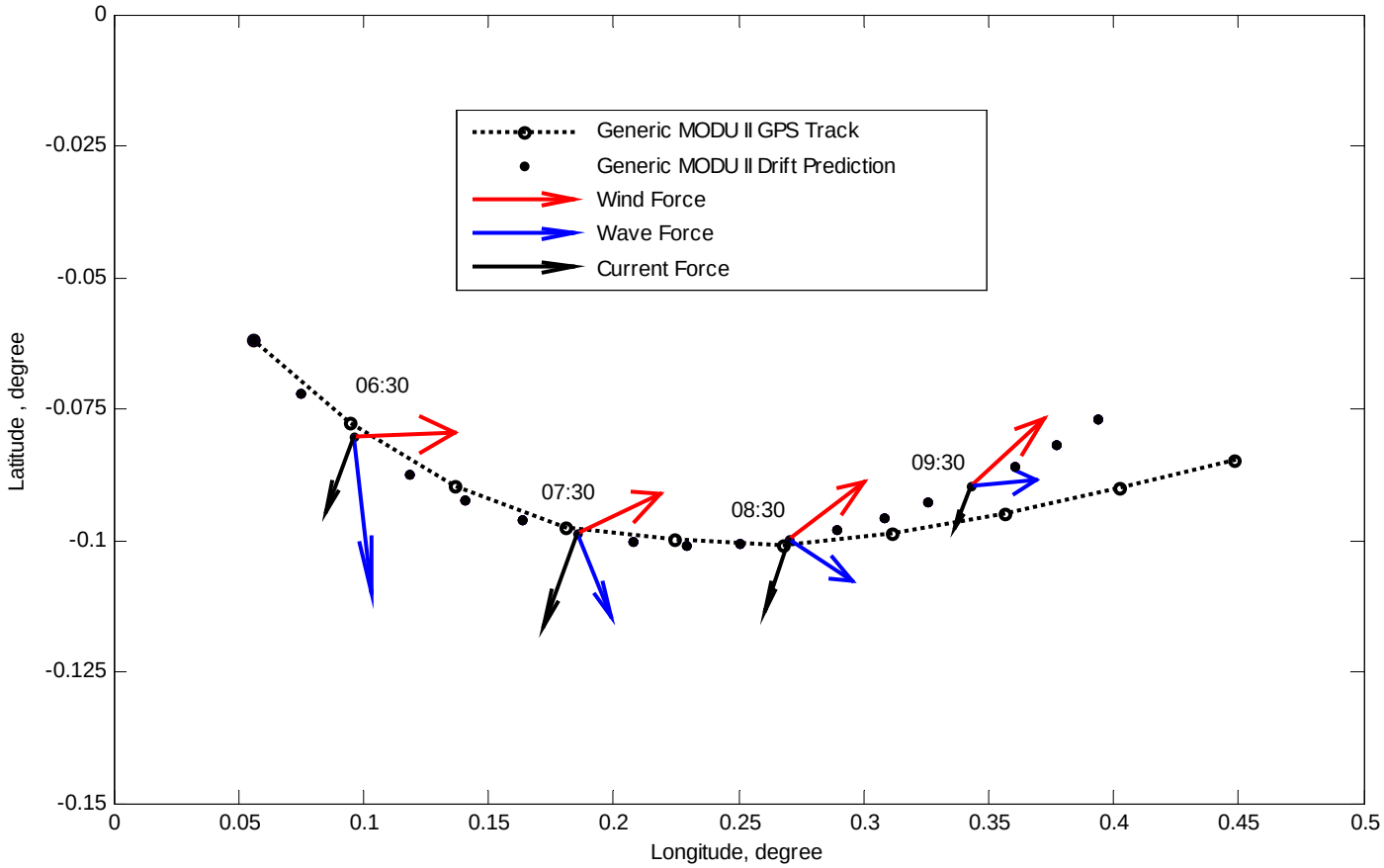

Fig. 4.17. Continued.

Examining Table 4.7 and Figure 4.17, the following observations can be made:

- The predicted drift of MODU II is consistent with the magnitude and direction of the wind and wave forces with no significant effects due to the current forces.
- The wind force decreased as the hurricane moved away from the MODU's position.
- The current force also decreased as the hurricane moved away from the MODU's position maintaining a nearly constant direction throughout the simulation.
- The wave force has its highest values at 06:00 UT with no significant change in its magnitude throughout the simulation.

5. CONCLUSIONS

The numerical program “DRIFT” was developed and used for predicting the trajectory of two typical semi-submersible MODUs, namely ”Generic MODU I” and ”Generic MODU II”, during hurricane Katrina, given the hindcast met-ocean conditions (wind, current, and wave) and the characteristics of the MODUs. Two sets of hindcast data called, “Emergency Response Data” (ERD) and “Revised Data” (RD) were sequentially provided by our industry partners for this study but only the results of the predicted drift based on ERD are presented in this thesis.

Under the impact of severe wind, currents, and waves, the mooring system of a MODU may lose its position holding capability allowing the MODU to drift. To explore the feasibility and accuracy of predicting the trajectory of a drifting MODU given hindcast or real-time met-ocean conditions and limited knowledge of the condition of the drifting MODU, this study employed a simplified governing equation describing only the horizontal (surge, sway, and yaw) motions of a MODU experiencing steady wind, current, and wave forces. The simplified hydrodynamic model neglects the first- and second-order oscillatory wave forces, unsteady wind forces (owing to wind gustiness), wave drift damping, and the effects of the body oscillation on the steady wind and current forces. It was assumed that the net effects of the oscillatory forces on the steady motion are insignificant. To verify the accuracy and feasibility of this simplified approach, the predicted drifts of two MODUs were compared with the corresponding measured trajectories recorded by the Global Positioning System (GPS).

A satisfactory agreement was observed between the recorded trajectories of MODU I and II and the corresponding predictions based on the ERD. The distance between the predicted and measured position was less than 2.5 km for MODU I after five and a half-hours of drift and 4.0 km for MODU II after four and a half-hours of drift. However, it was noticed that the hindcast current velocity in the ERD was a depth averaged storm

driven current velocity, which greatly underestimates the current velocity near the free surface.

Based on this study, the following conclusions are derived:

1. The numerical program, “DRIFT”, based on a relatively simplified hydrodynamic model, is capable of predicting the trajectory of a drifting MODU.
2. However accurate prediction depends on the accuracy of the input met-ocean conditions (wind, wave, and current data) and the accurate and complete description of the condition of the MODU and its damaged mooring system. If the input met-ocean conditions are inaccurate or the descriptions of the condition of the drift MODU are incomplete, the prediction will be inaccurate or even qualitatively different from the corresponding measurement.
3. At present stage, real-time met-ocean conditions during a hurricane can be predicted with certain accuracy or uncertainty. Considering this factor, the simplified hydrodynamic model used in this study seems to be adequate.
4. Directions, spreading and the energy of wave components at relatively high frequency ranges are crucial, especially at late stages of a hurricane when the wind force is no longer dominant.

However, it should be noted that the above conclusions are derived based on the comparison of the simulations with the recorded trajectories of two drifting MODUs during hurricane Katrina. More studies are required for the drifting of different MODUs in different hurricanes before drawing the final conclusion that we have the capability of predicting the trajectory of a MODU, which completely or partially loses its positioning capability during hurricanes.

REFERENCES

Anderson, E., Odulo, A., Spaudling, M., 1998. Modeling of Leeway Drift. U.S. Coast Guard Research and Development Center, Report No. CG-D-06-99. http://www.rdc.uscg.gov/reports/1999/CGD0699Report.pdf

American Petroleum Institute (API), 1993. Recommended practice for planning, designing and constructing fixed offshore platforms-working stress design. API RP2A-WSD, 20th edition, American Petroleum Institute, Dallas, TX.

Argyris, J., Mlejnek, H.P., 1991. Dynamic of Structures. Elsevier Science Publication Co., New York.

Chen, X., 2002. Floating structures and their mooring/tendon systems. Ph.D. Dissertation, Ocean Engineering Program, Civil Engineering Department, Texas A&M University, College Station.

Chitrapu, A.S., Ertekin, R.C., 1995. Time-domain simulation of large-amplitude response of floating platforms. Ocean Engineering 22(4), 367-385.

Chopra, A.K., 2001. Dynamics of Structures: Theory and Applications to Earthquake Engineering. Prentice Hall, Upper Saddle River, New Jersey.

de Boom, W.C., Pinkster, J.A. and Tan, S.G., 1983. Motion and tether force prediction for a deepwater tension leg platform. Proceedings of the Offshore Technology Conference, Houston, OTC4487, 377-388.

Faltinsen, O.M., 1990. Sea Loads on Ships and Offshore Structures. Cambridge University Press, New York.

Goda, Y., 1979. A review on statistical interpretation of wave data. Report of the Port and Harbour Research Institute, 18, 5-32.

Grue, J., 1999. A note on the contributions to the wave-drift damping matrix from the time-averaged second order potential. Applied Ocean Research 21(1), 47-50.

Hodgins, D.O., Mak R.Y., 1995. Leeway Dynamic Study Phase I: Development and Verification of a Mathematical Drift Model for Four-person Liferafts. Transportation Development Center, Transport Canada, Report No. TP 12309E.

http://www.tc.gc.ca/tdc/publication/pdf/12300/12309e.pdf

Lee, C.H., 1995. WAMIT Theory Manual. Report No. 95-2, Massachusetts Institute of Technology, Cambridge.

Ma, W., Lee, M.Y., Zou, J., Huang, E.W., 2000. Deepwater nonlinear coupled analysis tool. Proceedings of the Offshore Technology Conference, Houston, OTC12085 [CD-ROM].

McGovern, A., 2004. Geographic Distance and Azimuth Calculations. http://www.codeguru.com/Cpp/Cpp/algorithms/article.php/c5115

Newman, J.N., 1999. Marine Hydrodinamics. Massachusetts Institute of Technology, Cambridge.

Nielsen, F.G., Herfjord, K., Hunstad, G. Olsen, G., 1994. Dynamic characteristics of a large catenary moored production platform. Proceedings of BOSS'94 Behavior of Offshore Structures, Massachusetts Institute of Technology, Cambridge, Massachusetts, 2, 113-131.

Oceanweather Inc., 2006. Hindcast Data on Winds, Waves, and Currents in Northern Gulf of Mexico in Hurricanes Katrina and Rita, Cos Cob, Connecticut. http://www.mms.gov/tarprojects/580/580AA.pdf

Ormberg, H., Larsen, K., 1997. Coupled analysis of floating motion and mooring dynamics for a turret moored tanker. Proceedings of BOSS'97 Behaviour of Offshore Structures, Delft, The Netherlands, 2, 469-483.

Paulling, J.R., Webster, W.C., 1986. A consistent large-amplitude analysis of the coupled response of a TLP and tendon system. Proceedings of Offshore Mechanics and Arctic Engineering (OMAE), Tokyo, Japan, 3, 126-133.

Ran, Z. Kim, M.H., 1997. Nonlinear coupled responses of a tethered spar platform in waves. International Journal of Offshore and Polar Engineering 7(2), 111-118.

Sharples, M., 2004. Post Mortem Failure Assessment of MODUs During Hurricane Ivan. http://www.mms.gov/tarprojects/548/Ivan_FinalReport.pdf

Smith, E., 2006. Recovery and Rebuilding Following Hurricanes Katrina and Rita. http://onlinepubs.trb.org/webmedia/2006am/553Smith.pdf

Su, T.C., 1986. On Predicting the Boat's Drift for Search and Rescue. U.S. Department of Transportation, Report No. DOT/OST/P-34/87/059.

Visual Numerics Inc., 1999. IMSL Fortran Library User's Guide Math/Library. http://www.vni.com/documentation/TechSpecs/fortrants/FortranTSV2.pdf

WAMIT, Inc., 1999. WAMIT User Manual Versions 5.4, 5.4PC, 5.3S. Massachusetts Institute of Technology, Cambridge.

Wilson, J.F. 2003. Dynamics of Offshore Structures. John Wiley & Sons Inc., Hoboken, New Jersey.

Wood, W.L., 1990. Practical Time-stepping Schemes. Clarendon Press, Oxford, United Kingdom.

Zimmerman, E., 2006. Private Communication.

Zwillinger, D., 1995. Spherical Geometry and Trigonometry. CRC Press, Boca Raton, Florida.

APPENDIX A-1

GREAT CIRCLE FORMULA

Assuming a spherical model, i.e., that the Earth is a sphere with mean radius $R = 6371.0$ km, and using the spherical law of cosines (Zwillinger, 1995), a formula for the distance between two points given their latitude and longitude coordinates is derived (McGovern, 2004). The spherical triangle shown in Fig.A-1.1 with sides **a**, **b**, and **c** and angles α, ϕ ,and γ is defined by two end points with coordinates (φ_1, λ_1) and (φ_2, λ_2), respectively and the North Pole. The spherical law of cosines applied to side **b** is given by the formula:

$$\cos(\mathbf{b}) = \cos(\mathbf{a})\cos(\mathbf{c}) + \sin(\mathbf{a})\sin(\mathbf{c})\cos(\phi) \tag{A-1.1}$$

The angular length of side b is given by:

$$\mathbf{b} = \arccos\left[\cos(\mathbf{a})\cos(\mathbf{c}) + \sin(\mathbf{a})\sin(\mathbf{c})\cos(\phi)\right] \tag{A-1.2}$$

The arc length between the two end points is given by:

$$\text{arc length} = R\arccos\left[\cos(\mathbf{a})\cos(\mathbf{c}) + \sin(\mathbf{a})\sin(\mathbf{c})\cos(\phi)\right] \tag{A-1.3}$$

where

$$\phi = (\lambda_2 - \lambda_1)\frac{\pi}{180} \tag{A-1.4}$$

$$\mathbf{c} = (90^\circ - \varphi_1)\frac{\pi}{180} \tag{A-1.5}$$

$$\mathbf{a} = \left(90^\circ - \varphi_2\right)\frac{\pi}{180} \qquad \text{(A-1.6)}$$

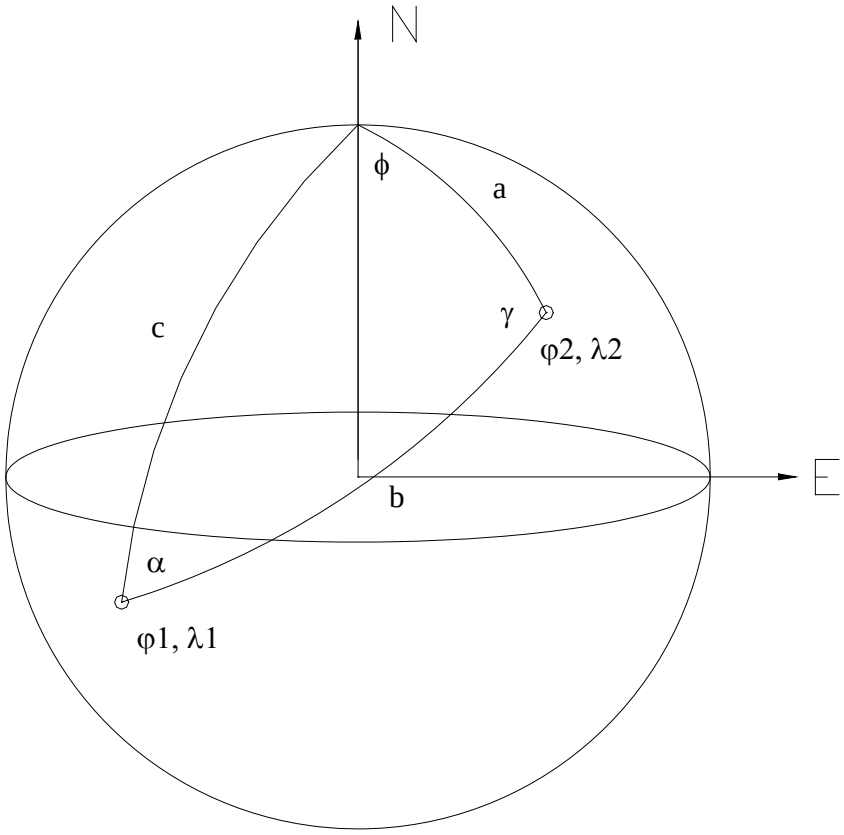

Fig.A-1.1. Spherical triangle.

The angle made between true north and the great circle passing through the two points at the first point, i.e. the azimuth α, can be found by using the law of sines (Zwillinger, 1995):

$$\frac{\sin(\alpha)}{\sin(\mathbf{a})} = \frac{\sin(\phi)}{\sin(\mathbf{b})} = \frac{\sin(\gamma)}{\sin(\mathbf{c})} \tag{A-1.7}$$

$$\sin(\alpha) = \frac{\sin(\mathbf{a})\sin(\phi)}{\sin(\mathbf{b})} \;\Rightarrow\; \alpha = \arcsin\left[\frac{\sin(\mathbf{a})\sin(\phi)}{\sin(\mathbf{b})}\right] \tag{A-1.8}$$

Given initial latitude and longitude coordinates (φ_1, λ_1), distance (arc length), and azimuth (α) the latitude and longitude coordinates (φ_2, λ_2) of the end point can be found using the spherical law of cosines for side **a**.

$$\cos(\mathbf{a}) = \cos(\mathbf{b})\cos(\mathbf{c}) + \sin(\mathbf{c})\sin(\mathbf{b})\cos(\alpha) \tag{A-1.9}$$

$$\mathbf{a} = \arccos\left[\cos(\mathbf{b})\cos(\mathbf{c}) + \sin(\mathbf{c})\sin(\mathbf{b})\cos(\alpha)\right] \tag{A-1.10}$$

$$\mathbf{b} = \text{arc length} / \text{R} \tag{A-1.11}$$

Using formula (A-2.6):

$$\sin(\phi) = \frac{\sin(\alpha)\sin(\mathbf{b})}{\sin(\mathbf{a})} \;\Rightarrow\; \phi = \arcsin\left[\frac{\sin(\alpha)\sin(\mathbf{b})}{\sin(\mathbf{a})}\right] \tag{A-1.12}$$

Then the latitude and longitude coordinates (φ_2, λ_2) are found by:

$$\varphi_2 = 90^\circ - \frac{180}{\pi}\mathbf{a} \tag{A-1.13}$$

$$\lambda_2 = \frac{180}{\pi}\phi + \lambda_1 \tag{A-1.14}$$

APPENDIX A-2

VISCOUS YAW DAMPING MOMENT

The drag force on a cylindrical element with length (dx) (See Fig.A-2.1) is given by:

$$dF = 0.5\rho C_d D_E V_y^2 dx \qquad \text{(A-2.1)}$$

where ρ is the water density, C_d the drag coefficient, and D_E the equivalent diameter.

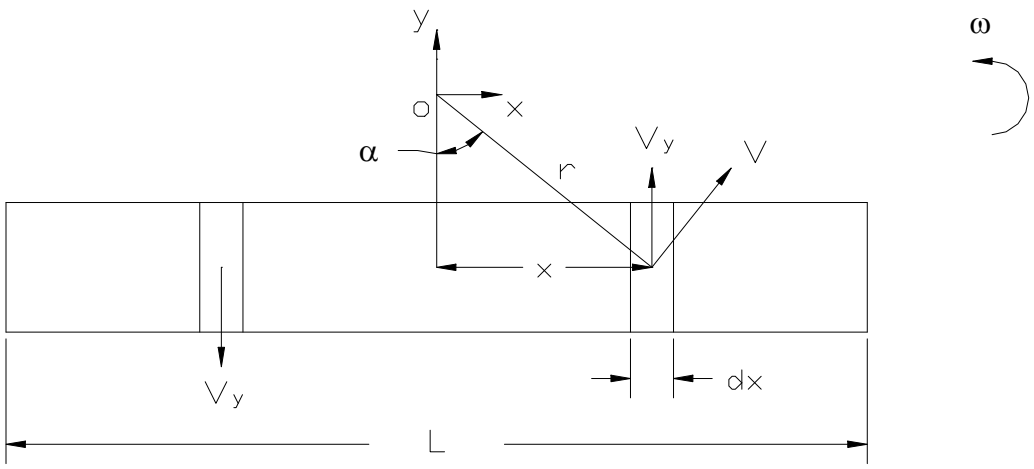

Fig.A-2.1. Drag force on a cylindrical element.

The yaw moment with respect to the center of gravity (CG), point o, is given by:

$$dM = 0.5\rho C_d D_E V_y^2 x dx \qquad \text{(A-2.2)}$$

The body velocity V, may be written in terms of the angular velocity ($\omega = d\theta / dt$) by:

$$V = r\omega = r\dot{\theta} \tag{A-2.3}$$

where θ is the yaw angle. Then form Fig.A-2.1 for V_y we have:

$$V_y = V \sin\alpha = r \sin\alpha\dot{\theta} = x\dot{\theta} \tag{A-2.4}$$

Substituting equation (A-2.4) into equation (A-2.2) and integrating over the length of the cylinder L, the viscous yaw moment caused by the yaw rotation of the body is:

$$M = \rho C_d D_E \frac{L^4}{16}\dot{\theta}^2 \tag{A-2.5}$$

The diameter of the equivalent cylinder, D_E can be found by equating the volumes of the structural element (pontoon or column) ∇ and the equivalent cylinder ∇_{EC}:

$$\nabla = \nabla_{EC} = \frac{\pi D_E^2}{4} L \ , \ D_E = \sqrt{\frac{4\nabla}{\pi L}} \tag{A-2.6}$$

It should be noted that the viscous yaw damping moment is in direction opposite to the body rotation.

APPENDIX A-3

MODU WAVE FORCE COEFFICIENTS

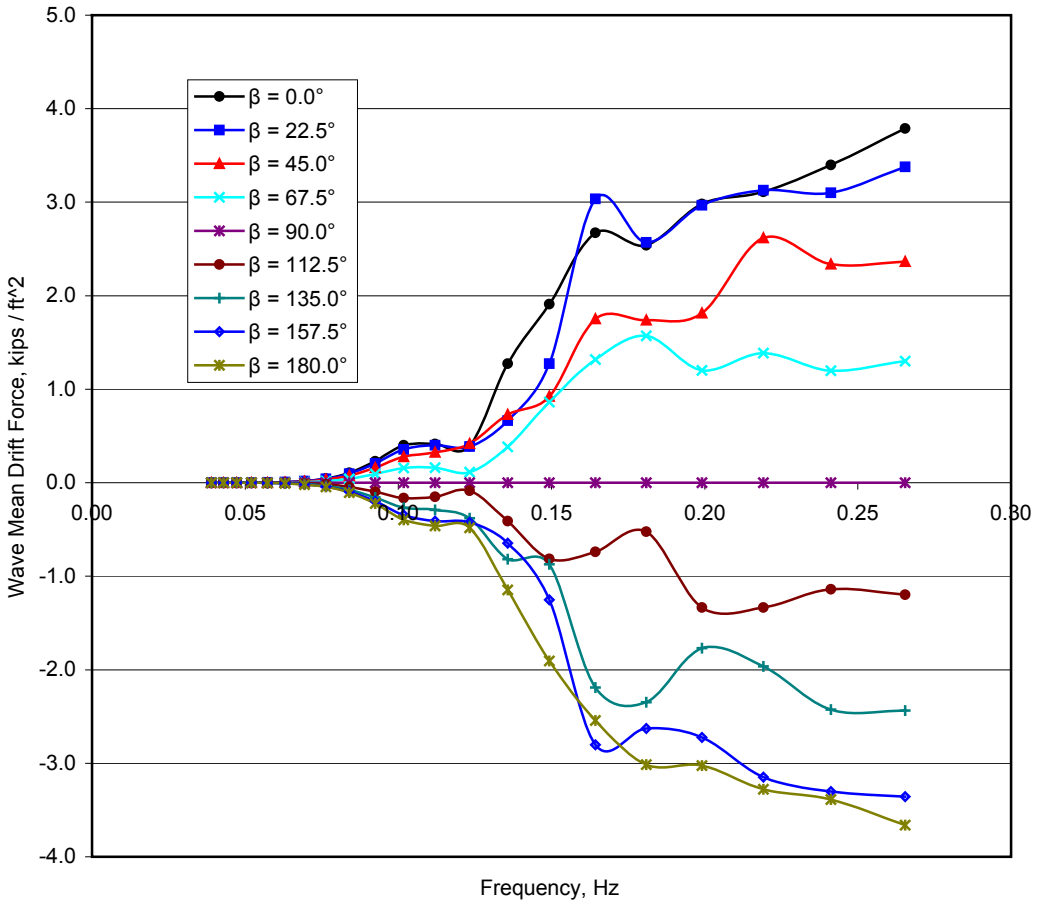

Fig.A-3.1. MODU I surge wave mean drift force coefficients.

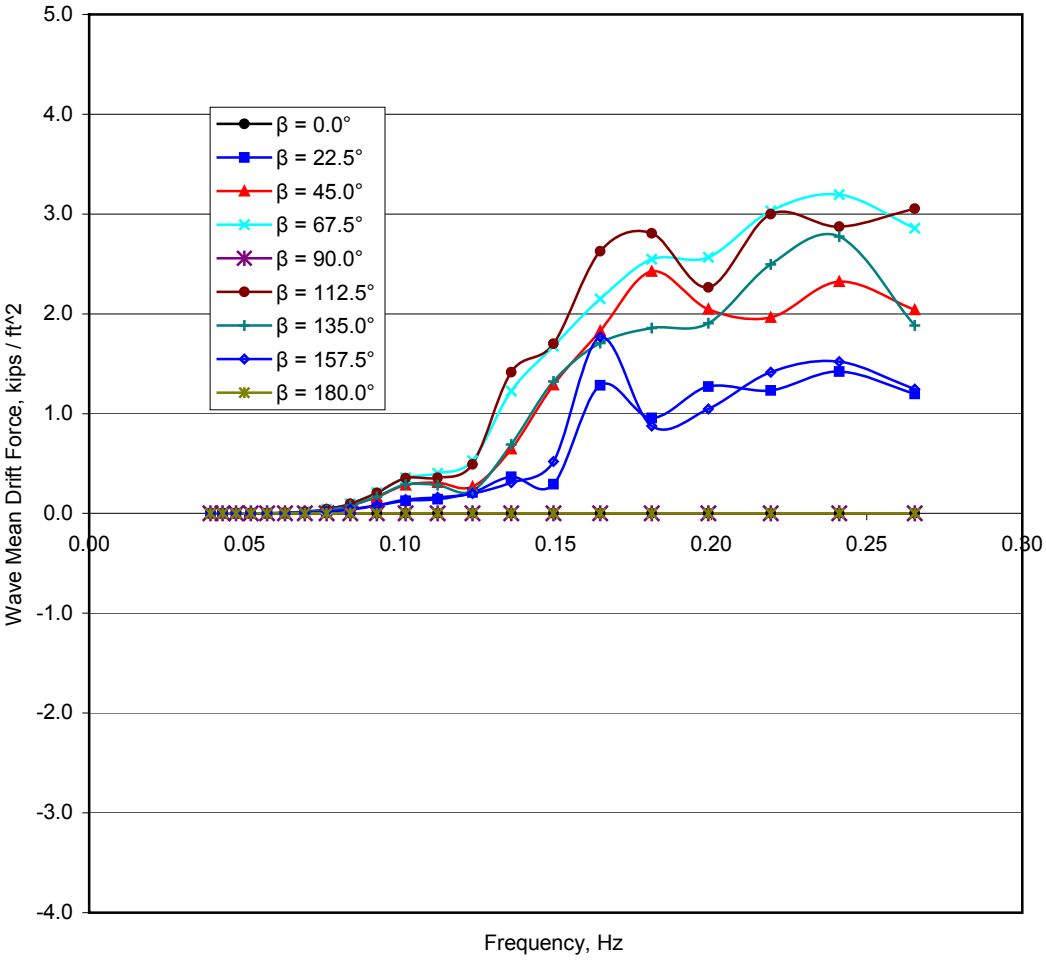

Fig.A-3.2. MODU I sway wave mean drift force coefficients.

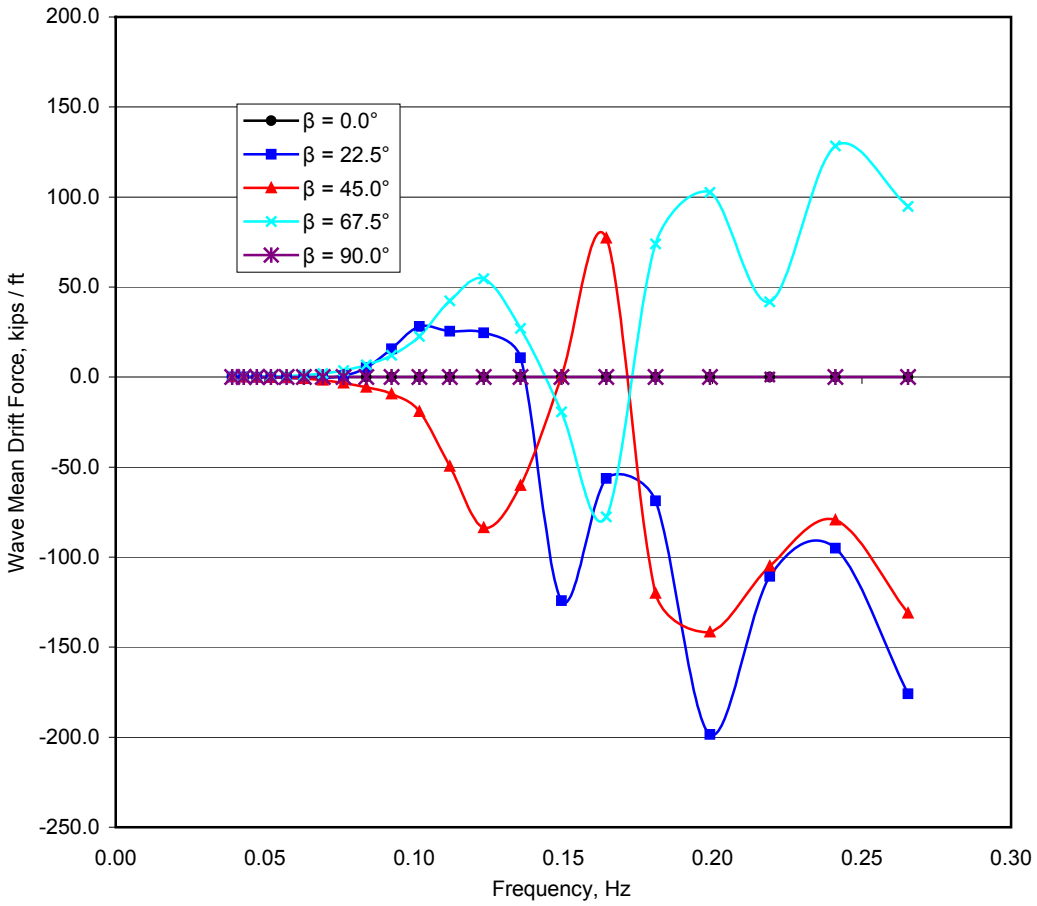

Fig.A-3.3. MODU I yaw wave mean drift force coefficients, $\beta = 0° \div 90°$.

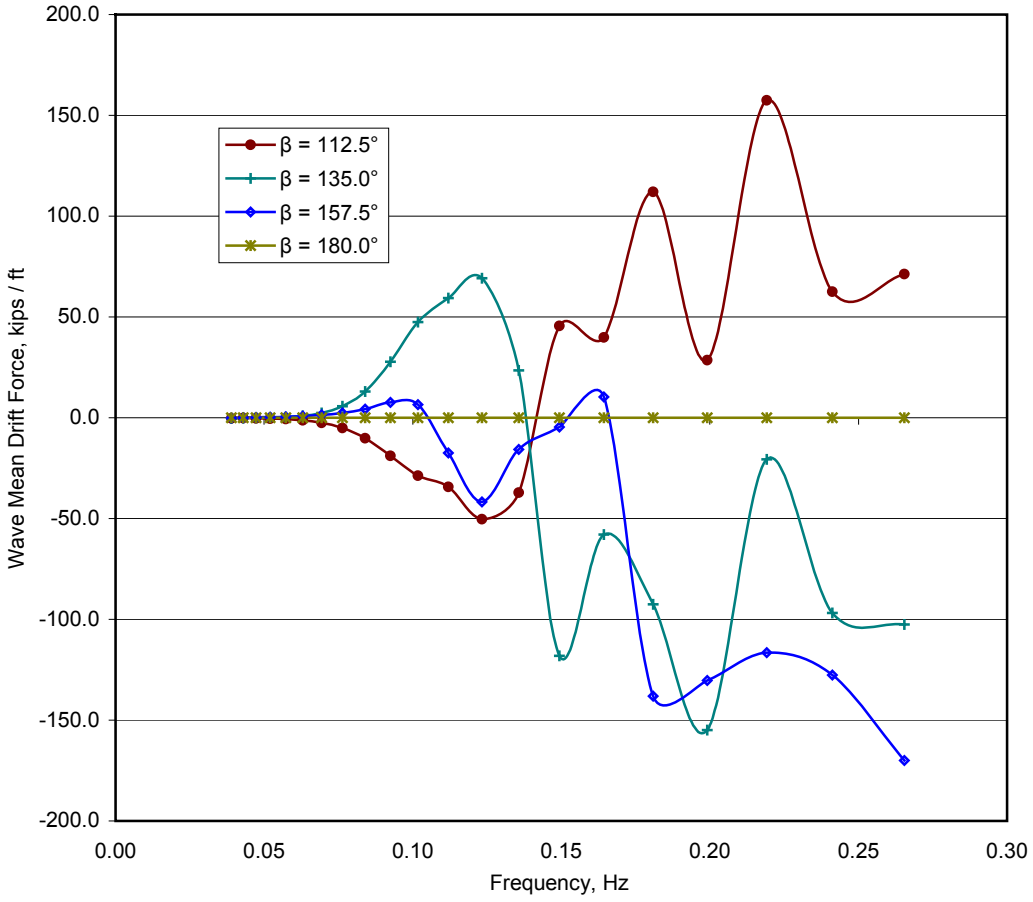

Fig.A-3.4. MODU I yaw wave mean drift force coefficients, $\beta = 112.5° \div 180°$.

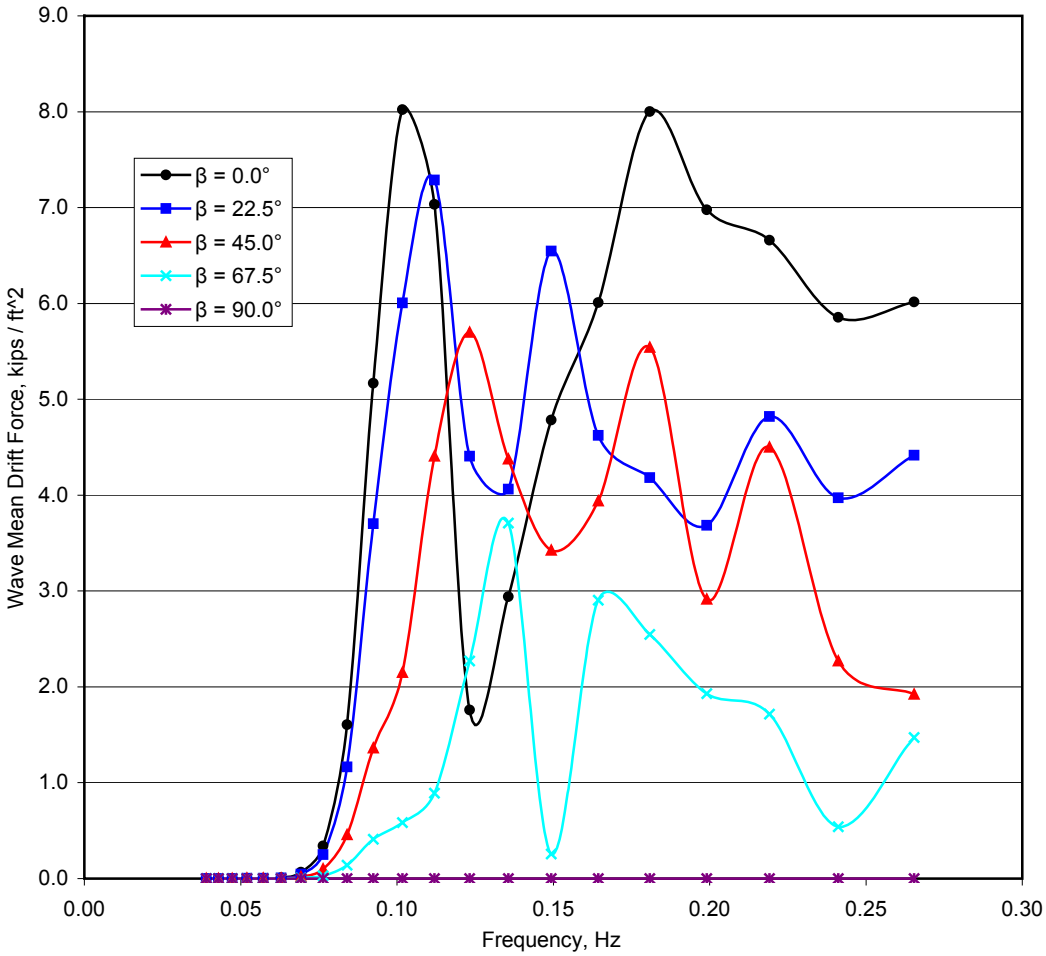

Fig.A-3.5. MODU II surge wave mean drift force coefficients.

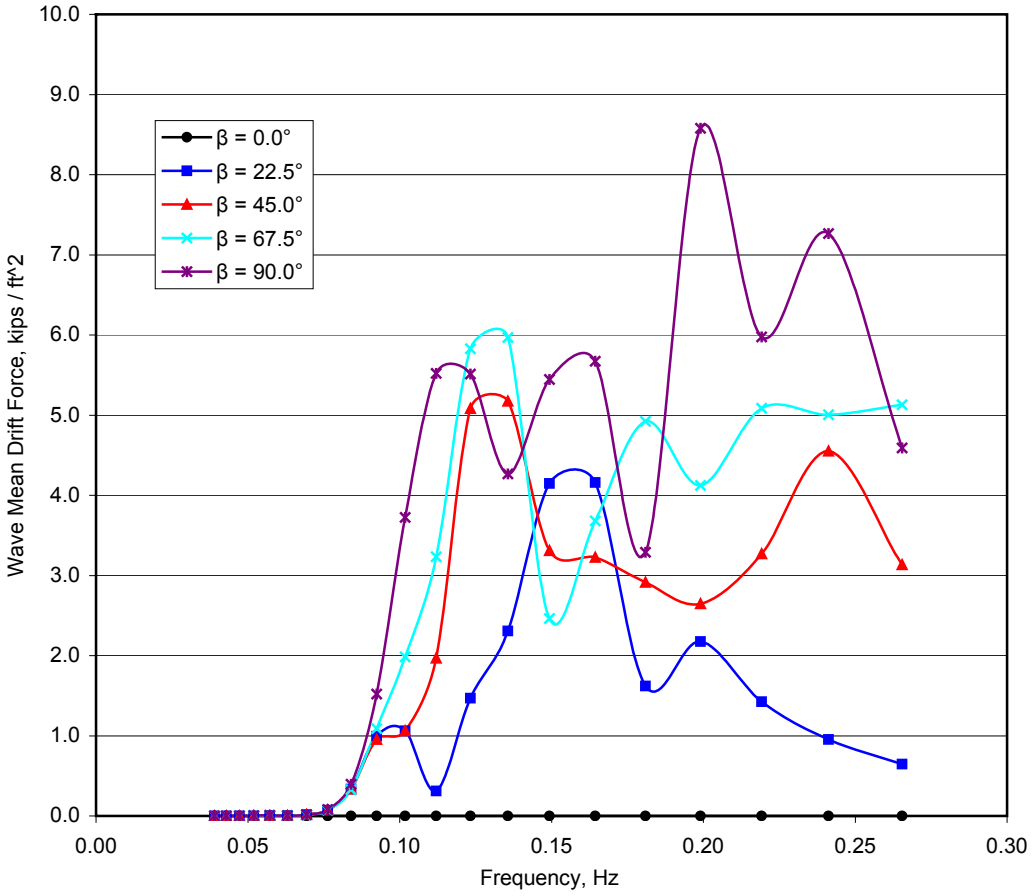

Fig.A-3.6. MODU II sway wave mean drift force coefficients.

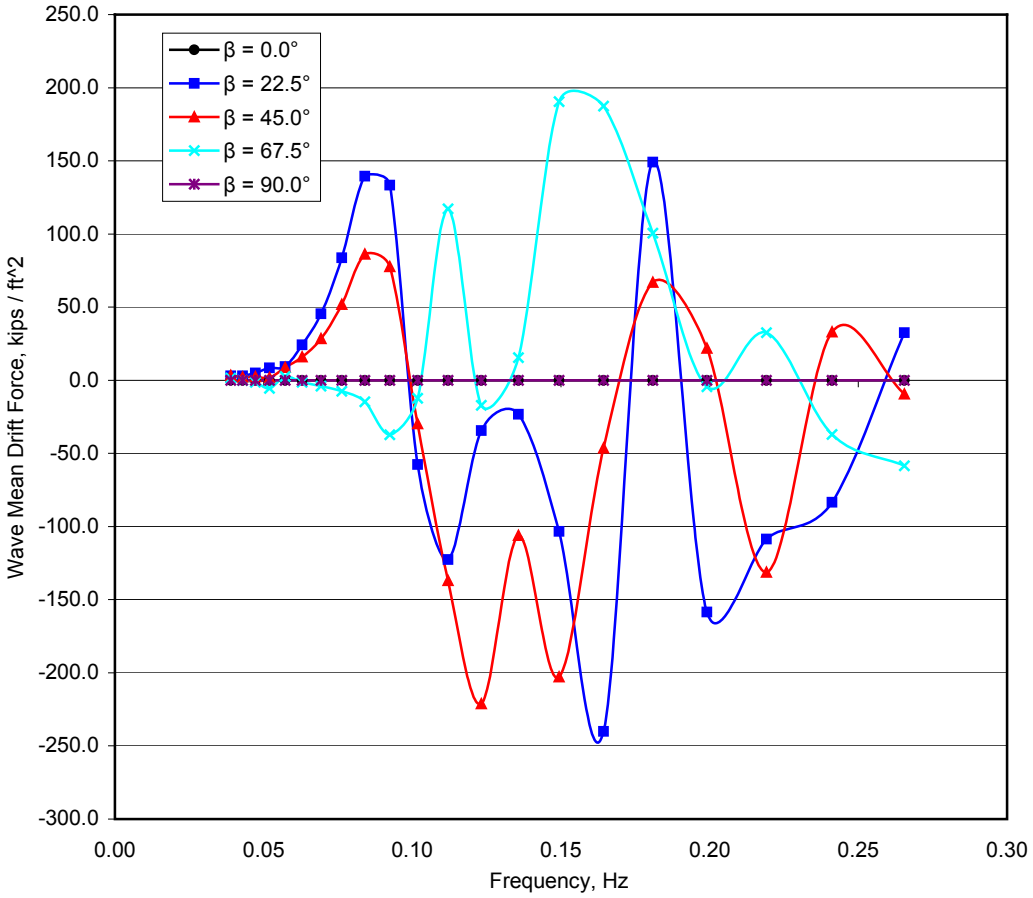

Fig.A-3.7. MODU II yaw wave mean drift force coefficients.

APPENDIX A-4

MODU WIND AND CURRENT FORCE COEFFICIENTS

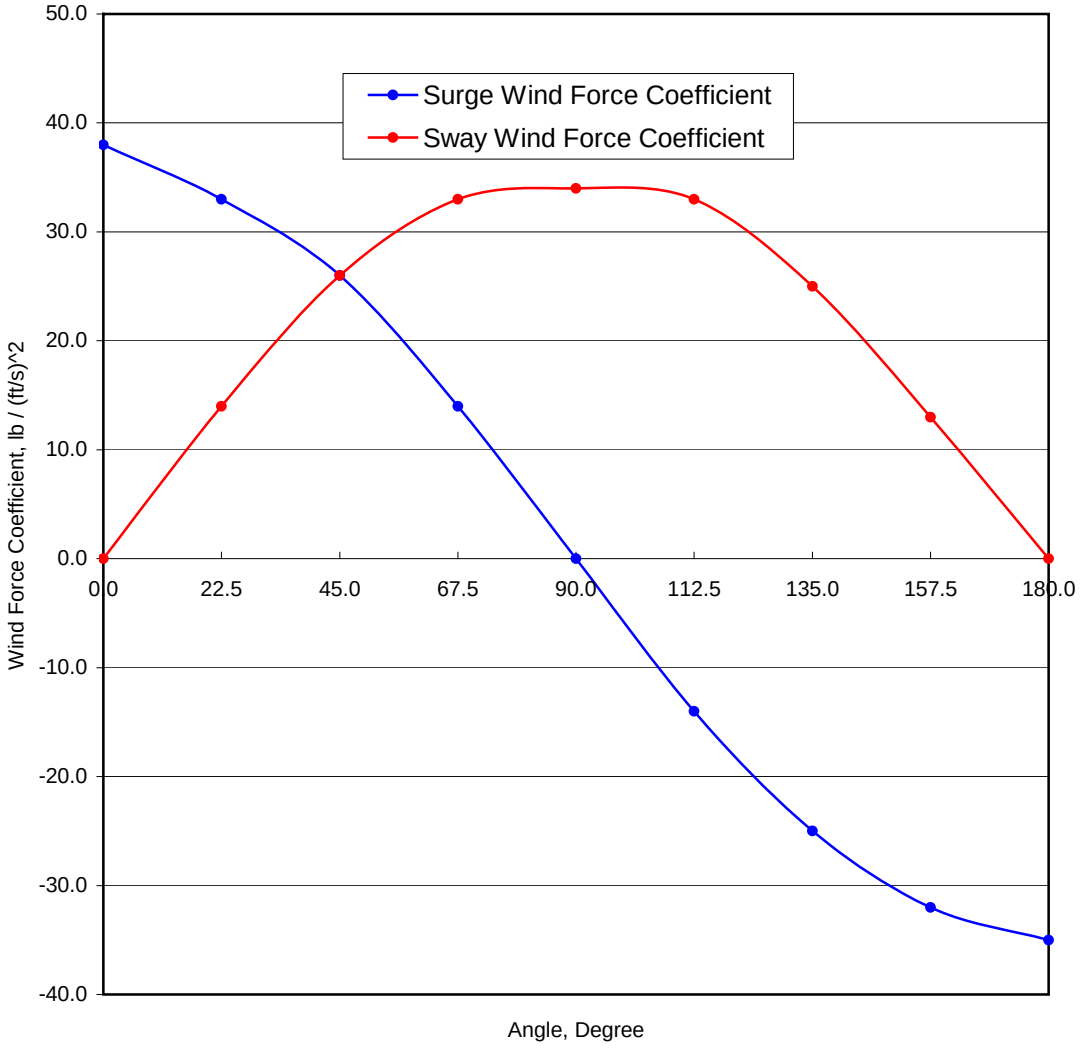

Fig.A-4.1. MODU I wind force coefficients.

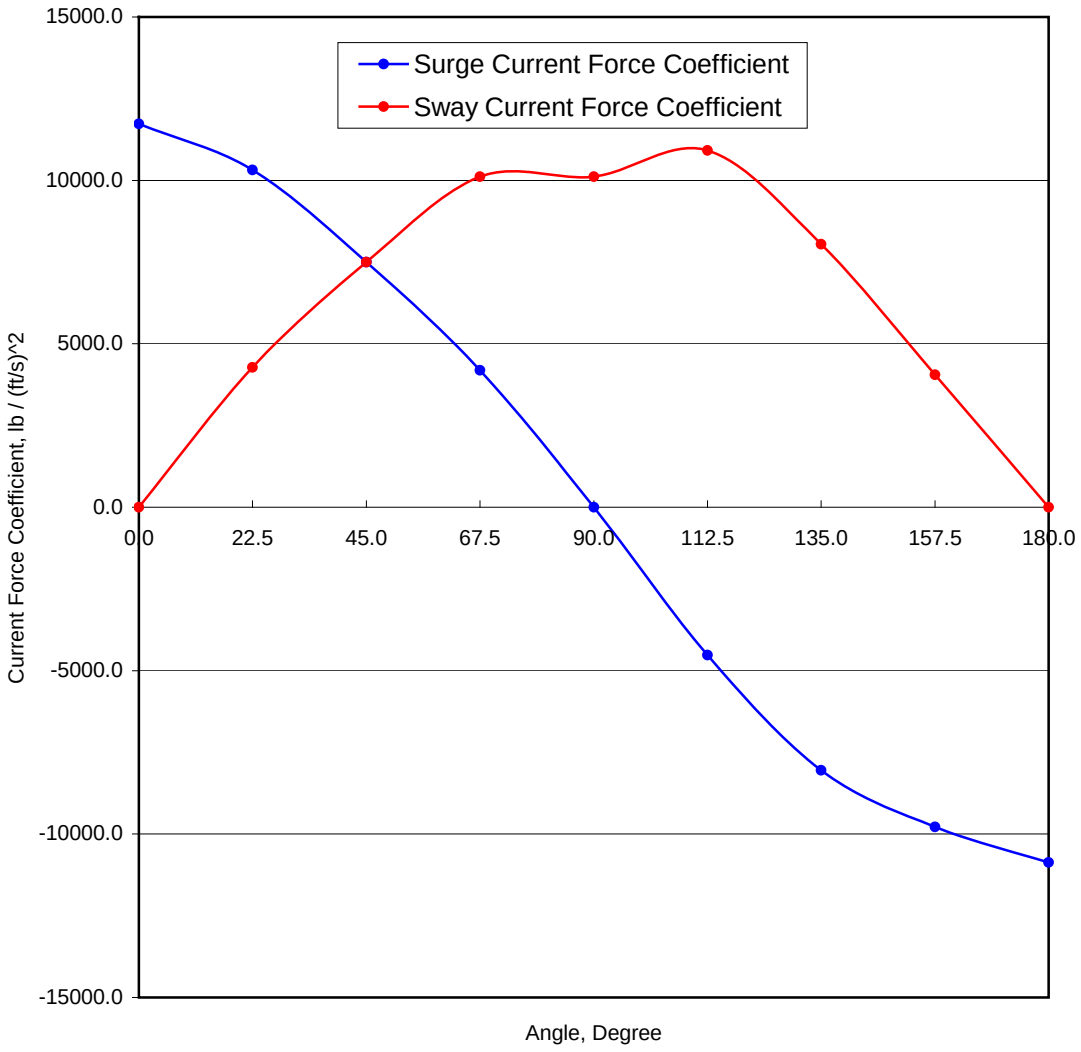

Fig.A-4.2. MODU I current force coefficients.

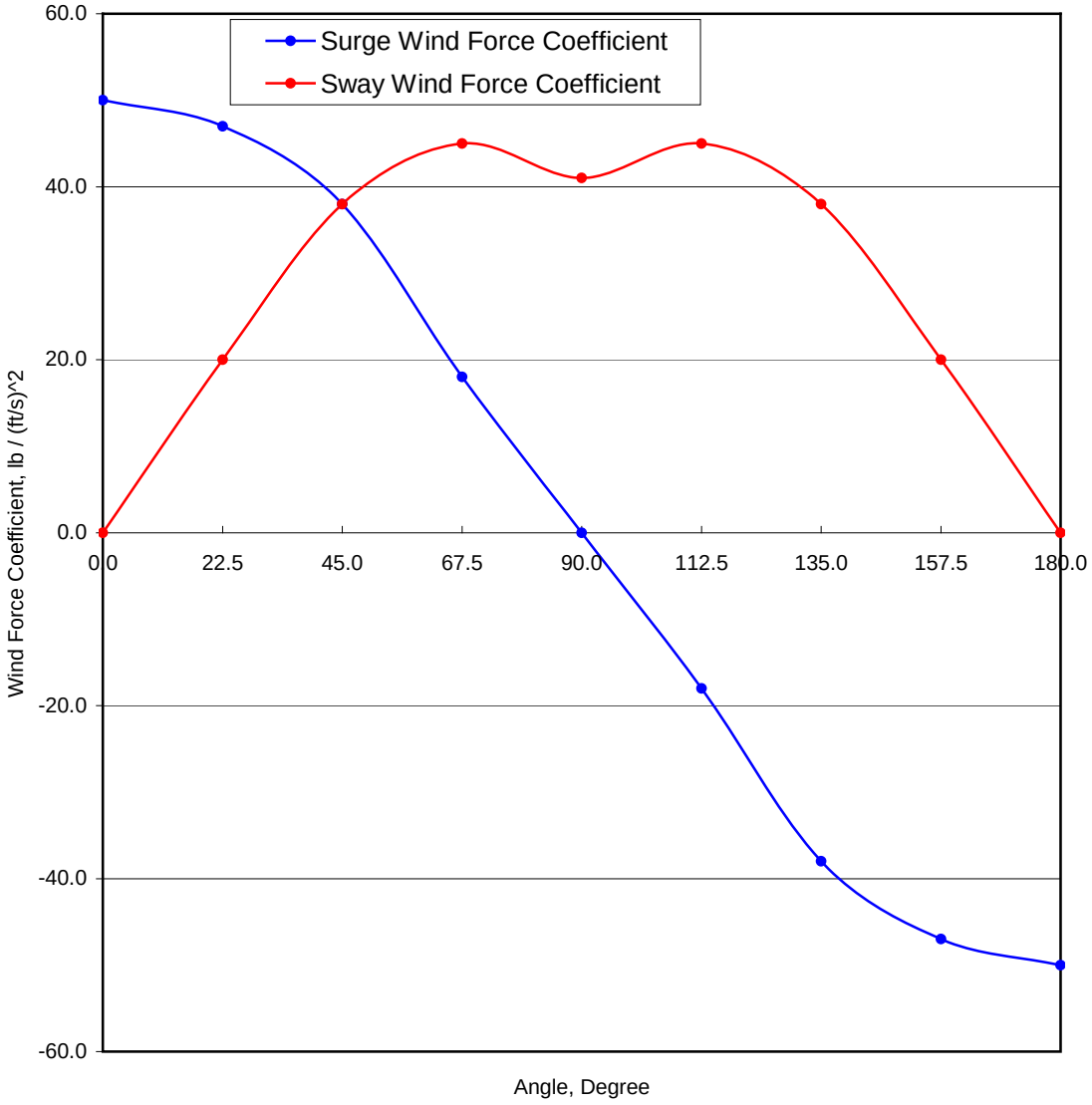

Fig.A-4.3. MODU II wind force coefficients.

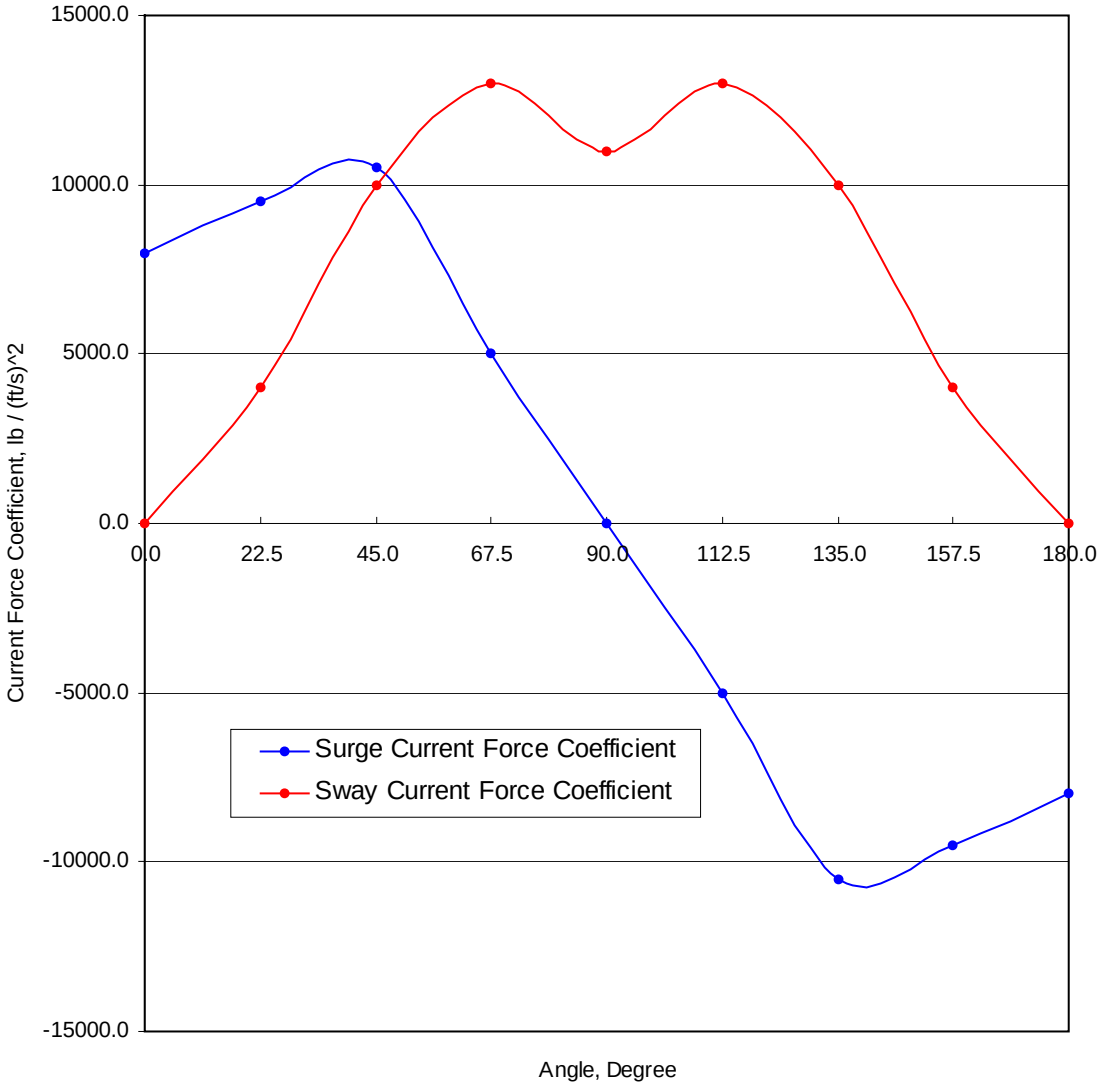

Fig.A-4.4. MODU II current force coefficients.

VITA

Name:	Galin Valentinov Tahchiev
Address:	1333 Eldridge Parkway # 535, Houston, TX 77077
Email Address:	g_tahchiev@yahoo.com
Education:	B.A., Naval Architecture and Marine Engineering, Technical University of Varna, Bulgaria, 2002 M.S., Ocean Engineering, Texas A&M University, 2007